8-2013

DUCTILITY ENHANCEMENT AND STRUCTURAL ORIGIN OF DUCTILE-BRITTLE TRANSITION IN BULK METALLIC GLASSES

Weidong Li
wli20@utk.edu

To the Graduate Council:

I am submitting herewith a dissertation written by Weidong Li entitled "DUCTILITY ENHANCEMENT AND STRUCTURAL ORIGIN OF DUCTILE-BRITTLE TRANSITION IN BULK METALLIC GLASSES." I have examined the final electronic copy of this dissertation for form and content and recommend that it be accepted in partial fulfillment of the requirements for the degree of Doctor of Philosophy, with a major in Materials Science and Engineering.

Yanfei Gao, Major Professor

We have read this dissertation and recommend its acceptance:

Hongbin Bei, Peter K. Liaw, Xiaopeng Zhao

Accepted for the Council:

Carolyn R. Hodges

Vice Provost and Dean of the Graduate School

(Original signatures are on file with official student records.)

DUCTILITY ENHANCEMENT AND STRUCTURAL ORIGIN OF DUCTILE-BRITTLE TRANSITION IN BULK METALLIC GLASSES

A Dissertation Presented for the
Doctor of Philosophy
Degree
The University of Tennessee, Knoxville

Weidong Li

August 2013

Dedication

To My Teachers

To My Family

To My Friends

ACKNOWLEDGEMENTS

This dissertation work is completed with help of many professors, colleagues and friends, among which the greatest gratitude should go to my major advisor, Dr. Yanfei Gao. Back to about three year ago, I was really worried about my future research works with him, since I have never touched solid mechanics and reading those intricate mechanics equations is really a headache for me. Right now as I am finishing my PhD study, I can claim that I am happy to work with Dr. Gao. Dr. Gao sets up a good example for me. He is smart, hard-working and stringent with scientific research scholar but also a considerate, patient and knowledgeable mentor. Three years of working with him is successful and important for my future career.

I also would like the give my great thanks to Dr. Hongbin Bei at the Oak Ridge National Laboratory. As a de facto co-advisor, he started to guide me to perform experimental researches at ORNL in September, 2011. His thoughts always inspire me to think and my view of science is constructed mainly with his guidance. He is an excellent scientist. I would like to thank Dr. Peter K. Liaw for his nice encouragement and supports.

I would also like to thank my committee members, Prof. Yanfei Gao, Prof. Peter K. Liaw, Prof. Hongbin Bei and Prof. Xiaopeng Zhao, for their precious time and efforts.

I would like to express my appreciation to all my team members, Lili Zheng, Jianyong Meng, Tianlei Li, Haoling Jia, Zhinan An, Lin Li, Chi-hua Yu, Shunfang Li, Yuzhi Xia and Chao Pu. Some of them help me start quickly with research and life in US, and discussions with them can always have me learn new things.

Finally, I give my great appreciation to my grandparents, my parents, my sister and many other relatives. When I was in middle school, I did not even know what the college and university are and my parents did not know either. The only thing they know is to support me. Without their supports, I can never be here.

ABSTRACT

Brittleness largely restricts promising applications of the metallic glasses as a new engineering material. Understanding fundamental amorphous structure, deformation mechanisms and search for ways to enhance its ductility is imperative. Among these, establishing a valid structure-property relationship is particularly important. Following these thoughts, a series of research works are conducted.

Both the finite element simulation and in-situ transmission electron microscopy were conducted to investigate the size effect in amorphous ZrCu nanopillars. Studies demonstrate that the deformation is localized near the top of the metallic glass pillars, which looks absent from outside, but form inside.

By assigning the free volume constitutive relation to the metallic glass, the radial shear bands were observed when indenting directly a bulk metallic glass, while extra semi-circular shear bands were found when a bonded-interface is introduced as in experiments.

Ductility enhancement mechanisms in the titanium thin film coated bulk metallic glasses were investigated with both the Rudnicki-Rice instability theory and free volume model. Reflection of the shear band at the film/substrate interface and shear band branching were observed. On top of that, the effect of adhesion between the film and substrate and the film thickness were also investigated.

Shear bands in the BMG composites are found initiate from the second phase/matrix at an angle or ~45 ^{o}, forming a blocking mechanism to the shear bands propagation, contributing to ductility improvement.

Finally, statistical nanoindentation experiments were employed to study the structure-mechanical property relationship of the metallic glass. The statistical nanoindentation technique finds that the pop-in load and the corresponding maximum shear stress increases gradually with increasing degree of structural relaxation, accompanied with a decrease in the statistical variation. A quantitative model incorporating both thermally-activated and defect-assisted processes is developed to understand the pop-in statistics, in which the pre-existing defects, or soft zones, are distributed randomly in the hard amorphous matrix.

Before performing nanoindentation tests, for reliability of the results, the spherical indenter tip radii were calibrated by taking the machine stiffness into the classic Hertzian solution rather than assuming a constant machine stiffness. By this method, the machine stiffness of the nanoindentation system was also explicitly evaluated.

TABLE OF CONTENTS

CHAPTER 1 INTRODUCTION 1
1.1. Deformation Behaviors of the Metallic Glass 4
1.1.1. Atomistic deformation mechanism 4
1.1.2. Homogeneous deformation 5
1.1.3. Inhomogeneous deformation 8
1.1.4. The constitutive law 10
1.2. Ductility Enhancement in the Metallic Glass 14
1.2.1. Enhanced by geometrical constraints 15
1.2.2. Enhanced via bulk metallic glass composites 16
1.3. Fracture Behaviors of the Metallic Glass 18
1.4. Motivation and objectives 20
CHAPTER 2 SHEAR BAND PREDICTION UNDER GEOMETRIC CONSTRAINTS 24
2.1. Introduction 24
2.2. Shear bands in BMG nanopillars 25
2.2.1. Experimental details 27
2.2.2. The free volume model 28
2.2.3. In-situ TEM observation 29
2.2.4. Prediction with the free volume model 34
2.2.5. Summary 37
2.3. Shear band pattern under indentation 38
2.3.1. Motivation 38
2.3.2. Direct spherical indentation 40
2.3.3. Bonded-interface indentation 44
2.3.4. Summary 47

CHAPTER 3 DEFORMATION MECHANISMS IN THE COATED BMG AND BMG COMPOSITES 48
3.1. Introduction 48
3.2. Enhanced ductility in the coated BMG 49
3.2.1. Motivation 49
3.2.2. Study with the Rudnicki-Rice instability theory 51
3.2.3. Study with the free volume model 56
3.2.4. Summary 63
3.3. Deformation mechanisms in the BMG composites 63
3.3.1. Lattice strain evolution in BMG composites 63
3.3.2. Lattice strain prediction with elastic-plastic model 67
3.3.3. Shear band evolution and deformation mechanism 75
3.3.4. Summary 85
CHAPTER 4 EFFECTS OF MACHINE STIFFNESS ON THE LOADING-DISPLACEMENT CURVE DURING SPHERICAL NANO-INDENTATION 86
4.1. Introduction 86
4.2. Method 90
4.3. Experimental 93
4.4. Results 96
4.4.1. Determination of indenter radius R 96
4.4.2. Determination of machine stiffness $S_{machine}$ 100
4.5. Discussion 105
4.6. Summary 109
CHAPTER 5 NANOMECHANICS OF STRUCTURAL ORIGIN OF THE TRANSITION FROM PURE GLASS TO METAL-LIKE BEHAVIOR IN METALLIC GLASES 113
5.1. Introduction 113
5.2. Three point-bending tests 116

5.3. Statistical nanoindentaiton tests 121
5.4. A quantitative structure-property relation 131
5.5. Summary 138
CHAPTER 6 CONCLUSIONS AND PERSPECTIVES 139
REFERENCES 144
VITA 163

LIST OF TABLES

Table 4.1 Indenter tip radii provided by the manufacturer (denoted as nominal), measured by the optical image of the indentation impressions on tin, derived by fitting to Eq. (4-1) and by our subtraction method in Eq. (4-8) using two materials (sapphire and fused silica). The corresponding machine stiffness can be fitted to the form of $S_{machine} = S_0 + kP$ ……...……...……112

Table 5.1 Fitting parameters in the unified structural model that incorporates both the thermal activation process and defect-assisted stochastic behavior……136

LIST OF FIGURES

Figure 1.1 A comparison of mechanical properties of the metallic glass with traditional materials. 2

Figure 1.2 Schematic illustration of (a) the free volume deformation mechanism and (b) shear transformation zone (STZ) deformation mechanism. 5

Figure 1.3 Steady-state homogeneous flow of the $Zr_{41.2}Ti1_{3.8}Cu_{12.5}Ni_{10}Be_{22.5}$ metallic glass at elevated temperatures, along with fittings with Eq. (1-1). 6

Figure 1.4 Non-steady-state homogeneous flow of the metallic glass, in which a typical stress overshoot can be observed before a steady-state condition is achieved 7

Figure 1.5 Development of the strain rate in the forming shear band, $\dot{\gamma_b}$, and surrounding matrix, $\dot{\gamma_m}$, normalized by the applied shear strain rate $\dot{\gamma_s}$. 8

Figure 1.6 A scanning electron micrograph showing formation of tin beads by melting of the pre-covered fusible tin coating during deformation, providing evidence of heat generation within the operating shear bands. 9

Figure 1.7 Brittle failure of the metallic glass under uniaxial (a,b) compression and (c,d) tension. Only limited plasticity can be achieved due to sudden fracture along a major shear band. 10

Figure 1.8 Atomic jumps in metallic glasses responsible for macroscopic plastic flow . 12

Figure 1.9 Creation of the free volume by squeezing an atom of volume v* into a neighboring hole of smaller volume v 13

Figure 1.10 Enhancing ductility of the metallic glass by Cu coating and (b) schematic illustration of the enhancing mechanism 15

Figure 1.11 Enhanced ductility of the bulk metallic glass by artificially creating a stress gradient 16

Figure 1.12 (a) Scanning electron microscopy of the Zr-based bulk metallic glass composite with dendrite crystalline phases. (b) Corresponding strees-strain curve showing substantially improved plasticity. The inset shows the deformed metallic glass composite. 17

Figure 1.13 (a) Scanning electron microscopy of fracture surface of the ductile metallic glass, showing the characteristic vein patter. (b) Fracture surface of the brittle metallic glass, in which the vein pattern can only be observed at a large magnification. 18

Figure 1.14 (a) Variation of the fracture energy with Poisson's ratio and (b) bulk-to-shear modulus ratio. Both shows sharp brittle-to-ductile fracture transition at certain a critical value 19

Figure 2.1 Representative stress–strain curves for nanocompression tests on the ZrCu thin film metallic glass pillars. 30

Figure 2.2 Video snaps taken from the in situ TEM compression showing the deformation of a Zr-based pillar (Pillar 1). The different stages of the nanocompression process are depicted by individual frames (a–h) at different strains: (a) undeformed, (b) ~2%, (c) ~4%, (d) ~6%, (e) ~8%, (f) ~10%, (g) ~15%, (h) ~20%. The corresponding stress–strain curve is inset at the bottom left corner for point-to-point correspondence. . 32

Figure 2.3 (a) Change in cross-sectional area vs. distance for Figure 2(b), (d), (f) and (h). Distance stands for distance at the top of the pillar sample. (b) Area change ratio as a function of the distance from the specimen top (normalized by the base diameter) at three representative deformation stages, with free volume contours in the insets. Contour plots are given in the deformed mesh, with displacement magnification ratios being 1 in all three directions. 34

Figure 2.4 (a) Compression of a Mises plastic pillar with a stiffness to yield stress ratio of 240; (b) compression of the same pillar but with the free volume constitutive law (where SDV1 indicates the free volume). Barreling deformation can be seen in the Mises solid. By contrast, highly localized deformation of metallic glass occurs with the shear band evolution procedure demonstrated by the free volume contour, which is given in the deformed mesh, with displacement magnification ratios being 1 in all three directions.. 36

Figure 2.5 (a) $Zr_{52.5}Al_{10}Ti_5Cu_{17.9}Ni_{14.6}$ bulk metallic glass sample indented with the bonded interface technique. Two parts are bonded together by using the super glue. (b) Shear bands observed on the bonded interface after splitting two parts and removing the su super glue. Shear bands consist of radial shear bands and semi-circular shear bands . 39

Figure 2.6 (a) Shear band patterns on the half-symmetric interface of the metallic glass substrate (without interface constraints) under spherical indentation. (b) Radial shear bands and (c) semi-circular shear bands on the half-symmetric interface of the bonded interface metallic glass substrate under spherical indentation..... 40

Figure 2.7 Finite element model used for predicting shear band under spherical indentation..... 41

Figure 2.8 To clearly visualize the three-dimensional conical shear band, free volume contours (SDV1) were plotted on a vertical plane that makes an angle of 60º from the backside surface in (a), and on a horizontal plane at a distance of 0.07R below the top sur surface in (b). Finite element simulations were performed in a quarter of the substrate under spherical indentation with symmetry boundary conditions prescribed on the two side surfaces. These plots are given in deformed mesh with displacement magnification ratios being 10, 2, and 10 in X, Y, and Z directions, respectively..... 43

Figure 2.9 When the traction free boundary condition is prescribed on one side surface, the first shear band becomes spade like with the initiation site marked by “X” in (a). A horizontal cut at a distance of 0.03R below the top surface is given in (b). These two plots

are given in deformed mesh with displacement magnification ratios being 10, 2, and 2 in X, Y, and Z directions, respectively. (c) A slight increase of the indentation load leads to the second shear band which is initiated on the free surface, as shown by the free volume contours in undeformed mesh. 45

Figure 3.1 Bending stress vs. bending strain for the uncoated bulk metallic glass and coated bulk metallic glasses with different materials 50

Figure 3.2 Top view of the indented (a) bulk $Zr_{52.5}Cu_{17.9}Ni_{14.6}Al_{10}Ti_5$ (Vitreloy 105) metallic glasses and (b) the same sample coated with 200 nm think pure Ti. More shear bands are observed in the coated sample. 51

Figure 3.3 (a) Half-symmetric Rockwell indention model on the metallic glass used for predicting shear band directions in (b) the bulk metallic glass and (c) titanium film coated bulk metallic glass, with $\mu+\beta=0$ and $\upsilon=0.3$. The blue solid curves indicate predicted s shear band directions and the red dashed curves are principal shear stress directions. The short solid black and dashed green curves are corresponding shear band directions and the principal shear stress directions. For clarity, the material coordinate space beneath the indenter is normalized by the contact half width *a*. 54

Figure 3.4 Free volume contour plots on different indentation configurations. (a) Indentation on the bulk metallic glass, without any coating. (b) Indentation on a thin film coated BMG with a bulk/ film thickness ratio of 20. The substrate and film is completely bonded, corresponding to the perfect adhesion case in practice. (d) Indentation on a same film coated BMG, but with zero adhesion. Practically, the film is simply put above the substrate and their interaction is frictionless. All plots are given in deformed mesh with displacement magnification ratio of 1 in three directions. 59

Figure 3.5 An indentation model with free-volume contour plots in different film-thickness cases: (a) a BMG substrate with a thin TFMG, having a film/substrate thickness

ratio of 1/20 and (b) a BMG substrate with a thick TFMG, having a film/substrate thickness ratio of 1/5 62

Figure 3.6 (a) Bulk metallic glass composite $Zr_{58.5}Ti_{14.3}Nb_{5.2}Cu_{6.1}Ni_{4.9}Be_{11.0}$, with soft dendritic crystals randomly distributed in the matrix. (b) The compressive stress versus strain, showing apparent plasticity. 65

Figure 3.7 Stress versus lattice strain in the crystalline phase of the bulk metallic glass composite studied by both the Synchrotron diffraction measurement and crystal plasticity modeling, showing characteristic 'tunrover' behavior at large stress level 67

Figure 3.8 Compressive stress as a function of the lattice strain for the composite with 90^o oriented dendrite inclusion, and corresponding Mises stress evolution contours at representative stages (I)~(IV) are shown in (b). Both the matrix and inclusion are simulated as elastic-perfectly-plastic bodies, with Young's modulus, Poisson's ratio and yield stress being 89 GPa, 0.37, 1.4 GPa and 60 GPa, 0.37, 0.45 GPa, respectively. 69

Figure 3.9 (a) Compressive stress as a function of the lattice strain for the composite with 45^o oriented dendrite inclusion, and corresponding Mises stress evolution contours at representative stages (I)~(IV) are shown in (b). Properties of the matrix and inclusion are the same as the previous. 72

Figure 3.10 (a) Applied stress as a function of the $\varepsilon_{ss}^{elastic}$ for both inclusion and matrix in the composite with multiple circular inclusions, and (b) the corresponding Mises stress evolution contours at representative stress levels (i) - (iv). The matrix is described by the free volume constitutive model through a UMAT subroutine in ABAQUS, with Young's modulus and Poisson's ratio being 200 GPa and 0.37, respectively. Other parameters can be found in text. The inclusion phase is elastic-perfectly plastic solid with Young's modulus, Poisson's ratio, and yield stress being 60 GPa, 0.37, and 0.45 GPa, respectively.

All figures are given in deformed mesh with a displacement magnification ratio of 1 and the state dependent variable 1 (SDV1) specifies the free volume. 79

Figure 3.11 (a) Applied stress as a function of the $\varepsilon_{22}^{elastic}$ for both inclusion and matrix in the composite with multiple dendrite inclusions, and (b) the corresponding Mises stress evolution contours at representative stress levels (i) - (iv). All the parameters are the same as those in Fig. 3.10. 82

Figure 4.1 (a) Schematic illustration of the instrumented indentation system (reproduced after Oliver and Pharr, 1992) and (b) schematic diagram showing that the experimentally measured displacement is the sum of the loading frame deflection, $h_{machine}$, and the penetration into the sample, h_{sample}, i.e., $h_{total}=h_{sample}+h_{machine}$.....89

Figure 4.2 Line scan and three dimensional view of the indentation impression on tin characterized by a white light interferometer, from which the indenter tip radius can be determined. Dash curve represents spherical tip with radius of 253μm. 95

Figure 4.3 Determination of the indenter tip radius. (a) Experimental P-hreported data on sapphire and fused silica using the Tip #2 indenter, shown by symbols. Direct Hertzian fitting is shown by the black solid curves and the Hertzian solutions with indenter radii obtained from our subtraction method are given by the red dashed curve. (b) The subtraction method is used to fit h_{fs}-h_{sp} (fs: fused silica; sp: sapphire) to $P^{2/3}$ as in Eq. (4-8). The slope can be used to determine the indenter tip radius. 98

Figure 4.4 Load-displace curves using the small tip-radius indenter (Tip #7). Symbols represent experiment P-hreported curves. Direct Hertzian fitting by using Eq. (4-1) is shown by the black solid curves and the Hertzian solutions with indenter radii obtained fro from our subtraction method are given by the red dashed curve. Notes that the black solid curves overlap the red dashed curve. 102

Figure 4.5 Maximum indentation loads and deviation loads for various indenters. The deviation load denotes load where the Hertzian solutions deviate noticeably from experimental P-$h_{reported}$ curves, as shown in Fig. 4.3(a). For small indenters, negligibly tiny deviation occurs, and the maximum loads equal to the deviation loads. The deviation load is around 0.05 N for the large indenters. 103

Figure 4.6 Machine stiffness under different loads with selected indenter tips. The machine stiffness approximately shows linear dependence on the load and can be described with $S_{machine} = S_0 + kP$, in which fitting parameters k and S_0 can be found in Table 1. For small indenters, the calculated machines stiffness is close to the pre-defined machines stiffness, $S_{default}$=9.1 N/μm. Machine stiffness at loads below 10% of the maximum load were not calculated because of great system errors. 105

Figure 4.7 Plots of contact stiffness versus load for the two materials using large indenter Tip #2 in (a) and small indenter Tip #7 in (b)..... 108

Figure 5.1 (a) Load-deflection curves for the as-cast Zr-based metallic glass and variously annealed samples under three point bending test, illustrating the ductile-to-brittle fracture transition. Insets show the fracture surfaces. (b) The synchrotron X-ray diffraction pattern of the annealed sample (at 300ºC). Diffuse rings reveal characteristic amorphous structure. (c) Pair distribution function (PDF) of the as-cast and annealed samples (at 200 ºC and 300ºC) . 118

Figure 5.2 (a) A representative nanoindentation P-h curve showing the pop-in as the onset of the plastic deformation. (b) Dependence of the first pop-in loads on the annealing temperature and the indenter tip radius (R=0.40, 1.78 and 3.80 μm). (c) Dependence of the maximum shear stress at the first pop-in on the annealing temperature and the indenter tip radius. 124

Figure 5.3 Cumulative pop-in probability as the function of the maximum shear stress τmax under various annealing temperatures and indenters: (a) R=0.40 μm, (b) R=1.78 μm and (c) R=3.80 μm. Solid curves are prediction from our unified structural model..... 128

Figure 5.4 Schematic illustration of the structural origin of the transition from metal-like to pure glass behavior in metallic glasses: (a) the as-cast condition, (b) intermediately relaxed state, and (c) extremely relaxed state (i.e., pure glass). Soft zones, as pre-existing defects, will facilitate ductile deformation, while the pure-glass state experiences the intrinsic, thermally-activated deformation..... 137

CHAPTER 1

Introduction

Amorphous solids exist in various material systems, like silicate glasses and amorphous polymers in the non-metallic material system. The metallic glass (also called amorphous alloys or glassy alloys) is an amorphous counterpart in the metallic material system, a relatively newcomer to the amorphous material family. The first metallic glass was fabricated at Caltech on $Au_{75}Si_{25}$ alloy by Klement et al. using the rapid-quenching experiments in 1960 [1]. Upon invention, it has attracted numerous scientific attentions and interests due to its unique mechanical properties, including high strength, large elastic limit, high fracture toughness and good corrosion resistance, and potential engineering applications [2, 3]. A comparison of the mechanical properties of the metallic glass with traditional materials is shown in Fig. 1.1. Such superior mechanical properties attributes to its amorphous structure characterized by lack of long-range order in atomic structure, opposed to periodic atomic arrangement in crystalline materials.

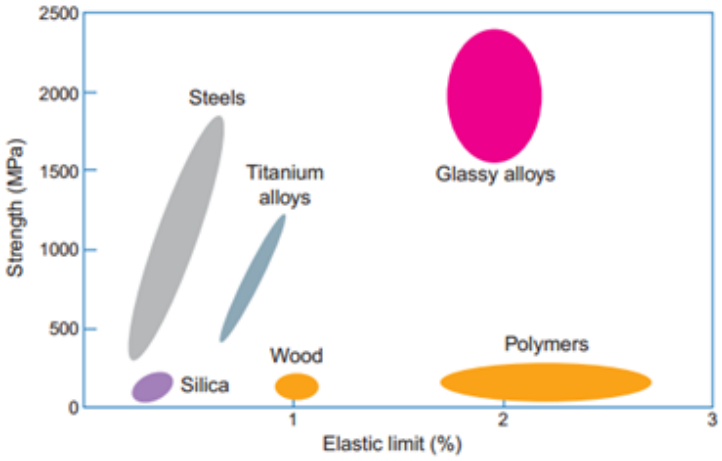

Figure 1.1 A comparison of mechanical properties of the metallic glass with traditional materials [3].

Afterwards, many different techniques were developed to fabricate a wide variety of metallic glasses. However, early fabrication of metallic glasses only limited to the thin film, ribbon or sheet because of the high cooling rate requirement during solidification. Accordingly, lowering down the required cooling rate and producing large sized metallic glass samples became the focus of the research. Such a need partly facilitated development and maturity of theories on formation of the glassy structure. One of the indices that successfully predict the glass forming ability (GFA) of an arbitrary combination of elemental constituents is the reduced glass transition temperature $T_{rg}=T_g/T_m$ (ratio of the glass transition temperature to the melting point) [4]. It is believed that a liquid having $T_{rg}=2/3$ can easily bypasses crystallization and cool to the amorphous state [5]. Advances in the experimental techniques and theoretical frameworks on formation of the amorphous structure ultimately provoked emergence of the bulk metallic glass in

Pd-Cu-Si alloy in 1970s, whose dimensions is in millimeter scale [6]. Around twenty years later, larger sized bulk metallic glasses (in excess of 1 cm) were proven to be able to be fabricated at a cooling rate of ~100 K/s in mulitcomponent Zr-based, La-based and Mg-based alloy systems [7, 8]. So far, the critical cooling rate for formation of metallic glasses can be as low as 10^{-1} K/s and the maximum sample thickness can be over 10 cm [9]. It need to be emphasized that emergence of the quinary Zr-based bulk metallic glasses, like Vitalloy 1 ($Zr_{41}Ti1_4Cu1_{2.5}Ni_{10}Be_{22.5}$), is another milestone of development of the bulk metallic glasses [10]. This family of metallic glasses exhibits high thermal stability and can form into ~10 cm diameter amorphous rods at a cooling rate of 1K/s. Owing to its attractive GFA, Zr-based metallic glasses had draw extensive attentions and were applied in industries only 3 years after its invention [11]. Currently, numerous metallic glass systems have being developed and studied and more attentions turn to Fe-, Cu-based metallic glasses and bulk amorphous steels [6-8, 12-19].

Generally, development of metallic glasses systems started with expensive metals, like Au, Pd and Pt, followed by less expensive Zr, Ti, Ni and further followed by much cheaper Fe and Cu and finally turn to the amorphous steel [11]. Such a development trace reflects human's desire to push new materials into engineering applications, which is the destination of any new materials.

1.1. Deformation Behaviors of the Metallic Glass

1.1.1. Atomistic deformation mechanism

As one knows, in crystalline materials, dislocation activities govern the deformation [20]. Unlikely, in the metallic glass, owing to absence of the crystalline defects, the dislocation mechanism no longer exist and a scenario of local atomic rearrangement is believed to be responsible for the deformation [21-27]. Two most extensively used atomistic deformation mechanism models in the metallic glass are the free volume model [28, 29] and shear transformation zone model (STZ) [30, 31]. The free volume model was first applied to the case of the metallic glass by Spaepen [28] via borrowing similar concept from conventional glasses and liquid [32, 33]. In this model, a conceptual state variable, the free volume, is introduced to control strain evolution in the metallic glass. The free volume is defined as the average excess atomic volume in a real material compared to an ideally ordered structure. Deformation of the metallic glass is caused by a series of discrete atomic jumps. In the pure shear case, the macroscopic plastic flow occurs as a result of net forward atomic jumps in the direction of applied stress, as depicted by Fig. 1.2 (a).

The STZ model is somehow similar with the free volume model in the sense of atomistic description of the deformation except that it interprets a cluster of atom containing ~100 atoms as the deformation unit [34-39]. Operation of a STZ under shear stress is shown in Fig. 1.2(b). Both of these two mechanisms are thermally activated with

comparable activation energy scale of around tens of kT_g, with k the Boltzmann constant and T_g the glass transition temperature [28, 33].

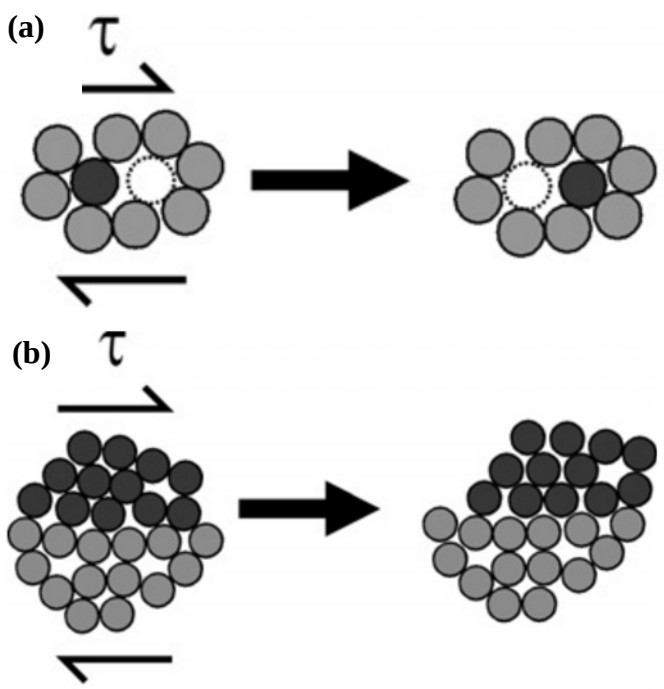

Figure 1.2 Schematic illustration of (a) the free volume deformation mechanism and (b) shear transformation zone (STZ) deformation mechanism [21].

1.1.2. Homogeneous deformation

The homogeneous deformation in the metallic glasses normally happens at elevated temperatures and the materials can experience large strain under loading without failure. Particularly, if an equilibrium between the structural disordering and ordering can be instantly achieved, a steady-state homogeneous flow is obtained. From atomistic point of

view, the free volume creation equals annihilation and no biased accumulation occurs [21, 28]. In the framework of STZ model, the plastic flow under uniaxial compression or tension can be described by [39, 40]

$$\dot{\varepsilon} = \alpha_0' \upsilon_0 \gamma_0 \exp(-\frac{Q}{kT}) \sinh(\frac{\sigma V}{\sqrt{3}kT}) \quad (1\text{-}1)$$

where υ_o is frequency of the vibration; α_0' is a constant that could incorporate state variables like the free volume; $\dot{\varepsilon}$ and σ are uniaxial strain rate and stress; γ_0 is the characteristic strain of each net forward operation; V=$\Omega_0\gamma_0$, with Ω_o the characteristic STZ volume. Fig. 1.3 is the representative steady-state plastic flow for $Zr_{41.2}Ti1_{3.8}Cu_{12.5}Ni_{10}Be_{22.5}$ metallic glass studied by experiments along with theoretical fits with Eq. (1-1) [41].

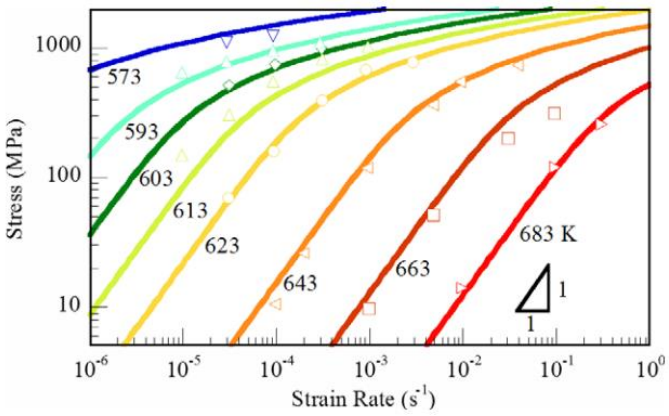

Figure 1.3 Steady-state homogeneous flow of the $Zr_{41.2}Ti_{13.8}Cu_{12.5}Ni_{10}Be_{22.5}$ metallic glass at elevated temperatures, along with fittings with Eq. (1-1) [41].

As one can sees from Eq. (1-1) and Fig. 1.3, the plastic flow is in nature strain rate sensitive. At the low stress level, the stress is linearly proportional to the strain rate and the flow is Newtonian. In this condition, the metallic glasses can be deformed up to 1000% [42]. With increase of the strain rate, non-Newtonian flow will become dominant and deformability of the metallic glass will be largely reduced [43, 44].

Another form of homogeneous flow of the metallic glass is the non-steady-state flow. The reason why it is called non-steady-state is that the free volume creation and annihilation is not balanced but the deformation is still homogeneous. Reflecting on the stress-strain relationship, a stress overshoot can be observed when the plastic deformation initially starts. This is followed by a strain softening until the equilibrium of free volume creation and annihilation is reached, as shown in Fig. 1.4 [41].

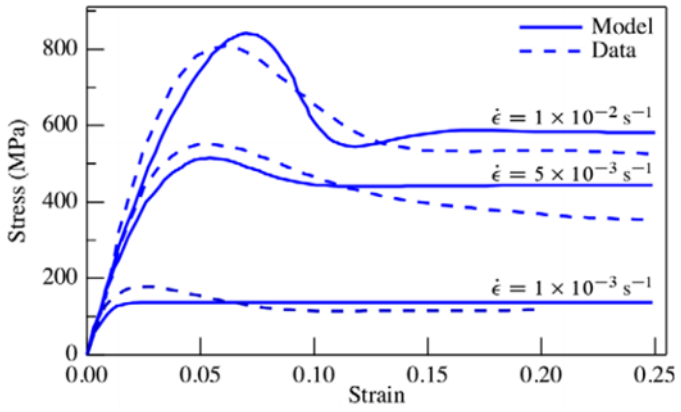

Figure 1.4 Non-steady-state homogeneous flow of the metallic glass, in which a typical stress overshoot can be observed before a steady-state condition is achieved [41].

1.1.3. Inhomogeneous deformation

The inhomogeneous deformation in the metallic glass occurs at high stresses and low temperatures through the shear band operations [45, 46]. Mechanistically, shear band is a result of strain localization caused by softening via localized accumulation of the free volume [47-49], which will lead to a local reduction of the viscosity [50, 51]. This can be understood by a separation of the strain rate in the localized shear band and surrounding matrix, which was theoretically interpreted by Argon and depicted in Fig. 1.5 [31].

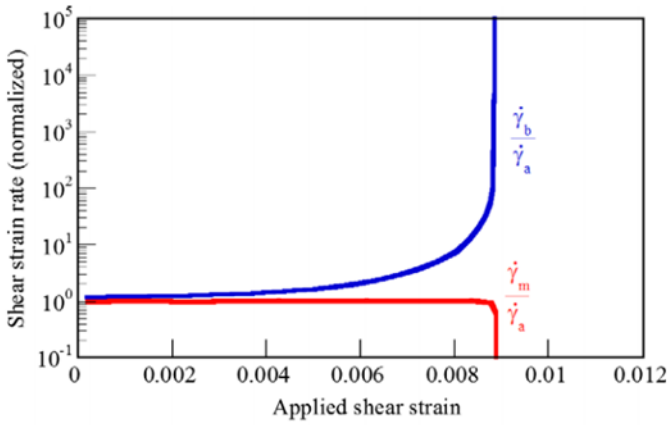

Figure 1.5 Development of the strain rate in the forming shear band, $\dot{\gamma}_b$, and surrounding matrix, $\dot{\gamma}_m$, normalized by the applied shear strain rate $\dot{\gamma}_s$ [31].

An alternative interpretation is the local adiabatic heating within the shear band, which is believed to be the cause of local viscosity decrease [52-54]. This is solidly supported by Lewandowski and Greer's experimental observations, in which a fusible coating of tin was covered on a $Zr_{41.2}Ti_{13.8}Cu_{12.5}Ni_{10}Be_{22.5}$ metallic glass and the coating

was melted promptly during deformation, forming beads on the slip steps (shear bands), as in Fig. 1.6 [55, 56]. This is indicative of heat generation within the shear bands and makes them argue that the temperature rise in the metallic glasses is a result, rather than a cause, of shear banding events.

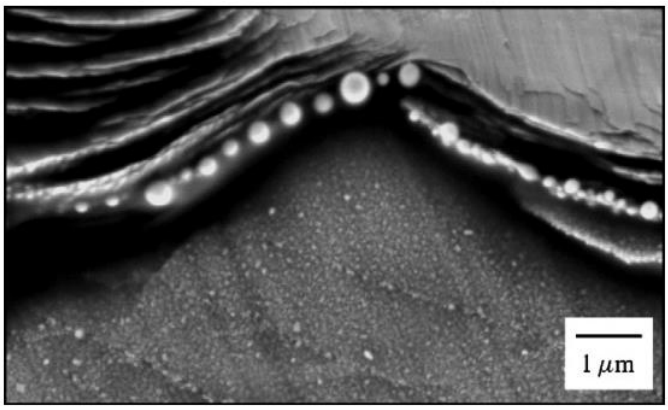

Figure 1.6 A scanning electron micrograph showing formation of tin beads by melting of the pre-covered fusible tin coating during deformation, providing evidence of heat generation within the operating shear bands [55].

Macroscopically, the shear banding is responsible for catastrophic failure of the bulk metallic glass at the room temperature, particularly under uniaxial loading conditions. This makes many bulk metallic glasses exhibit low plasticity under either compression or tension, as representatively shown by the Zr-based metallic glass in Fig. 1.7 [57]. Consequently, understanding the shear band initiation and propagation has been a central subject to study the inhomogeneous deformation mechanism of the metallic glass and avoid brittle failure.

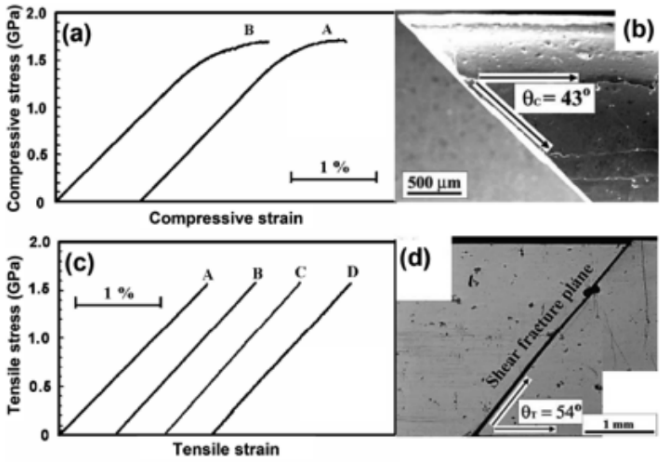

Figure 1.7 Brittle failure of the metallic glass under uniaxial (a,b) compression and (c,d) tension. Only limited plasticity can be achieved due to sudden fracture along a major shear band [57].

1.1.4. The constitutive law

The shear band formation and evolution form fundamental deformation mechanism of the metallic glass. From microscopic level, the shear band formation is believed to be associated with evolution of the local structural order. One atomistic mechanism capturing shear band formation and evolution in bulk metallic glasses is the free volume model proposed by Spaepen [28] and further developed by Steif *et. al* [29]. From continuum mechanics point of view, the shear band is a result of strain softening and can be considered as a strain localization phenomena. The free volume model treats the free volume as the state variable and controls the structural change at the atomic level in bulk metallic glasses.

The free volume is a measure of the departure from the ideally ordered structure and can be regarded as difference between the average atomic volume in real materials and that in the ideally ordered structure. In this model, it assumes that in pure shear case, the macroscopic plastic flow occurs as a result of net forward atomic jumps in the direction of the applied stress. The general flow equation can be represented by

$$\frac{\partial \gamma^p}{\partial t} = 2f \exp\left(-\frac{\alpha v^*}{v_f}\right)\exp\left(-\frac{\Delta G^m}{k_B T}\right)\sinh\left(\frac{\tau\Omega}{2k_B T}\right) \qquad (1\text{-}2)$$

where f is frequency of atomic vibration; α is a geometric factor of order 1; v^* is the hard-sphere volume of an atom; v_f is the average free volume per atom; ΔG^m is the activation energy; Ω is the atomic volume; τ is the applied shear stress; k_B is the Boltzmann constant, and T is the absolute temperature. The average free volume v_f is treated as the order parameter and control the structural change in metallic glasses. Fig. 1.8 schematically demonstrates an individual atomic jump with assistance of the free volume, responsible for the macroscopic plastic flow [28].

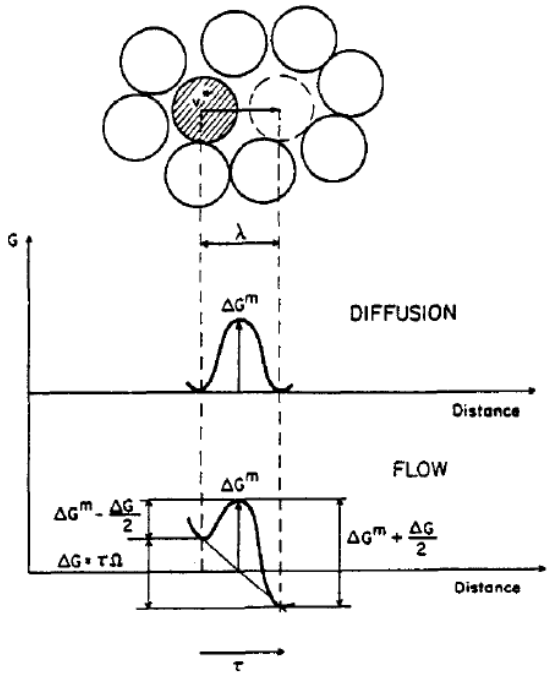

Figure 1.8 Atomic jumps in metallic glasses responsible for macroscopic plastic flow [28].

The structural rearrangement with applied stress is controlled by competition between a stress-induced disordering process and a diffusional reordering process. Consequently, the net increase of the free volume is given as

$$\frac{\partial v_f}{\partial t} = v^* f \exp\left(-\frac{\alpha v^*}{v_f}\right)\exp\left(-\frac{\Delta G^m}{k_B T}\right)\left\{\frac{2\alpha k_B T}{v_f C_{eff}}\left(\cosh\left(\frac{\tau\Omega}{2k_B T}\right)-1\right)-\frac{1}{n_D}\right\} \qquad (1\text{-}3)$$

where n_D is the number of atomic jumps needed to annihilate a free volume equal to υ^* and is usually taken to be 3-10, and the effective elastic modulus is $C_{eff}=E/3(1-\upsilon)$. This is still a stress-controlled process. In other words, at low stress level, the free volume created by the stress can be readily annihilated and the homogeneous deformation is maintained, while at high stress level, a net increase of the free volume arise and hence

shear banding occurs. Fig. 1.9 shows how the free volume is created in an amorphous structure [28].

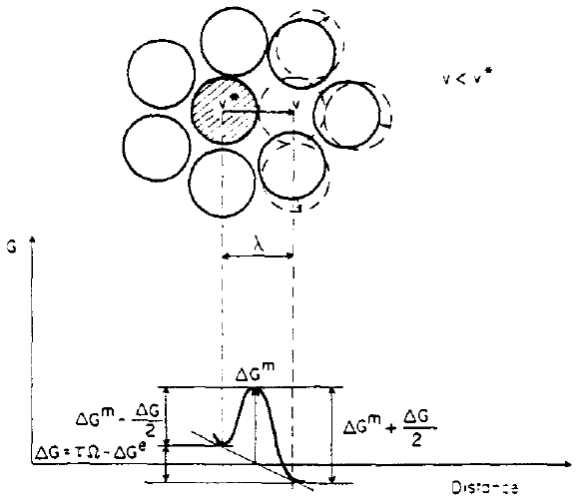

Figure 1.9 Creation of the free volume by squeezing an atom of volume v* into a neighboring hole of smaller volume v [28].

Eq. (1-2) along with Eq. (1-3) form the basics of the constitutive relation applicable for both the homogeneous and inhomogeneous flow in the metallic glasses. With a J_2-type, small strain viscoplasticity framework, the free volume model can be generalized into multiaxial stress states [58]. The strain rates can be decomposed into the elastic and plastic parts:

$$\dot{\varepsilon}_{ij} = \dot{\varepsilon}^{e}_{ij} + \dot{\varepsilon}^{p}_{ij} \tag{1-4}$$

The elastic part can be described by the general Hooke's law,

$$\dot{\varepsilon}_{ij}^{e} = \frac{1+\nu}{E}(\dot{\sigma}_{ij} - \frac{\nu}{1+\nu}\dot{\sigma}_{kk}\delta_{ij}) \tag{1-5}$$

With a characteristic time scale $t^{*} = f^{-1}\exp(\Delta G^{m}/k_{B}T)$, the plastic part, namely, the flow equation (Eq. (1-1)) can be described as,

$$\dot{\varepsilon}_{ij}^{p} = \exp(-\frac{1}{\nu_{f}})\sinh\left(\frac{\sigma_{e}}{\sigma_{0}}\right)\frac{S_{ij}}{\sigma_{e}} \tag{1-6}$$

where $S_{ij} = \sigma_{ij} - \sigma_{kk}\delta_{ij}/3$ is the deviatoric stress tensor and $\sigma_{e} = \sqrt{S_{ij}S_{ij}}$ is the Mises stress.

The free volume evolution equation (Eq.(1-2)) under multiaxial stress states is

$$\dot{\nu}_{f} = \frac{1}{\alpha}\exp(-\frac{1}{\nu_{f}})\left\{\frac{3(1-\nu)}{E}\left(\frac{\sigma_{0}}{\beta\nu_{f}}\right)\left[\cosh\left(\frac{\sigma_{e}}{\sigma_{0}}\right)-1\right]-\frac{1}{n_{D}}\right\} \tag{1-7}$$

where $\sigma_{0} = 2k_{B}T/\Omega$ is the reference stress; $\nu_{f} = \bar{\nu}_{f}/\alpha\nu^{*}$ is the normalized free volume and $\beta = \nu^{*}/\Omega$. Eq. (1-4)~(1-7) define the constitutive relationship for the metallic glass. Note in the above questions, a dot over a quantity denotes $\dot{(\ )} = f^{-1}\exp(\Delta G^{m}/k_{B}T)(\partial(\ )/\partial t)$. Detailed description can be found in Ref. 58.

1.2. Ductility Enhancement in the Metallic Glass

To promote real structural applications of the bulk metallic glasses, preventing the catastrophic shear band propagation and enhancing ductility is of primary importance. Given the reason for brittle failure of the metallic glass is that the shear displacement along a dominant shear band can easily reach a critical value of fracture, a thought of

improving ductility is in fact to limit propagation of an individual shear band and distribute the plastic strain over many shear bands [21]. Practically, following this idea, two categories of approaches are proposed for the ductility enhancing purpose.

1.2.1. Enhanced by geometrical constraints

One way to enhanced ductility is to impose geometrical constraints onto the shear band propagation, which could be achieved by a couple of approaches. Some researchers increase ductility by coating a thin layer of film onto the bulk metallic glasses. Since motion of the shear bands is restricted when propagating to the substrate/film interface and multiple shear band formation is stimulated, the ductility of the metallic glass is increased by 3~10 times [59-61]. One of such examples is presented in Fig. 1.10 [60].

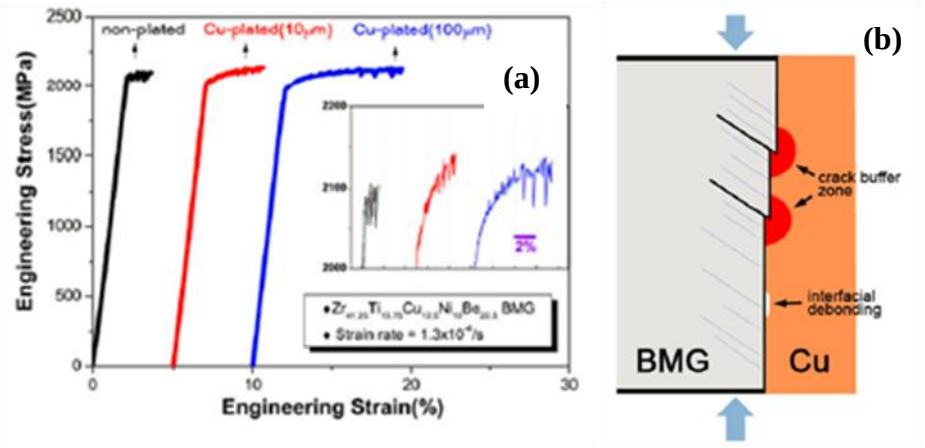

Figure 1.10 Enhancing ductility of the metallic glass by Cu coating and (b) schematic illustration of the enhancing mechanism [60].

In addition, some other people enhance ductility of the metallic glasses by artificially creating a stress gradient [62]. Such a stress gradient will introduce the stress concentration locally and promote formation of multiple shear bands and hence increase the ductility, as shown in Fig. 1.11. Other geometrical constraints to enhance ductility include rolling or bending [63], laminated composites in which layers of ductile metals alternate with layers of metallic glasses [64, 65] and porous metallic glasses in which randomly distributed pores play a role of restricting motion of the shear bands [66, 67].

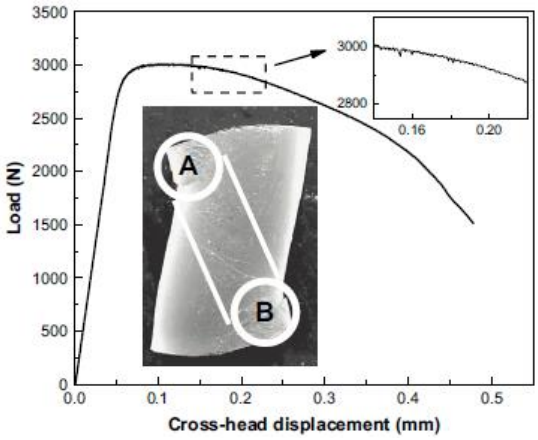

Figure 1.11 Enhanced ductility of the bulk metallic glass by artificially creating a stress gradient [62].

1.2.2. Enhanced via bulk metallic glass composites

Another way is to fabricate composite materials consisting of an amorphous matrix and crystalline phases. The crystalline phases can help induce initiation of a large amount of shear band and inhibit the shear band propagation. Possible approaches to

introduce crystalline phases into the amorphous matrix include partial devitrification of a metallic glass, forming in situ metallic glass composite through precipitation of the crystalline phases during solidification and produce ex situ composites by adding second-phase particles in to a melt [68-72]. For instance, a bulk metallic glass with soft dendrite inclusions can possesses substantially good ductility, as shown in Fig. 1.12 [73].

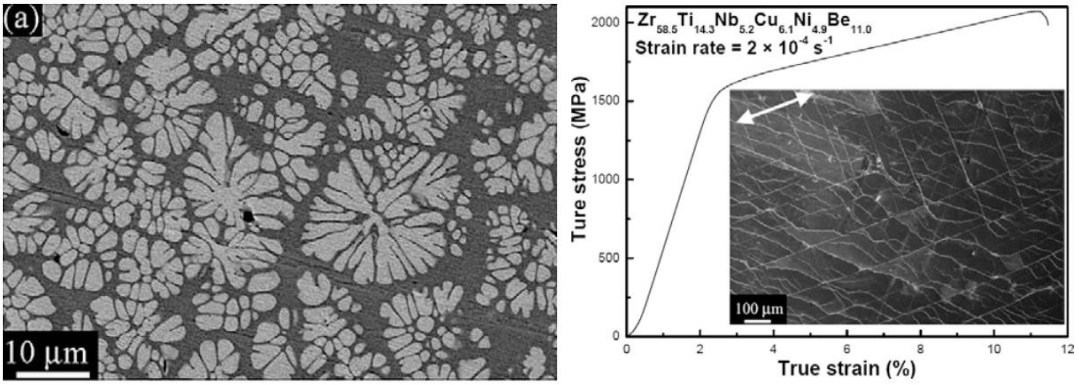

Figure 1.12 (a) Scanning electron microscopy of the Zr-based bulk metallic glass composite with dendrite crystalline phases. (b) Corresponding strees-strain curve showing substantially improved plasticity. The inset shows the deformed metallic glass composite [73].

During deformation, significant stress concentrations will be developed around the second-phase particles. This will trigger formation of multiple shear bands since a yield criterion could be easily satisfied around these particles. The stress concentration at the matrix/precipitate could contribute to residual stress caused by thermally mismatched strains [74, 75], differences in elastic properties [76] and the plastic deformation mismatch [77].

1.3. Fracture Behaviors of the Metallic Glass

Due to characteristic amorphous structure, fracture behaviors of many metallic glasses are much like that in oxide or silicate glasses. However, this does not mean fracture of all metallic glasses is brittle. In reality, the fracture behavior the metallic glasses could be in either ductile or brittle manner, depending on a couple of factors [78-80]. Note ductile fracture here in the metallic glass is not the same as that in the crystalline materials due to lack of the dislocation micromechanism, although some metallic glasses do possess toughness comparable to the crystalline materials. Fracture is considered ductile if large plastic deformation is involved. The fracture surface morphology in the ductile fracture exhibits typical vein pattern, as shown in Fig. 1.13 [80-82]. By contrast, brittle fracture occur with zero plasticity and usually has a relatively flat surface with very fine vein pattern that only can be observed at high magnifications [80].

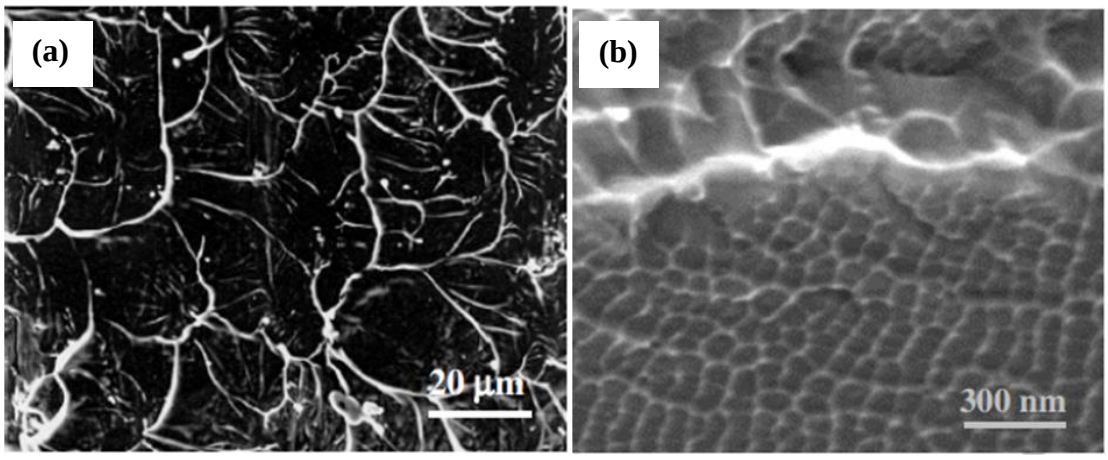

Figure 1.13 (a) Scanning electron microscopy of fracture surface of the ductile metallic glass, showing the characteristic vein patter. (b) Fracture surface of the brittle metallic glass, in which the vein pattern can only be observed at a large magnification [80].

Sharp ductile-brittle fracture transition was also observed. Basically, annealing induced structural relaxation and devitrification could transform the metallic glass from ductile fracture to brittle fracture [82, 83], which was attributed to the free volume drop [84, 85].

However, the free volume is only a conceptual stuff and is not persuasive to account for brittle or ductile fracture in the metallic glasses. Investigation on a large collection of the metallic glasses finally makes Lewandowski and co-workers correlate the fracture energy G_c with their elastic properties. To be specific, they believe metallic glasses with Poisson's ratio υ>0.41 tends to have large fracture energy and hence fracture plastically. On the contrary, metallic glasses with small Poisson's ratio fracture in the brittle manner. Alternatively, metallic glasses with μ/B<0.41 are tough, while those with μ/B>0.43 are brittle, with μ and B being the shear modulus and bulk modulus [86], as shown by Fig. 1.14. Poisson's ratio and μ/B can be correlated by $\frac{\mu}{B} = \frac{3(1-2\upsilon)}{2(1+\upsilon)}$.

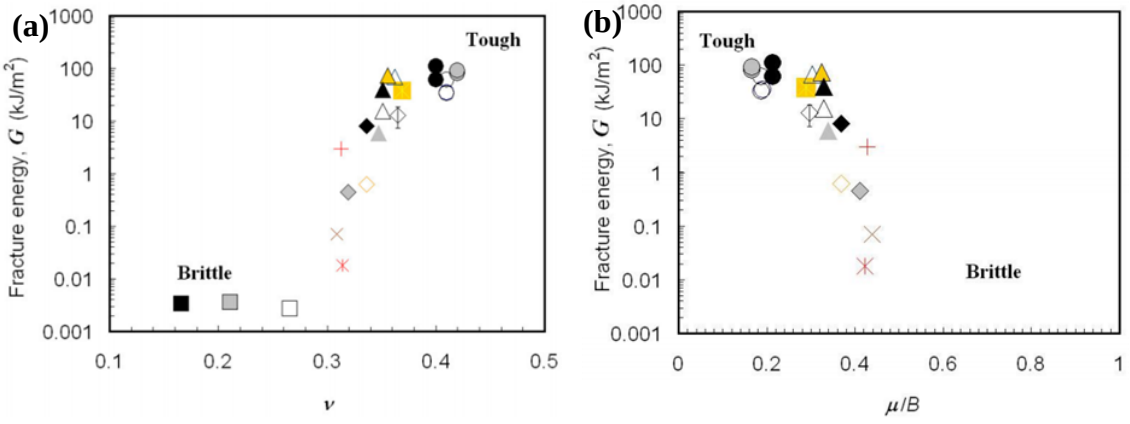

Figure 1.14 (a) Variation of the fracture energy with Poisson's ratio and (b) bulk-to-shear modulus ratio. Both shows sharp brittle-to-ductile fracture transition at certain a critical value [86].

This argument is interpreted as a competition between the shear and dilatation [46]. A low value of *G* is weakly resistant to plastic shear deformation, while a large *B* indicates strong resistance to the dilatation necessary for mode I crack propagation [21, 68].

1.4. Motivation and objectives

Invention of the metallic glass has been over half a century and the bulk metallic glasses have also emerged for over 30 years. Unique mechanical properties of the metallic glasses have attracted extensive scientific interests. Particularly, success of fabricating bulk metallic glasses with featured dimension larger than 1 mm makes people see the hope of driving the metallic glasses into practical applications. However, these nice wishes were found hard to be realized, which are mainly hindered by intrinsic brittleness of the metallic glasses. With unremitting research efforts, it is increasingly realized that without fundamental understanding, it is impossible to prompt the metallic glasses into industrial applications. Researches then turn to study essential deformation mechanisms of the metallic glasses and develop approaches to prevent brittle failure and enhance ductility of the metallic glasses. Among various research efforts, investigating inhomogeneous deformation mechanism of the bulk metallic glass has become very popular. This is because catastrophic fracture normally occurs when the inhomogeneous deformation begins through formation of a dominant shear band. Accordingly, shear band behaviors of the metallic glasses is of special interest.

Given aforementioned development traces of metallic glasses, the present work intends to investigate how the shear band inside the metallic glass controls ductility or brittleness. To be specific, the following scientific issues will be addressed:

(1) Size effect study in the metallic glass. The size effect in the metallic glasses has been widely studied using the micro- or nano-pillar samples. Some reported that when the size of the pillar samples were brought down to a critical value, like 200 nm, the deformation of the metallic glass would become homogeneous and brittle failure could be avoided. However, some others claimed that the size effect was not supposed to be existing in the metallic glass because of absence of dislocation mediated plasticity like in the crystalline materials. If the size effect does exist as that in the crystalline materials, fabricating small sized metallic glasses can provide products combining the high strength and good ductility, and the real application of the metallic glasses would be hopefully realized in MEMS. Accordingly, size effect study in the metallic glasses is of much significance. Study on this can be found in Chapter 2.

(2) How the shear bands develop under multiaxial stress states in indentation. Indentation on the bulk metallic glasses generally introduces multiaxial stress states, which help prevent brittle failure of the metallic glasses. Visualizing the shear band pattern under indentation and examining how they are formed and interact with each other is useful in understanding mechanisms that contribute to prevention of the brittle fracture. This part is also included in Chapter 2.

(3) Enhanced ductility in the thin film coated bulk metallic glasses and metallic glass composites. To push the metallic glass into industrial applications, seeking various possible ways to enhance its ductility has been a vital practice in the metallic glass community. Coating the bulk metallic glass with a thin layer of ductile metals fabricating metallic glass composite containing reinforced crystalline phases were found to be effective in increasing ductility. Studying the ductility enhancement mechanism in these samples can help design optimal methods to resolve the long-standing brittleness issue existing in the metallic glasses. Investigation on this work is in Chapter 3.

(4) Spherical nanoindentation is an important technique for probing mechanical properties of metallic glasses and many other materials, including elastic modulus, hardness and fracture toughness. The accuracy of the testing results largely depends on the correctness of the indenter tip radius and influence of the machine stiffness. In practice, the indenter tip normally does not present a perfect spherical shape, which is determined by the manufacturing process. Accordingly, the indenter tip radius given by the manufacturers are unbelievable. Although fitting with the Hertzian theory could give acceptable tip radius value, it still possibly become give incorrect values when subjecting to influence of other factors, like the machine stiffness. The machine stiffness becomes particularly important at high load levels. Given these facts, it is a necessity to accurately evaluate the indenter tip radius and machine stiffness. This is present in Chapter 4.

(5) The structure-property relationship in the metallic glasses. The amorphous structural nature of the metallic glass makes it pretty difficult to characterize it structure

with conventional experimental techniques like the crystalline materials. Without necessary structural knowledge, many long-standing fundamental mechanical behaviors of the metallic glass, like the shear band mechanism and ductile-to-brittle transition, can not be unveiled. Consequently, it is an imperative task to explore proper approach to establish an effective structure-property relationship. This work can be found in Chapter 5.

A general introduction on the metallic glass is given in Chapter 1 and discussions and perspectives are presented in Chapter 6.

CHAPTER 2

Shear band prediction under geometric constraints

2.1. Introduction

Deformation of the metallic glasses can be divided into homogeneous and inhomogeneous counterparts. The homogeneous deformation normally happens at elevated temperatures, at least above the glass transition temperature and large deformation can be achieved, while the inhomogeneous deformation occurs at low temperatures with formation of shear bands. The metallic glasses accommodated by the inhomogeneous deformation generally exhibit limited plasticity, which is a great obstacle for its commercial applications. Accordingly, studying the shear band governed deformation mechanism in the metallic glasses is fundamentally important for avoiding brittle failure and improving ductility. In this sense, one the one hand, it is suggested that when the size of the metallic glass sample is reduced to nano or micron-scale, the shear banding will disappear and the deformation will transform from inhomogeneous to homogeneous mode. On the other hand, multi-stress state is believed to be able to impose geometric constraints to the deformation and hence help improve ductility of the metallic glasses. In the following, these two subjects will be studied with simulation methods, given the modeling could give novel perspectives on the problem identification and solution. Meanwhile, necessary experiments are carried out as well.

2.2. Shear bands in BMG nanopillars[1]

One of the most intriguing questions in the recent development of nanoscience is whether the fundamental laws of physics would break down when the characteristic dimension of the test sample approaches the dimension of atoms (i.e. the subnanometer scale). It is conceivable that when the critical dimension is reached the properties of the sample will undergo a drastic change, the so-called "size effect".

In the case of metallic glasses, the deformation can be divided into inhomogeneous and homogeneous deformation. Homogeneous deformation occurs typically near and above the glass transition temperature (T_g) [87]. By contrast, inhomogeneous deformation typically occurs at ambient temperature well below the T_g and the deformation mode is localized shear band formation [88]. Many attempts have been made to assess the critical sample size below which shear band localization disappears and the sample deforms homogeneously [89-98]. Based upon scanning electron microscopy (SEM) observations of de-formed pillar samples, the length scale necessary for homogeneous deformation to prevail was claimed to be less than 100 nm [89, 90, 92], Volkert et al. [91] reported that the length scale at the transition from shear band localization to homogeneous deformation occurred in 400 nm pillar. In comparison, Chen et al. [93] predicted 200 nm to be the minimum length scale below which a shear band would not form. On the other hand, Schuster et al. [99] and Dubach et al. [100] claimed that there is no evidence of deformation

[1] This work was completed with collaboration with M.C. Liu et al. at National Sun Yat-Sen University. They did the experiments and our side at University of Tennessee did the modeling analysis. Refer to Liu MC, et al. Scripta Mater 2012;66:817.

mode transition at a pillar diameter as small as 200 nm. Wu et al. [97] also conducted an in situ compression experiment, using a 150 nm diameter pillar in a trans-mission electron microscope, and concluded that there was no size effect. Despite these research efforts, it is still unclear whether there exists an inhomogeneous to homogeneous transition [101, 102]. Moreover, Kuzmin et al. [103] recently investigated experimentally the size effect on the inhomogeneous-to-homogeneous deformation transition in a bulk metallic glass and showed the effect of sample tapering. They demonstrated that taper-free pillars with smaller diameters would exhibit ductile behavior during compression almost without shear banding.

It is worth noting that most of these size-effect studies used micro- or nanopillar samples fabricated by focus ion beam (FIB) techniques [104], with only a few exceptions [105]. It is also known that FIB can cause damage to the sample surface and subsequently change its properties [96, 106, 107].

Moreover, the ion beam is not a delta function but has a Gaussian distribution. This results in the production of tapered pillar samples with a dome-shaped top. The exact shape of an FIBed sample is dependent upon the energy and angle of the incident ion beam. Usually, the curvature of the dome top becomes sharper when the diameter of the pillar sample is reduced. The taper and the non-flat top make plastic analysis difficult. It is conceivable that testing of dome-shaped pillar samples could lead to some misinterpretations of plasticity. However, for brevity, we will not discuss the effect of the dome shape here but, rather, will focus on the effect of sample tapering.

To study the effect of sample tapering on the plastic deformation mode, our collaborators, M.C. Liu, J.C. Huang and K.W. Chen et al. at National Sun Yat-Sen University and National Cheng Kung University performed in situ compression tests in a transmission electron microscope on the ZrCu pillar samples fabricated by FIB. We (University of Tennessee side) carried out, in parallel, finite element simulations of the compressive deformation and compared with the experimental observations.

2.2.1. Experimental details

Experimental samples with composition of $Zr_{50}Cu_{50}$ were deposited on Si (100) wafers by the magnetron co-sputtering method using the parameters developed by Dudonis et al. [108]. The total amorphous film thickness was fixed at ~1500 nm. The nature of as-deposited thin films was characterized by X-ray diffraction (Siemens) and transmission electron microscopy (TEM; JOEL 3010). To further explore the microscale mechanical properties of the as-deposited thin films, nanopillars were pre-pared from the resultant films using the dual FIB system (Seiko SMI3050 SE). In situ TEM compression tests were conducted by a novel and recently developed Hysitron pico-indenter TEM holder (Hysitron Inc., Minneapolis, MN) on a JEOL 2010F transmission electron microscope, equipped with a diamond flat punch, 1.5 lm in diameter. The nano-compression is also performed in the displacement-control mode and the corresponding strain rate is 5×10^{-3} s^{-1}. Nanopillar samples with a length of ~1.5 lm were fabricated by FIB. These nanopillars have a 140 nm diameter top and an ~250 nm diameter bottom. The aspect ratio is > 6, which is higher than the aspect ratio of 2–5 convention-ally used

for compression specimens. Such a high aspect ratio was used in order to minimize possible accidental collision between the indenter tip and the sample base.

2.2.2. The free volume model

The free-volume model, proposed by Spaepen, is a classic constitutive description for MGs, which assumes that the macroscopic plastic flow occurs as a result of net forward atomic jumps in the direction of the applied stress in a pure shear case [109]. The general flow equation can be represented as:

$$\frac{\partial \gamma}{\partial t} = 2fexp(-\frac{\alpha v^*}{v_f})\exp(-\frac{\Delta G^m}{k_B T})\sinh(\frac{\tau \Omega}{2k_B T}) \quad (2\text{-}1)$$

where f is the frequency of the atomic vibration, α is a geometric factor of order 1, v^* is the hard-sphere atomic volume, v_f is the average free volume per atom, ΔG^m is the activation energy, Ω is the atomic volume, τ is the applied shear stress, k_B is the Boltzmann constant, and T is the absolute temperature. The average free volume, v_f, is treated as the order parameter and controls the structural change in MGs. The structural rearrangement with the applied stress is controlled by the competition between a stress-induced disordering process and a diffusional reordering process. Consequently, the net increase of the free volume is given as:

$$\frac{\partial v_f}{\partial t} = v^* f exp\left(-\frac{\alpha v^*}{v_f}\right)\exp\left(-\frac{\Delta G^m}{k_B T}\right)[\frac{2\alpha k_B T}{v_f C_{eff}}\left[\cosh\left(\frac{\tau \Omega}{2k_B T}\right) - 1\right] - \frac{1}{n_D}] \quad (2\text{-}2)$$

where n_D is the number of atomic jumps needed to annihilate a free volume equal to v^* and is usually taken to be 3 - 10, and the effective elastic modulus is $C_{eff} = E/3(1-v)$.

The trend is a stress-controlled process. At a low-stress level, the free volume created by the stress can be readily annihilated, and homogeneous deformation is maintained, while at a high-stress level, a net increase in the free volume arises, and, hence, shear banding occurs. Equations (3) and (4) form the basis of the constitutive relation, which can be applied for both homogeneous and inhomogeneous flows in MGs. The flow equation is generalized into a multiaxial stress state with the small-strain, J_2-type viscoplasticity framework and implemented in the ABAQUS model using an user-defined material subroutine written by Gao [110].

2.2.3. In-situ TEM observation

Several predetermined displacements (100, 200 and 300 nm) were initially selected for the in situ compression of ZrCu nanopillars. After several trials, it was found that only displacement >200 nm produces sufficiently useful results. Subsequently, most examinations were conducted on samples compressed to a displacement of 300 nm. The load–displacement (similar to engineering stress– strain) curves from several samples are summarized in Fig. 2.1. There are some variations in the data, probably caused by the initial misalignment of samples, though the shapes and trends of the curves are similar. The yield strength is obtained from the departure of the linearity of the early portion of the curve. Because the sample is tapered, yielding will occur from the top of the sample, which is the location with the smallest cross-sectional area. Accordingly, the yield strength can be extracted from the departure load divided by the top area. The yield strength varies between 1.8 and 2.5 GPa, which are within the range reported in the

literature [97, 111, 112].

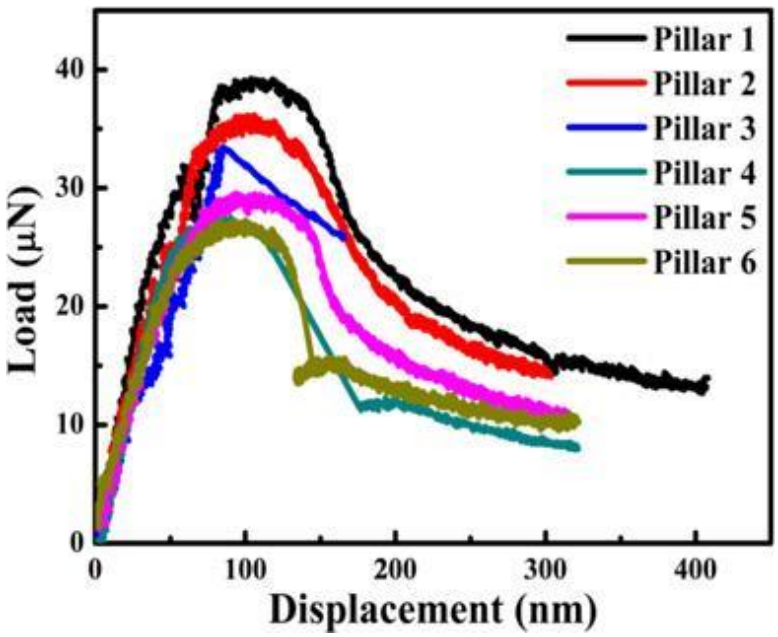

Figure 2.1 Representative stress–strain curves for nanocompression tests on the ZrCu thin film metallic glass pillars [112].

The compressive load typically reaches its maximum level at a displacement of about 75 nm, followed by a gradual decrease. This load decrease resulted from severe buckling or bending, as will be shown below for the in situ TEM observations. The bending or buckling phenomenon is inevitable due to the sample high aspect ratio (~6) and, possibly, sample bending due to misalignment. In fact, it has been pointed out by Zhang et al. [113] that bending or buckling is significant when the aspect ratio of the test pillar is greater than 5. Therefore, for the current ZrCu nanopillars, the reasonable

maximum compressive strength without significant buckling or bending should be the upper-bound value of about 2.0–2.5 GPa.

To view the in situ deformation, a series of cropped TEM video frames recording the deformation of ZrCu nanopillar are shown in sequence in Figure 2.2(a)–(h), together with the corresponding load–displacement curve (inset). The bottom part of the sample (gray area) is the silicon substrate. The pillar is tapered (~3^{o}). Perfectly aligning the nanometer-sized compressive sample is so difficult it is almost impossible to achieve. As shown in Figure 2, the sample axis is slightly off the compressive axis (~2-3^{o}). To simplify the analysis, we ignore the effect misalignment in this paper. Sample misalignments will lead to preferable initiation of shear bands from the pillar corner, and these shear bands may not propagate through the entire sample because of the additional bending stress [62, 101]. While these effects are also present in our work, the sample taper plays a more intriguing role in confining shear bands to the pillar top. Our free-volume constitutive law and finite element simulations later on in this paper are essentially the same as those used by Wu et al. [62], from which we can qualitatively understand the misalignment effects. Thus, in our following analysis, we focus on the sample tapering effects.

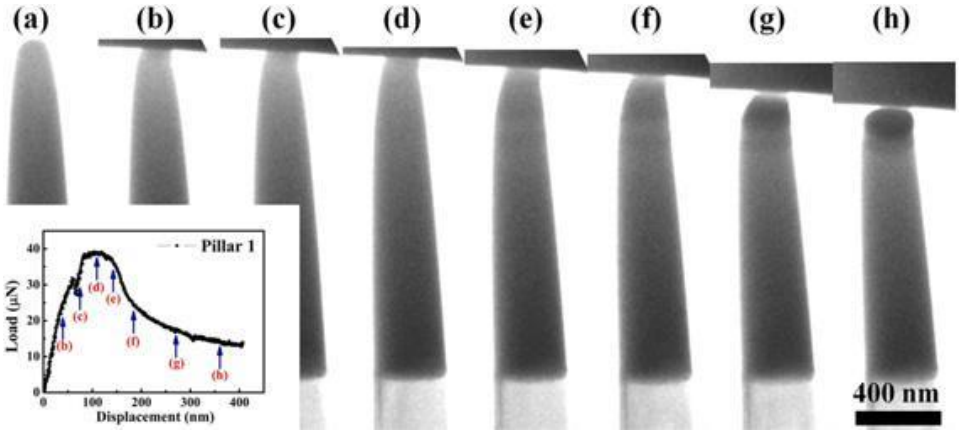

Figure 2.2 Video snaps taken from the in situ TEM compression showing the deformation of a Zr-based pillar (Pillar 1). The different stages of the nanocompression process are depicted by individual frames (a–h) at different strains: (a) undeformed, (b) ~2%, (c) ~4%, (d) ~6%, (e) ~8%, (f) ~10%, (g) ~15%, (h) ~20%. The corresponding stress–strain curve is inset at the bottom left corner for point-to-point correspondence [112].

Plastic deformation in the sample is noted to be local, occurring mainly in the upper portion of the sample. The change in cross-sectional area as a function of distance from the top of the pillar sample after being deformed 300 nm is shown in Figure 3(a). Apparently, the dimension of the bottom part of the sample remains practically unchanged even after being compressed to a 300 nm displacement. This is primarily because metallic glasses are perfectly plastic materials and the test sample is tapered. The strain localization near the top of the sample was additionally supported by the observation that the initial TEM contrast of the top part of the sample was brighter, resulting from a smaller diameter because of tapering. After compression, the top part of the pillar gradually became darker as a result of increasing diameter. It is particularly

noted in Fig. 2.2 that, despite the strain localization near the top of the sample, there is no visible evidence of localized shear across the sample and the de-formed sample has a mushroom-shaped top, just like that observed by Volkert et al. [91]. According to the conventional wisdom, one would conclude that the pillar was homogeneously deformed; however, this is not, in fact, the case. As demonstrated later in the simulation on tapered nanopillars, shear bands initiate from the contact corner between the sample and punch and form an in-verse cone, with the tip of the cone located along the centerline of the compressive axis.

Whereas an SEM micrograph can show the three-dimensional (3-D) morphology of a deformed pillar and the presence of surface offset caused by shear banding, TEM only provides a 2-D view. It is therefore hard to detect the sudden formation of individual shear bands from the current TEM images. The difficulty is caused by the facts that the width of a shear band is particularly thin (~10–20 nm), requiring the use of a high-resolution TEM for observation [114], and also because shear band propagation speed is extremely rapid (~4 mm s^{-1}) [115]. It is estimated to take less than 0.1 ms to propagate a shear band through the entire pillar sample. However, the current TEM video speed is only 13 frames s^{-1}; thus there is insufficient temporal resolution to capture shear bands. Also, the pillar specimen fails after deformation, and cannot be examined by lattice imaging to search for the possible existence of shear bands.

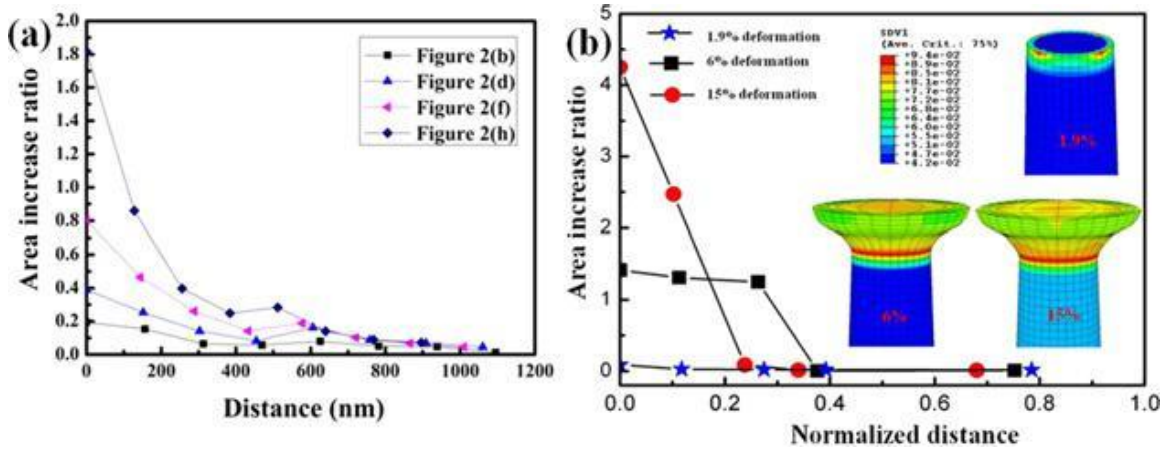

Figure 2.3 (a) Change in cross-sectional area vs. distance for Figure 2.2(b), (d), (f) and (h). Distance stands for distance at the top of the pillar sample. (b) Area change ratio as a function of the distance from the specimen top (normalized by the base diameter) at three representative deformation stages, with free volume contours in the insets. Contour plots are given in the deformed mesh, with displacement magnification ratios being 1 in all three directions.

2.2.4. Prediction with the free volume model

To investigate the tapering effects on the shear band formation and deformation behavior, finite element simulations were performed using the free volume model [28, 58]. Our simulations are based on the nonlinear finite element method developed previously [58]. A 3-D tapered pillar with the aspect ratio of 4 was constructed for simulation in ABAQUS, with a total number of 38,401 C3D8 elements. A flat-ended indenter is used to apply the compressive load from the above while the sample bottom is completely clamped. The constitutive parameters were specified as $\bar{v}_f = 0.05$, and a Poisson's ratio

of 0.333. The normalized loading rate $(\dot{L}/L_0)\exp(\Delta G^m/K_B T)$ can be calculated to be 2.5×10^{-6}, where $\dot{L}$ is the strain rate and L_0 is the original length of the sample.

As a result of sample tapering, the stress distribution in the initial elastic stage of compression test is non-uniform. Usually, for a Mises solid obeying classic continuum plasticity, the plastic zone gradually extends from the pillar top to the entire sample, and the entire deformation history is smooth and continuous, as shown in Fig. 2.4(a). The taper angle has an insignificant effect on the final barrel-like deformed shape. For metallic glasses, however, the scenario is radically different. Strain localization in the form of shear band is initiated near the pillar top because of the stress concentration. This is clearly shown in Fig. 2.4(b), in which a series of shear bands are initiated symmetrically from the top edge of the specimen and keep propagating downward toward the center until an inverse cone is formed. Macroscopically, this did not lead to large shear displacement, nor a large discontinuous shape on the surface. In other words, the shear bands are formed inside the pillar and are not observable on the sample surface. Thus, the shear band trace and the shear band offset cannot be observed easily under in situ TEM. Continuous deformation after the cone is formed would lead to the spread of localized deformation, but would still be confined to the vicinity of the top of the pillar.

A view of the entire sample deformed to a large strain is shown in Fig. 2.3(b). It is evident that there is a drastic increase in the cross-sectional area, although the absolute strain level is generally small except in the shear bands. The shear bands are contained inside the pillar and are therefore not observable from the outside. In contrast to the

catastrophic failure in large pillar compression tests, these shear bands will not evolve into cracks be-cause the taper angle results in a geometric hardening effect. The slight work hardening is an artifact resulting from tapering of the pillar sample, and the ever-increasing cross-sectional area during compression testing.

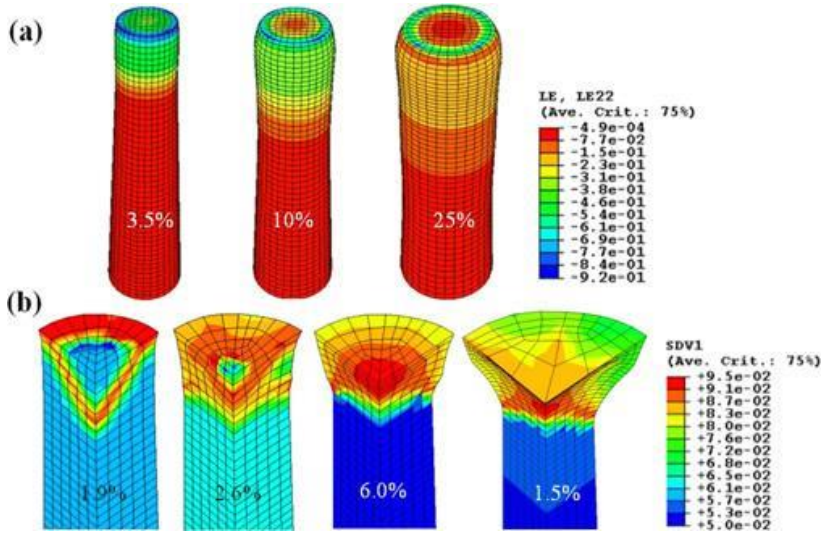

Figure 2.4 (a) Compression of a Mises plastic pillar with a stiffness to yield stress ratio of 240; (b) compression of the same pillar but with the free volume constitutive law (where SDV1 indicates the free volume). Barreling deformation can be seen in the Mises solid. By contrast, highly localized deformation of metallic glass occurs with the shear band evolution procedure demonstrated by the free volume contour, which is given in the deformed mesh, with displacement magnification ratios being 1 in all three directions.

The comparison between the simulations and experiments indicate a significant effect of the taper angle, so that the deformation becomes highly localized near the top and the resulting force–displacement curve cannot be directly or easily translated into the

constitutive behavior of the material. It is also noted that our predicted area change ratio is much larger than in experiments (Fig. 2.4(a)), which is mainly due to the misalignment-induced bending in the experiments that accommodates the compressive displacement. Nevertheless, the general trends for the experiment and the simulation are similar.

2.2.5. Summary

According to the findings in section 2.2, it is anticipated that inhomogeneous deformation prevails down to 140 nm pillars. First, if homogeneous deformation were to dominate at small scales, localized deformation near the tip of the tapered pillars would not have occurred. Fully homogeneous deformation, such as the superplasticity behavior that occurs in many crystalline metals [116], would lead to uniform straining throughout the specimen. Both the taper angle and the tip rounding do not change the general deformation behavior, while the degrees of deformation localization depend on these two parameters. Second, previous observations of inhomogeneous to homogeneous deformation are often explained by the lack of mechanical energy input when the pillar size is reduced. In fact, it is well known that whether strain localization leads to a sudden load-drop or to catastrophic failure depends on the mechanical stiffness. Shear bands may not be observable in small-sized pillars because they are often inside the pillar, as shown by our simulations in Fig. 2.3(b). Finally, we note that a constitutive model incorporating a length scale would truly predict the transition from inhomogeneous to homogeneous deformation mode. However, the experiments presented here found localized

deformation even for 140 nm pillar, suggesting that such a length scale will be much smaller. This agrees with the hypothesis that a material's length scale is governed by its free volume diffusion or other atomistic mechanisms. In summary, compressive testing of tapered pillar samples with an aspect ratio of 6 is not a viable technique for the identification of the transition from inhomogeneous to homogeneous deformation mode in metallic glasses.

2.3. Shear band pattern under indentation[2]

2.3.1. Motivation

Experimentally, shear band under indentation can be visualized by the bonded-interface technique [117-124]. In this technique, two samples are bonded together using the super glue and subsequent indentation is made in to the center, as shown in Fig. 2.5(a). After indentation, the shear bands on the bonded interface can be observed by splitting two bonded parts. It is found the bonded interface contains two family of shear bands: radial shear band, like these blue curves, and semi-circular shear bands, like these red curves as demonstrated in Fig. 2.1(b). However, since the stress fields will be significantly affected by the interface, it is necessary to understand whether the experimentally observed shear band using the bonded interface technique represent actual ones when the interface is absent.

[2] This work was done by collaborating with Z.N. An at University of Tennessee. Z.N. An predicted the shear band directions under indentation with the Rudnicki-Rice instability theory, while W.D. Li did that using the free volume model.

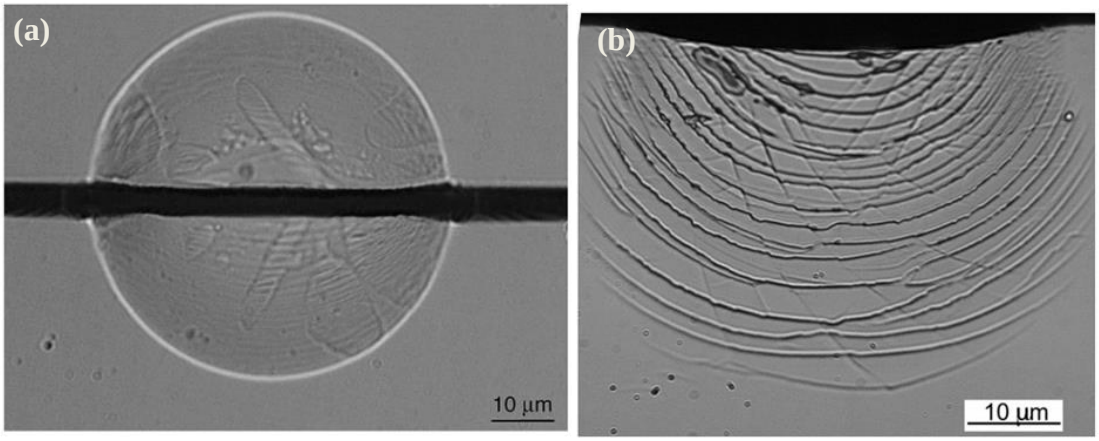

Figure 2.5 (a) $Zr_{52.5}Al_{10}Ti_5Cu_{17.9}Ni_{14.6}$ bulk metallic glass sample indented with the bonded interface technique. (b) Shear bands observed on the bonded interface after splitting two parts and removing the super glue [125].

Predictions with the Rudnicki-Rice instability theory by Z.N. An found that [126] when the bonded-interface is absent, only the radial shear bands are formed, as depicted in Fig. 2.6 (a). As a bonded-interface is present, which is realized by releasing the motion in the direction normal to the symmetric surface in a 3D half-symmetric finite element model, both the radial shear bands and the semi-circular shear bands are observed, as shown in Fig. 2.6 (b). Based on these theoretical predictions, it appears that the semi-circular shear bands observed in experiments are a result of stress relaxation of the bonded-interface in practice. To confirm this, further studies with the free volume model is performed, given its capability of predicting shear band propagation paths.

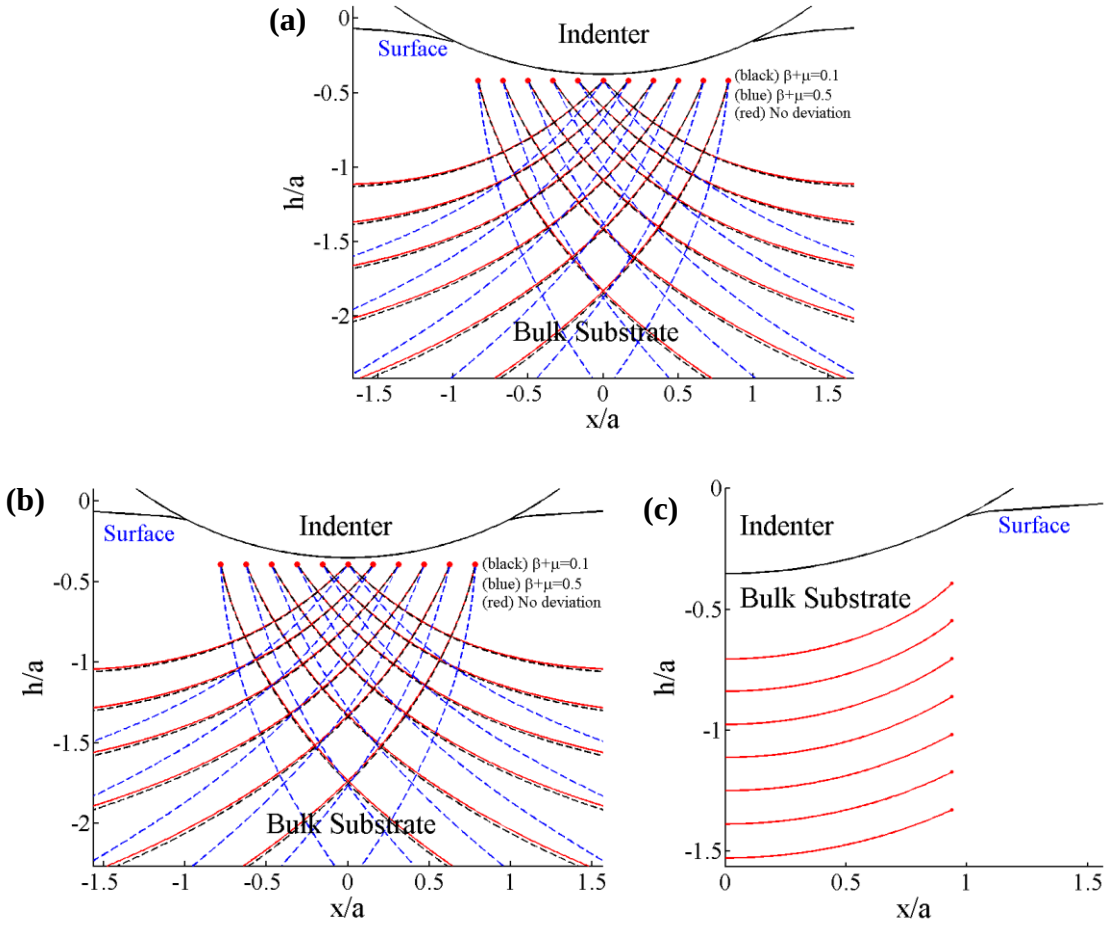

Figure 2.6 (a) Shear band patterns on the half-symmetric interface of the metallic glass substrate (without interface constraints) under spherical indentation. (b) Radial shear bands and (c) semi-circular shear bands on the half-symmetric interface of the bonded interface metallic glass substrate under spherical indentation [126].

2.3.2. Direct spherical indentation

The Fig. 2.7 shows the finite element model used for predicting shear band behavior under indentation. Because of symmetry, a quarter of the substrate was constructed for 3D indentation simulation using 37,490 C3D8 elements in ABAQUS, and

the region underneath the indenter was finely meshed for accurate calculation consideration. The spherical indenter was modeled as a rigid body with a radius of R and the contact between the indenter and the substrate was frictionless. Symmetric boundary conditions were assigned to two lateral faces (normal to positive X and positive Z) and the bottom was completely pinned. Specifically, the initial free volume is given by $v_f/\alpha v^* = 0.05$, and other constitutive parameters are $E\Omega/2k_BT = 240$, ν =0.333, $n_D = 3$, α =0.15, and v^*/Ω =1. The normalized loading rate is $\frac{\dot{h}}{Rf}\exp\left(\frac{\Delta G^m}{k_BT}\right) = 3.0\times10^{-7}$. When $a/R \approx 0.14$, the first shear band has initiated and extended to a distance of about $0.5a$.

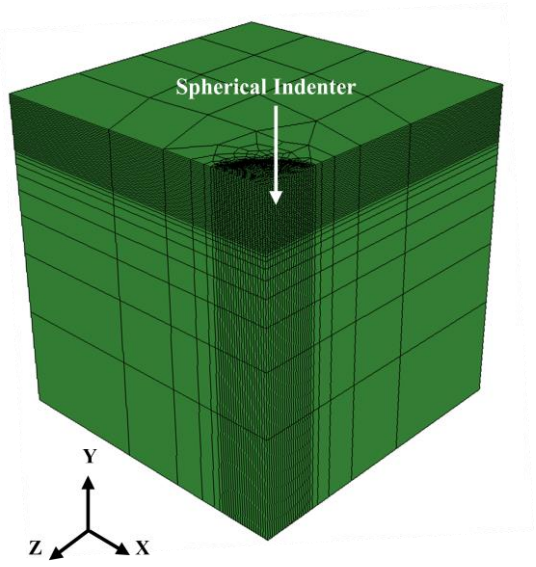

Figure 2.7 Finite element model used for predicting shear band under spherical indentation.

Two interesting observations can be obtained from the cut-and-view plots in Fig. 2.8. First, the first shear band is actually a conical shear surface, which resembles a radial shear band from the side view. Such a perfect axisymmetry may not be attained in reality because of sample defects or loading misalignment. Second, how far a shear band extends depends on material constitutive parameters and, most importantly, the strain and strain rate fields. Indentation-induced stress fields decay rapidly, so the observed shear bands rarely extend far beyond about twice the contact size.

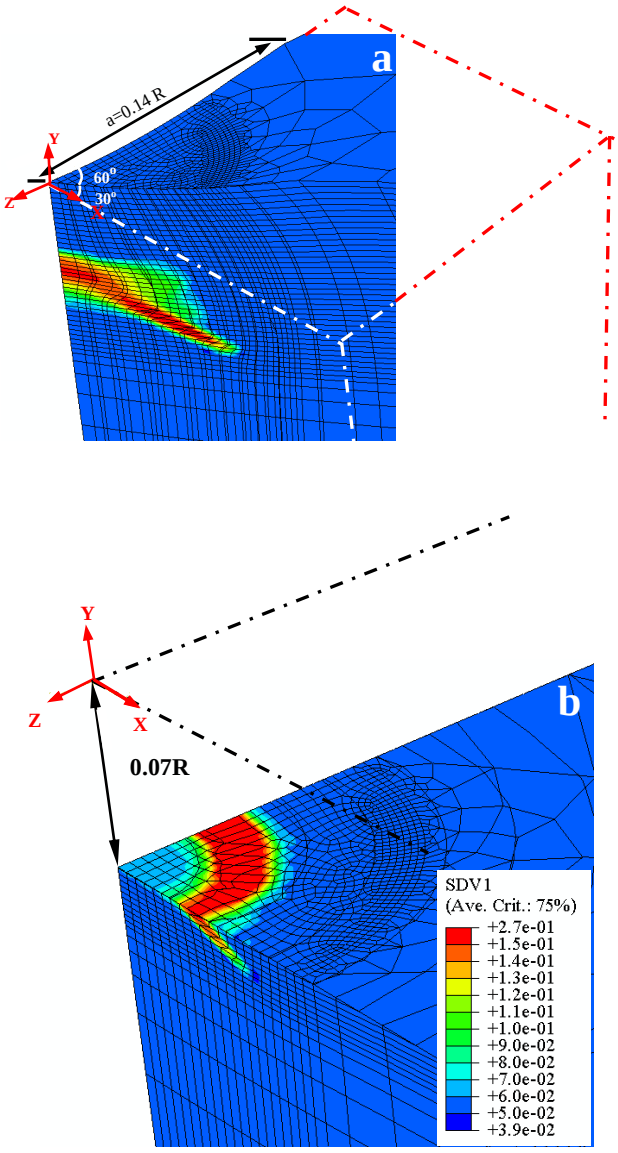

Figure 2.8 To clearly visualize the three-dimensional conical shear band, free volume contours (SDV1) were plotted on a vertical plane that makes an angle of 60º from the backside surface in (a), and on a horizontal plane at a distance of 0.07R below the top sur surface in (b). Finite element simulations were performed in a quarter of the substrate under spherical indentation with symmetry boundary conditions prescribed on the two side surfaces. These plots are given in deformed mesh with displacement magnification ratios being 10, 2, and 10 in X, Y, and Z directions, respectively.

2.3.3. Bonded-interface indentation

The bonded-interface case can be simulated by prescribing traction-free boundary conditions on one side surface as shown in Fig. 2.9. Different from the conical shear surface, a spade-like shear band is initiated inside the specimen but away from the contact axis and then extends to the center of the contact area. Subsequent loading leads to the second shear band initiated on the traction-free surface as shown in Fig. 2.9(c). Note the change of view direction in Fig. 2.9(c). Further simulations were not performed since the shear band simulation suffers mesh sensitivity problem, i.e., shear band width is set by the mesh resolution, and a fine mesh calculation is not readily feasible. The mesh sensitivity problem can be resolved by introducing a length scale in the constitutive law [125, 127]. Nevertheless, these simulations clearly demonstrate that the interface relaxation has a critical effect on the shear band formation, and after the first shear band (which is hidden in the sample), semi-circular shear bands are initiated on the bonded interface.

Figure 2.9 When the traction free boundary condition is prescribed on one side surface, the first shear band becomes spade like with the initiation site marked by "X" in (a). A horizontal cut at a distance of 0.03R below the top surface is given in (b). These two plots are given in deformed mesh with displacement magnification ratios being 10, 2, and 2 in X, Y, and Z directions, respectively. (c) A slight increase of the indentation load leads to the second shear band which is initiated on the free surface, as shown by the free volume contours in undeformed mesh.

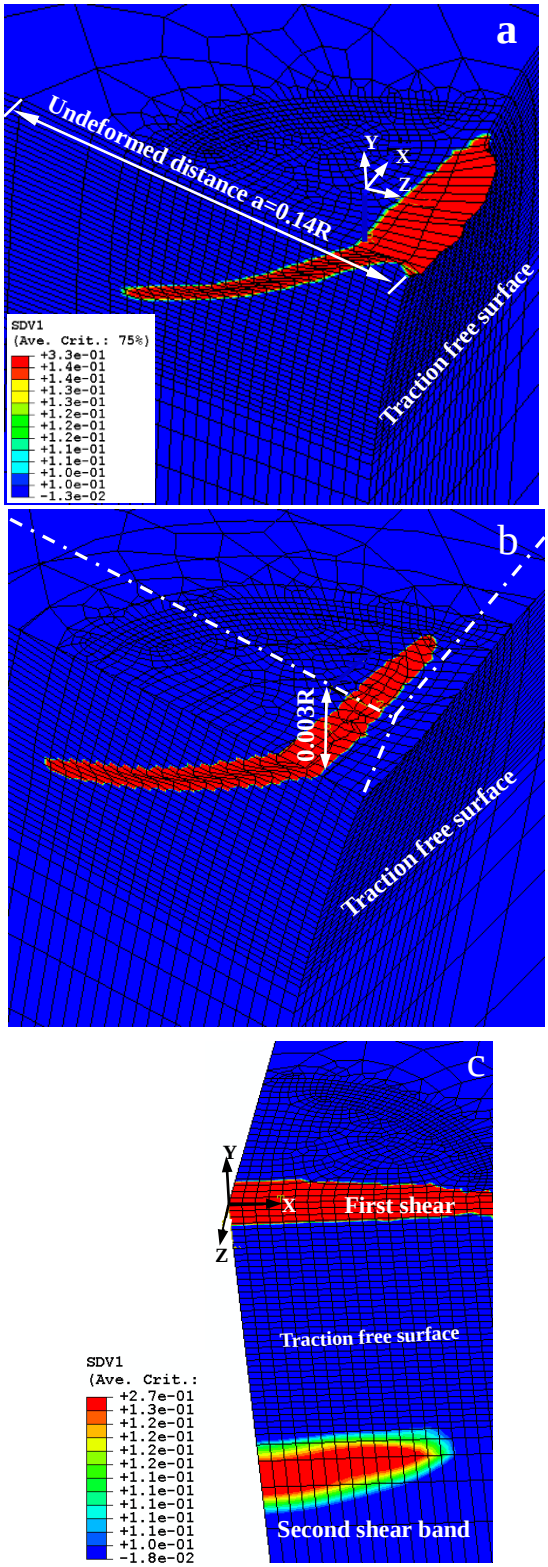
a
Undeformed distance a=0.14R
Y
X
Z
SDV1
(Ave. Crit.: 75%)
+3.3e-01
+1.4e-01
+1.4e-01
+1.3e-01
+1.3e-01
+1.2e-01
+1.2e-01
+1.2e-01
+1.1e-01
+1.1e-01
+1.0e-01
+1.0e-01
-1.3e-02
Traction free surface
b
0.03R
Traction free surface
c
Y
X
Z
First shear
Traction free surface
SDV1
(Ave. Crit.:
+2.7e-01
+1.3e-01
+1.2e-01
+1.2e-01
+1.2e-01
+1.2e-01
+1.1e-01
+1.1e-01
+1.1e-01
+1.1e-01
+1.1e-01
+1.0e-01
-1.8e-02
Second shear band

2.3.4. Summary

Based on the result in section 2.2, it can be concluded that the radial shear bands are actually intrinsic for indentation, while the semicircular shear bands are caused by the stress relaxation on the bonded interface in experiments.

CHAPTER 3

Deformation mechanisms in the coated BMG and BMG composites

3.1. Introduction

Under deformation, the plastic flow in BMGs is accommodated by shear bands, thus, the catastrophic failure happens, due to the unconstraint propagation of individual shear bands. Thus, the most efficient way to improve the ductility is to geometrically constrain these shear bands, so that the plastic strain in each shear band can be minimized, therefore preventing crack initiation from a shear band. The application of surface coatings is a typical approach to constrain the shear-band propagation and, thus, promote the proliferation of shear bands. For instance, Li et al. [128] studied the effect of the nanocrystalline Ni–15%Fe (weight percent, wt.%) coating on a Zr-based BMG and ascribed the ductility enhancement to the increase of the shear-band density. They proposed that the multiplication of shear bands was due to the resistance of the nanocrystalline coating to shear-band propagation at the interface. An alternative to prevent catastrophic failure of the bulk metallic glass along a major shear band is by forming BMG composite. By having certain fractions of second phases randomly distributed in the metallic glass matrix, more shear band initiation locations would be introduced at the second phases/matrix interface. Meanwhile, the shear band propagation could be blocked by the crystalline phase. Both these features will result in formation of

multiple shear bands, which allow strain to be shared by a large amount of shear bands and hence help enhance ductility.

Although the general pictures for enhanced ductility in the coated metallic glasses and metallic glass composites are easy to be understood, explicit micro-deformation mechanisms are still not very clear and needed to be elucidated. For instance, in the coated metallic glasses, what contributes to enhance ductility and what factors affect the effectiveness of the ductility improvement are still unclear. In the BMG composites, how the deformation of the crystalline phases and metallic glass matrix compromise with each other is still need to be understood. Given limitation of experimental techniques, using simulation approach could provide insightful understanding on these issues. In the Chapter, we will use the Rudnicki-Rice instability theory [129, 130] and free-volume model [110, 131] to understanding fundamentals of deformation in the coated metallic glasses and bulk metallic glass composites.

3.2. Enhanced ductility in the coated BMG[3]

3.2.1. Motivation

This work was motivated by experimental observation by our Taiwan colleagues. They found that the bulk metallic glasses coated with thin films, including Titanium film, metallic film and others, have better ductility than uncoated bulk metallic glasses, as shown by the bending tests in Fig. 3.1 [59]. Subsequent indentation tests found that the

[3] This work was completed with collaboration with C. Rullyani and Chu J.P. at National Taiwan University of Science and Technology. They made the experimental observation and we performed modeling.

titanium coated bulk metallic glass has large density of shear band compared to uncoated bulk metallic glass [132], as revealed by the top view of the indented uncoated and coated bulk metallic glasses in Fig. 3.2. Under this background, it is a necessary task to understand what mechanism contributes to enhanced ductility in bulk metallic glasses. Given limitation of experiments, modeling with the Rudnicki-Rice instability theory and the free volume model would be employed to uncover this.

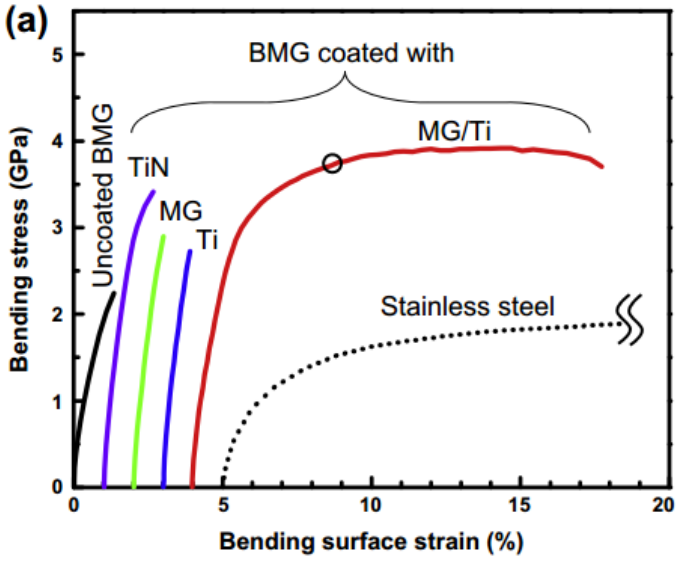

Figure 3.1 Bending stress vs. bending strain for the uncoated bulk metallic glass and coated bulk metallic glasses with different materials [59].

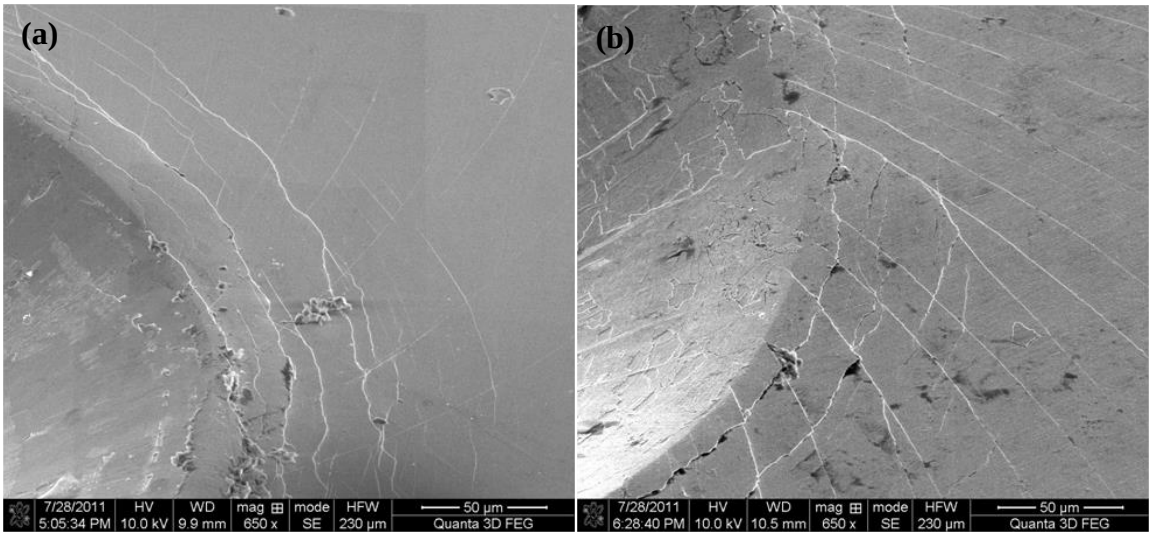

Figure 3.2 Top view of the indented (a) bulk $Zr_{52.5}Cu_{17.9}Ni_{14.6}Al_{10}Ti_5$ (Vitreloy 105) metallic glasses and (b) the same sample coated with 200 nm think pure Ti. More shear bands are observed in the coated sample [132].

3.2.2. Study with the Rudnicki-Rice instability theory

Strain localization is a phenomenon of instability, from continuum mechanics point of view, and can be described by a general bifurcation theory, in which the shear-band is resulted from bifurcation of a homogeneous elastic-plastic flow. The shear band angle in the principal stress space is given by [129, 130]:

$$\theta_0 = tan^{-1}\sqrt{\frac{\xi - N_{min}}{N_{max} - \xi}} \tag{3-1}$$

where $\xi = \frac{1}{3}(1+v)(\mu+\beta) - N(1-v)$, $N_{max} = \frac{\sigma_I^{'}}{\bar{\tau}}$, $N = \frac{\sigma_{II}^{'}}{\bar{\tau}}$, $N_{min} = \frac{\sigma_{III}^{'}}{\bar{\tau}}$, and $\bar{\tau} = \frac{\sigma_{mises}}{\sqrt{3}}$. $\sigma_I^{'}$, $\sigma_{II}^{'}$, and $\sigma_{III}^{'}$ are principal deviatoric stresses. υ is the Poisson's ratio, μ is the coefficient of internal friction and β is the dilatancy factor. Accordingly, the shear-band

plane will make an angle of ±θ with the first principal stress direction and parallel to the second principal stress direction.

To predict the shear-band initiation and propagation under deformation, in coating/substrate systems with a film/substrate thickness ratio of 1/20, compared with the bare substrate case, a three-dimensional (3-D) half-symmetric ABAQUS model under Rockwell indentation was developed, as shown in Fig.3.3(a) [133]. In this model, both the MG substrate and film are treated as a pure elastic body, which means that the deformation behavior of the substrate and coating is merely determined by Young's moduli (E) and Poisson's ratios (v). In our case, E and v for substrate and film are 88.6 GPa, 122GPa, and 0.3, 0.34, respectively. The Rudnicki-Rice instability theory is employed to predict the directions of shear bands for both the monolithic (Fig. 3.3(b)) and coated BMGs (Fig. 3.3(c)) [133], with $\mu + \beta = 0$ in the MG substrate, where $\mu + \beta = 0$ indicates that the materials deformation is pressure insensitive and associative. The detailed explanation on the $\mu + \beta$ from the mechanics point of view can be found in the work [130]. The prediction, from the instability theory, gives typical radial shear-band patterns under indentation for both the bare substrate and film/substrate cases, which is consistent with many reported experimental results [122, 126]. In Fig. 3.3(b), the blue solid curves indicate the predicted shear-band directions, while the red dashed curves are along principal shear stress directions. Since there are no shear-band constraint conditions on the surface of the monolithic BMG specimen, only major shear bands appear and propagate in the MG substrate. However, in the coating/substrate material system, more

shear bands appear, most of which are less than the major shear bands in the bare-substrate case, as shown in Fig. 3.3(c). It can be observed that a lot of short solid black and dashed green curves, which are the corresponding shear-band directions and principal shear-stress directions, respectively, occur at the coating/substrate interface, together with some larger shear bands (blue solid curves). This phenomenon suggests that the local strain of the BMG produced in the deformation process can be dispersed by more shear bands, which reduce the shear strain in each shear band. Therefore, the plasticity of BMG substrate is increased by a surface coating.

Moreover, in the TFMG-substrate material systems, shear bands are "reflected", resulting in the occurrence of more short and minor shear bands (solid curves, Fig.3.3(c)), when major shear bands propagate and arrive at the film/substrate interface during deformation, as shown in Fig.3.3(c). It should be noted that in our simulations, shear bands start from the substrate material, while shear bands can be initiated at the interface in the real case. The term "reflection" means the shear-band directions change, since two families (before and after reflection) of shear bands may be initiated simultaneously. This trend causes the formation of multiple shear bands at the interface, so that each shear band will not endure a large amount of shear strains. Thus, enhanced ductility can be achieved in the coated MG during experiments.

Figure 3.3 (a) Half-symmetric Rockwell indention model on the metallic glass used for predicting shear band directions in (b) the bulk metallic glass and (c) titanium film coated bulk metallic glass, with $\mu+\beta=0$ and $\upsilon=0.3$. The blue solid curves indicate predicted s shear band directions and the red dashed curves are principal shear stress directions. The short solid black and dashed green curves are corresponding shear band directions and the principal shear stress directions. For clarity, the material coordinate space beneath the indenter is normalized by the contact half width *a*.

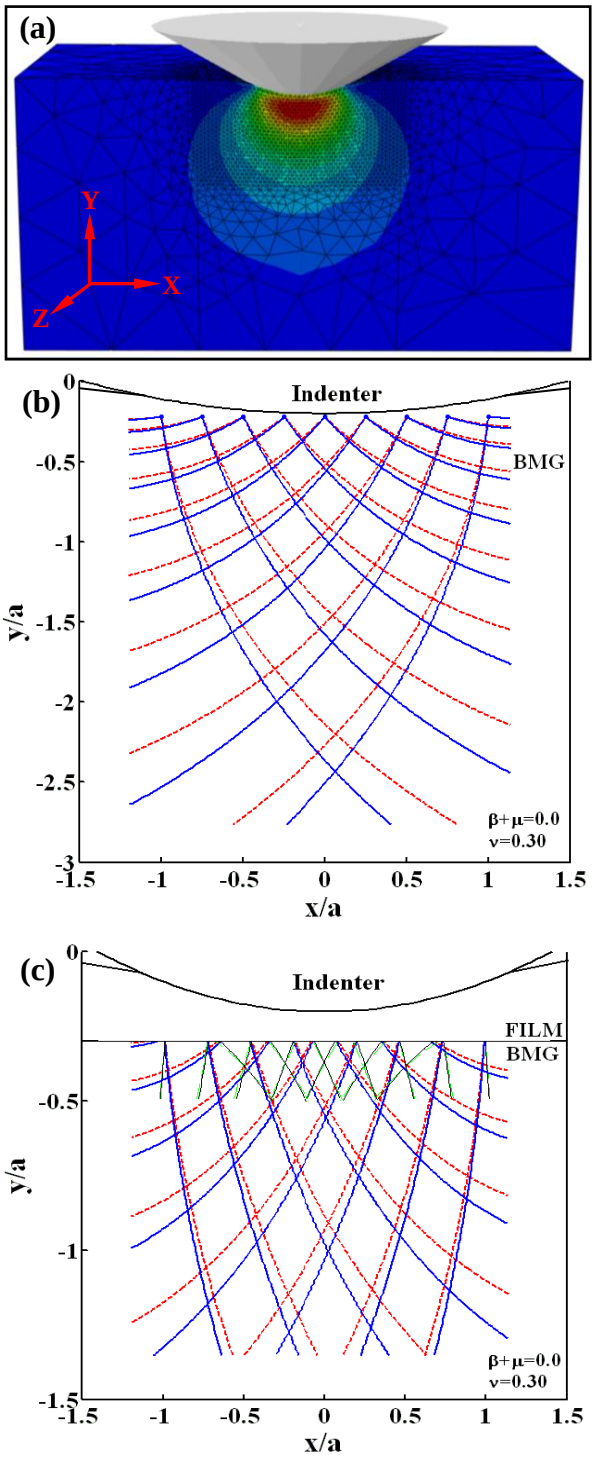
(a)
Y
X
Z
(b)
Indenter
BMG
y/a
x/a
β+μ=0.0
ν=0.30
(c)
Indenter
FILM
BMG
y/a
x/a
β+μ=0.0
ν=0.30

3.2.3. Study with the free volume model

Fatigue behavior of the film-substrate material system is significantly dependent on the adhesion between the film and substrate. However, the effects of the adhesion properties between film and substrate are difficult to be simulated with the Rudnicki-Rice instability theory, although the deformation mechanism, as well as the shear bands propagation direction, in the film-substrate materials is in-depth studied by the indentation simulation using the ABAQUS model and Rudnicki-Rice instability theory in the previous section. Alternatively, a free-volume model will be employed to investigate the film-substrate adhesion on the fatigue behavior of the coating specimens in the following.

A two dimensional (2D) ABAQUS model consisting of four-node plane strain elements, with an element type of C3D4, is built under indentation loading, with the substrate as metallic glass and thin film being a Ti-based alloy. To explore the effects of the coating thickness and adhesion on the enhanced plasticity, films with varied configuration and constitutive laws was employed. A rigid Rockwell indenter was applied to indent specimen, and the sample bottom is completely constrained for any motion. The contact between the indenter and sample was frictionless, while the substrate/coating interaction varies for different simulation purposes, as explained in detail below. For substrate materials in all cases, the constitutive parameters are given as $v_f/\alpha v^* = 0.05$, $E\Omega/2k_BT = 240$, $v = 0.33$, $n_D = 3$, $\alpha = 0.15$, and $v^*/\Omega = 1$. The

normalized loading rate is $\dot{\gamma} = \frac{\dot{h}}{Rf}\exp\left(\frac{\Delta G^m}{k_B T}\right) = 2.3 \times 10^{-6}$ s^{-1}. Different constitutive relations are assigned to coatings and substrate, which will be given below.

To investigate the effects of coating adhesion on the ductility and fatigue enhancement of BMGs, different indentation contours were simulated in Fig. 3.4 [132]. The coating material used in the present work is Ti, which is treated as a purely elastic body in the ABAQUS model, with a Young's modulus of E = 122 GPa and a Poisson ratio of ν = 0.34. In Fig. 3.4(a), it is demonstrated that the indentation of the bare BMG substrate results in several major pairs of intersecting shear bands. By contrast, the indentation of Ti-coated MG specimen to the same displacement induces the formation of multiple shear bands, for both infinite-adhesion and zero-adhesion cases, as displayed in Fig. 3.4(b) and (c), respectively. This shear-band multiplication phenomenon in the coating case is attributed to two mechanisms: (1) shear-band reflection occurs at the film/BMG interface, and (2) abundant minor shear-band branches appear inside the coated specimens. Both mechanisms are triggered by the geometrical constraint of coatings and responsible for the enhanced plasticity in MGs. This result agrees well with the previous predictions by the Rudnick-Rice instability theory on shear-band multiplication in coating/substrate materials [129, 130].

Experimental studies [134] reveal that film/substrate adhesion plays a crucial role in enhancing the ductility of BMGs. To examine this effect, two extreme cases are simulated in the present work with the ABAQUS model: (1) indentation of a Ti-coated MG substrate with perfect adhesion (Fig. 3.4(b)) and (2) the same sample with zero

adhesion (Fig. 3.4(c), which is realized by defining a frictionless film/substrate contact between the film and substrate. Consistent with the experimental observations, poor film/substrate adhesion tends to bring about less shear-band reflection and branching, which is attributed to film delamination occurring easily in the poor adhesion case. As a result, only relatively limited enhanced plasticity is obtained in the poorly-bonded coating material, thus leading to poor fatigue improvement. For the perfect film-adhesion condition, the fatigue-crack initiation stage is significantly elongated, thus prolonging the overall fatigue life of this coating material. However, it should be noted that geometrical constraints by coatings will lose their effect on the ductility and fatigue improvement of substrate materials once the fatigue crack starts to propagate.

Figure 3.4 Free volume contour plots on different indentation configurations. (a) Indentation on the bulk metallic glass, without any coating. (b) Indentation on a thin film coated BMG with a bulk/ film thickness ratio of 20. The substrate and film is completely bonded, corresponding to the perfect adhesion case in practice. (d) Indentation on a same film coated BMG, but with zero adhesion. Practically, the film is simply put above the substrate and their interaction is frictionless. All plots are given in deformed mesh with displacement magnification ratio of 1 in three directions.

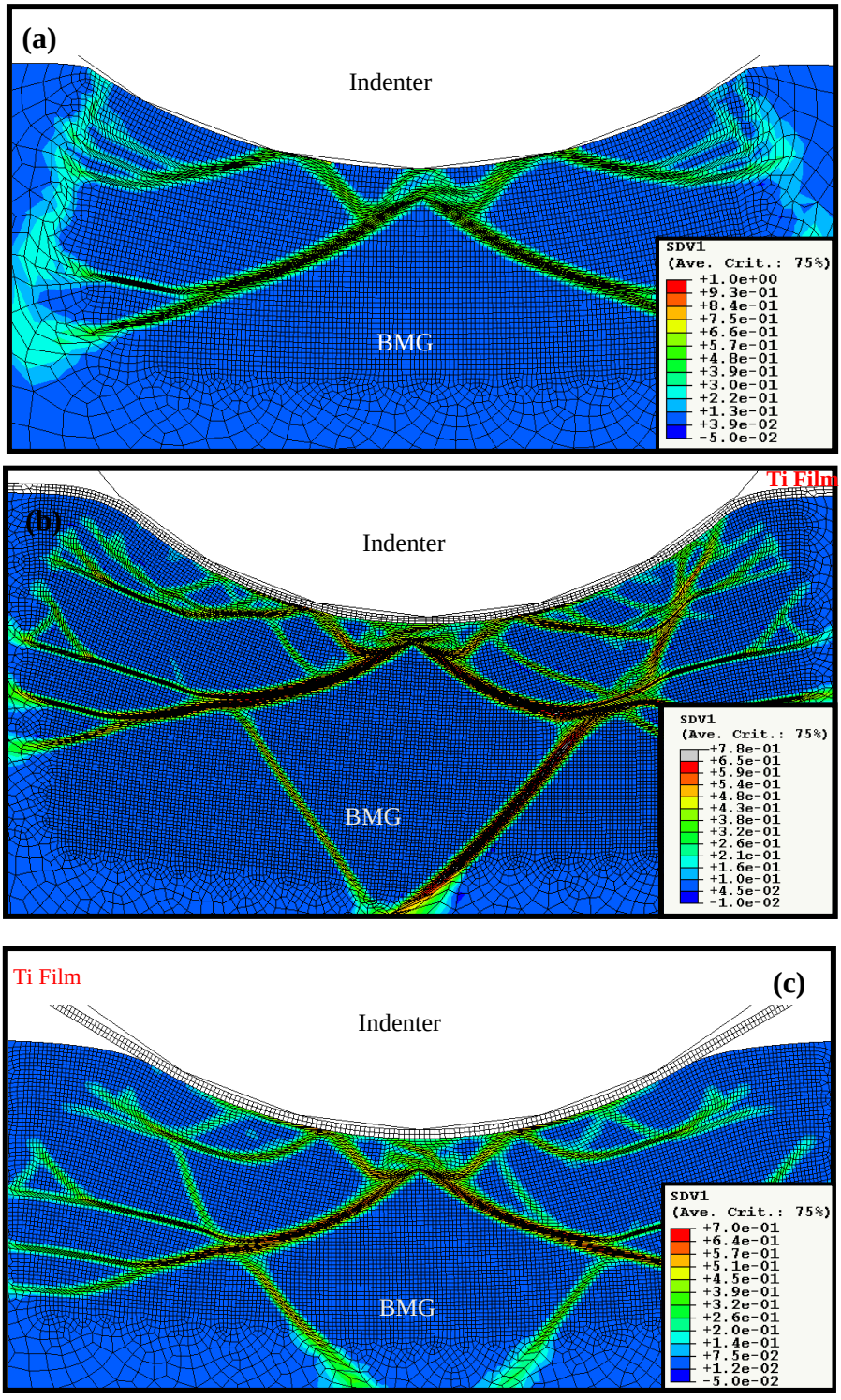
(a)
Indenter
BMG
SDV1
(Ave. Crit.: 75%)
+1.0e+00
+9.3e-01
+8.4e-01
+7.5e-01
+6.6e-01
+5.7e-01
+4.8e-01
+3.9e-01
+3.0e-01
+2.2e-01
+1.3e-01
+3.9e-02
-5.0e-02
(b)
Ti Film
Indenter
BMG
SDV1
(Ave. Crit.: 75%)
+7.8e-01
+6.5e-01
+5.9e-01
+5.4e-01
+4.8e-01
+4.3e-01
+3.8e-01
+3.2e-01
+2.6e-01
+2.1e-01
+1.6e-01
+1.0e-01
+4.5e-02
-1.0e-02
Ti Film
(c)
Indenter
BMG
SDV1
(Ave. Crit.: 75%)
+7.0e-01
+6.4e-01
+5.7e-01
+5.1e-01
+4.5e-01
+3.9e-01
+3.2e-01
+2.6e-01
+2.0e-01
+1.4e-01
+7.5e-02
+1.2e-02
-5.0e-02

Experiments also reveal that fatigue behavior of the thin film coated bulk metallic glass system also strongly depends on the coating thickness [135]. To elucidate what mechanism behind control this and what thickness of the coating should be selected for optimal ductility enhancement, two different cases, with a film/substrate thickness ratio of 20 (thin-film) and 5 (thick-film) are comparatively studied. In both cases, the perfect film/matrix adhesion is adopted. The results reveal that a large amount of shear bands are triggered in the thin-coating case (Fig. 3.5(a)), while less shear bands happen to the thick film coated metallic glasses (Fig. 3.5(b)). This is because in the thick-coating case, the coating itself will have to sustain large deformation. This makes damage or delamination easily happen to the thick film, resulting relatively worse ductility enhancement effect. A clue from the simulation is that in the thick-coating case the deformation in the metallic glass mainly sustained by two major intersecting shear bands, which is more likely to lead to delamination when they arrive at the film/substrate interface, as revealed in Fig. 3.5 (b).

These simulation results are essentially consistent with experimental findings [136] and account for why many fatigue works are conducted on the BMG specimens coated with thin metallic glass films having a thickness of around 200 nm, rather than 1 μm or larger, although some exceptions exist[134, 137, 138].

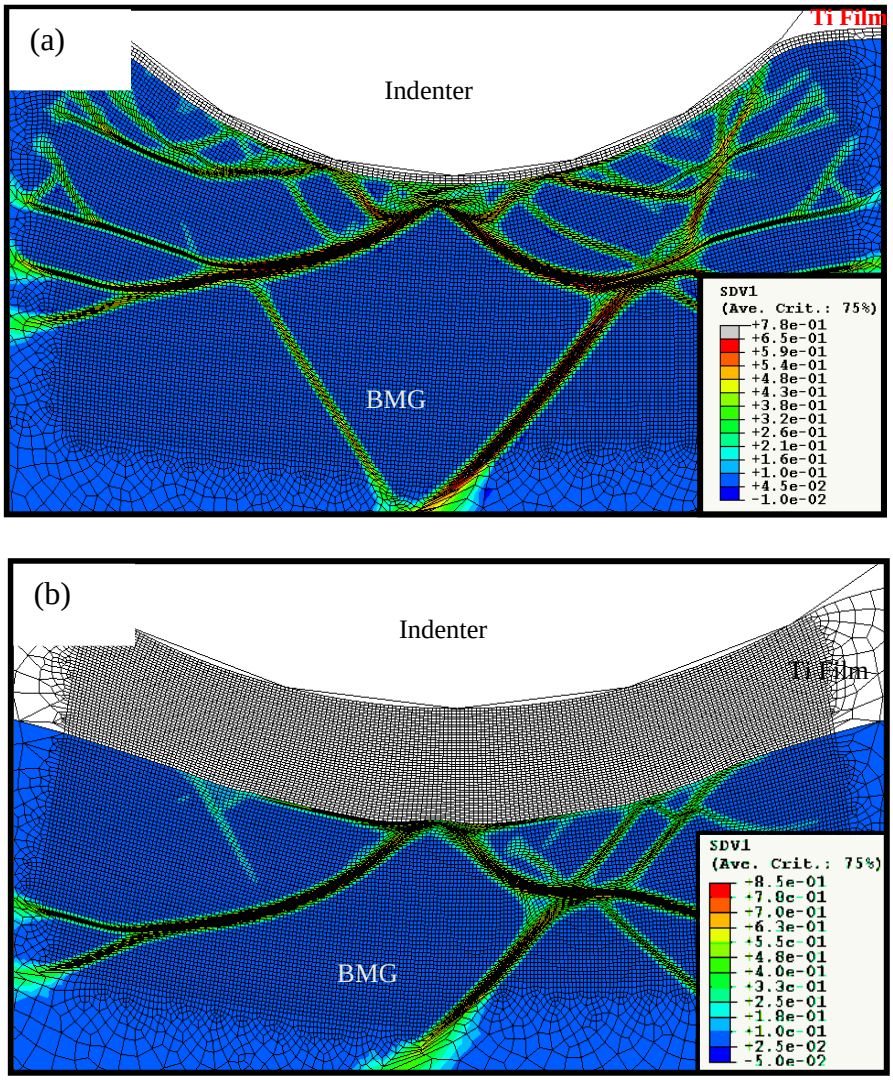

Figure 3.5 An indentation model with free-volume contour plots in different film-thickness cases: (a) a BMG substrate with a thin TFMG, having a film/substrate thickness ratio of 1/20 and (b) a BMG substrate with a thick TFMG, having a film/substrate thickness ratio of 1/5.

3.2.4. Summary

Simulation with the Rudnicki-Rice instability theory and free volume support the experimental observation that coating the bulk metallic glass with Titanium film helps improve the ductility. The radial shear bands pattern under indentation of the bulk metallic glass is successfully predicted with both approaches, while the enhanced ductility attributes to formation of multiple shear bands caused by two mechanisms: shear band reflection at the matrix/film interface and shear band branching inside the material. Goode adhesion between the coating and metallic glass matrix is also critical in guaranteeing effectiveness of the ductility enhancement. Besides, choosing appropriate film thickness is equally important. The intuition that the thicker the coating is, the better the ductility will be is incorrect and a proper coating thickness for different coating/substrate system needs to be selected carefully.

3.3. Deformation mechanisms in the BMG composites[4]

3.3.1. Lattice strain evolution in BMG composites

The bulk metallic glass has very limited plasticity and one way to increase its ductility is to fabricate in-situ BMG composites. A recently developed bulk metallic glass composite has soft crystalline dendrite randomly distributed in the metallic glass matrix,

[4] Study of this part was in collaboration with H.L. Jia at University of Tennessee. H.L. Jia carried out synchrotron diffraction experiments and crystal plasticity simulations to investigate the lattices strain evolution. W.D. Li performed the free volume modeling.

serving as a reinforcement phase, as shown in Fig. 3.6(a) [139-142]. By incorporating the soft dendritic crystals, the ductility of the bulk metallic glass composite can be substantially improved, as indicated by Fig. 3.6(b), which is believed to attribute the arrested propagation of shear bands by soft crystalline phases [143-145]. Since the deformation of the bulk metallic glass composites is accommodated by both the metallic glass matrix and crystalline phase, to build up a clear picture about the deformation mechanism of the metallic glass composite it is necessary to understand how the deformation of the matrix and crystalline phases accommodated with each other. In this sense, deformation of the dendritic inclusions needs to be investigated.

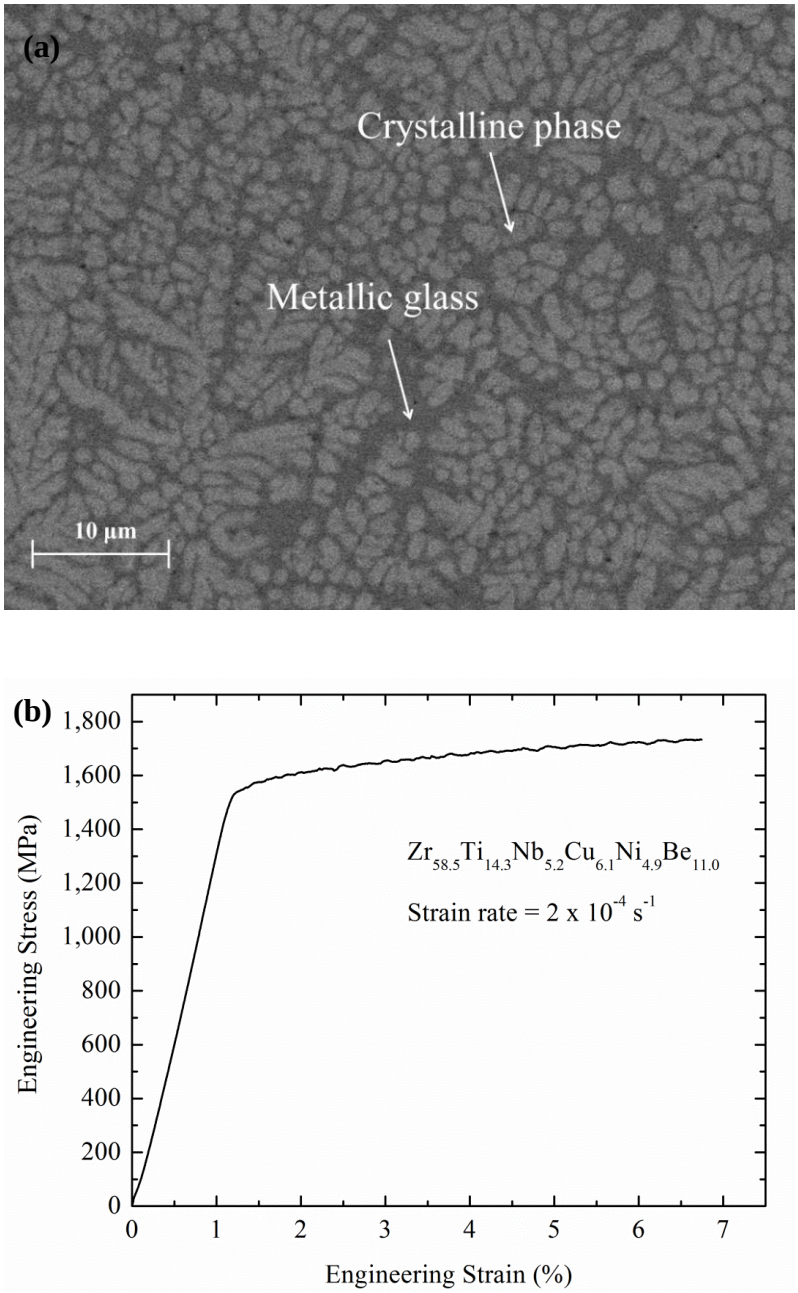

Figure 3.6 (a) Bulk metallic glass composite $Zr_{58.5}Ti_{14.3}Nb_{5.2}Cu_{6.1}Ni_{4.9}Be_{11.0}$, with soft dendritic crystals randomly distributed in the matrix. (b) The compressive stress versus strain, showing apparent plasticity [139].

The high energy X-ray diffraction technique (Synchrotron diffraction) has excellent penetration capability and is able to measure the in-situ deformation of the second phase [146-151]. The deformation of the second crystalline phases is normally characterized by the lattice strain, which indicates the elastic lattice distortion of grains in various crystallographic directions and can be calculated from shift of the diffraction peaks. From the micromechnism point of view, the lattice strain reflects the intergranular interactions between neighboring grains. Experimental measurement by the Synchrotron diffraction found that the lattice strain evolution in the dendritic crystals first experiences elastic deformation followed by nonlinear behavior after yielding and further followed by a strain 'turnover' behavior at high level stress, as depicted in Fig. 3.7 [139]. Meanwhile, simulation with the crystal plasticity model by H.L. Jia through assigning various crystallographic orientations but identical properties based crystal plasticity theory [152, 153] found the similar trend, as in Fig. 3.7. To understand the lattice strain evolution in the crystalline phases in more depth, further modeling studies with the elastic-perfectly-plastic model and free volume model will be performed. Besides, prediction with the free volume model reveal more details in the deformation mechanism in the metallic glass composite because it is capable to capture the shear band feature existing in the metallic glasses.

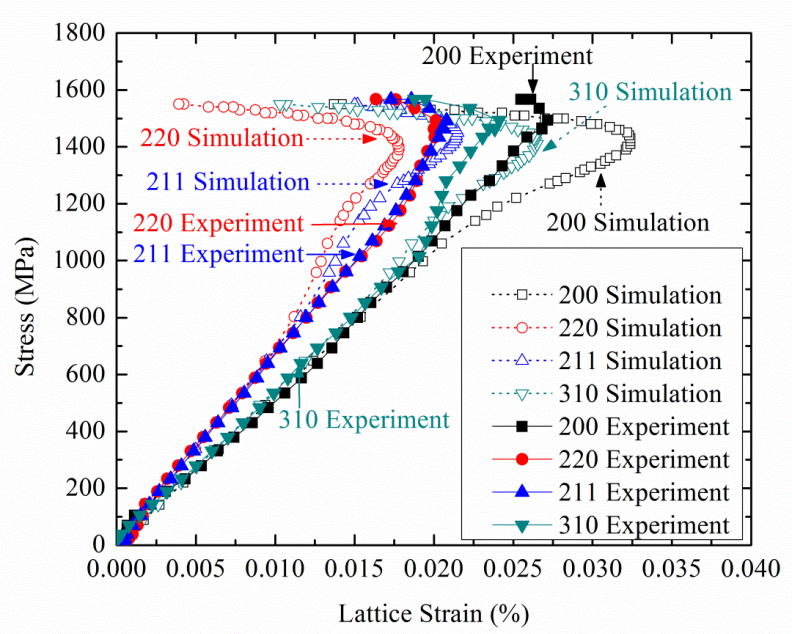

Figure 3.7 Stress versus lattice strain in the crystalline phase of the bulk metallic glass composite studied by both the Synchrotron diffraction measurement and crystal plasticity modeling, showing characteristic 'tunrover' behavior at large stress level [139].

3.3.2. Lattice strain prediction with elastic-plastic model

To reduce the simulation efforts, a two dimensional (2-D) uniaxial compression model is first applied to study the lattice strain evolution of the crystalline phases in the metallic glass composite and only one dentritic inclusion is considered, as shown in Fig. 3.8 (b) and 3.9 (b). Both the matrix and inclusion are simulated as elastic-perfectly-plastic bodies, with Young's modulus, Poisson's ratio and yield stress being 89 GPa, 0.37, 1.4 GPa and 60 GPa, 0.37, 0.45 GPa, respectively. In addition, compression simulations on the bulk metallic glass composites (MGMCs) with 45^{o} and 90^{o} oriented dendrite

inclusions were comparatively studied to investigate the influence of orientations of the dendrite inclusions on the lattice-strain evolution. It is found that in the MGMCs with a 45^{o}-oriented dendrite inclusion, no relaxation occurs, as indicated by (iii) and (iv) in Fig. 3.8(a). In contrast, slight relaxation can be observed in the model with a 90^{o}-oriented dendritic inclusion, as shown in Fig. 3.9(a). In the 45^{o} dendritic model, the stress concentration initiates from four corners of the dendrite inclusion and propagates throughout the entire sample, as shown in the Mises stress contour evolution (i) - (iv) in Fig. 3.8(b). In contrast, stress concentration only starts from two horizontal dendrite vertexes, and the other two perpendicular dendrite vertexes have low stress, as shown in the Mises stress contour evolution (i) - (iv) in Fig. 3.9(b).

Figure 3.8 Compressive stress as a function of the lattice strain for the composite with 90^{o} oriented dendrite inclusion, and corresponding Mises stress evolution contours at representative stages (I)~(IV) are shown in (b). Both the matrix and inclusion are simulated as elastic-perfectly-plastic bodies, with Young's modulus, Poisson's ratio and yield stress being 89 GPa, 0.37, 1.4 GPa and 60 GPa, 0.37, 0.45 GPa, respectively.

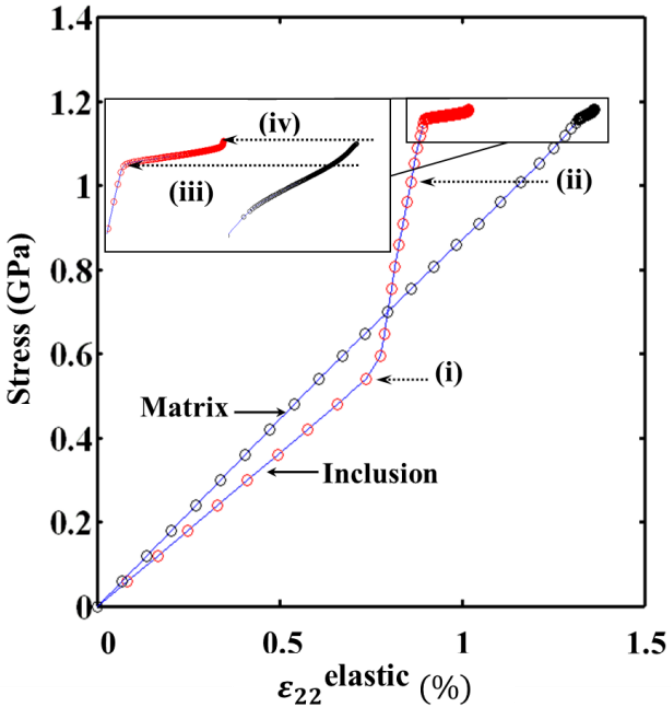
1.4
1.2
1
0.8
0.6
0.4
0.2
0
0
0.5
1
1.5
Stress (GPa)
ε_{22} elastic (%)
(i)
(ii)
(iii)
(iv)
Matrix
Inclusion

(a)

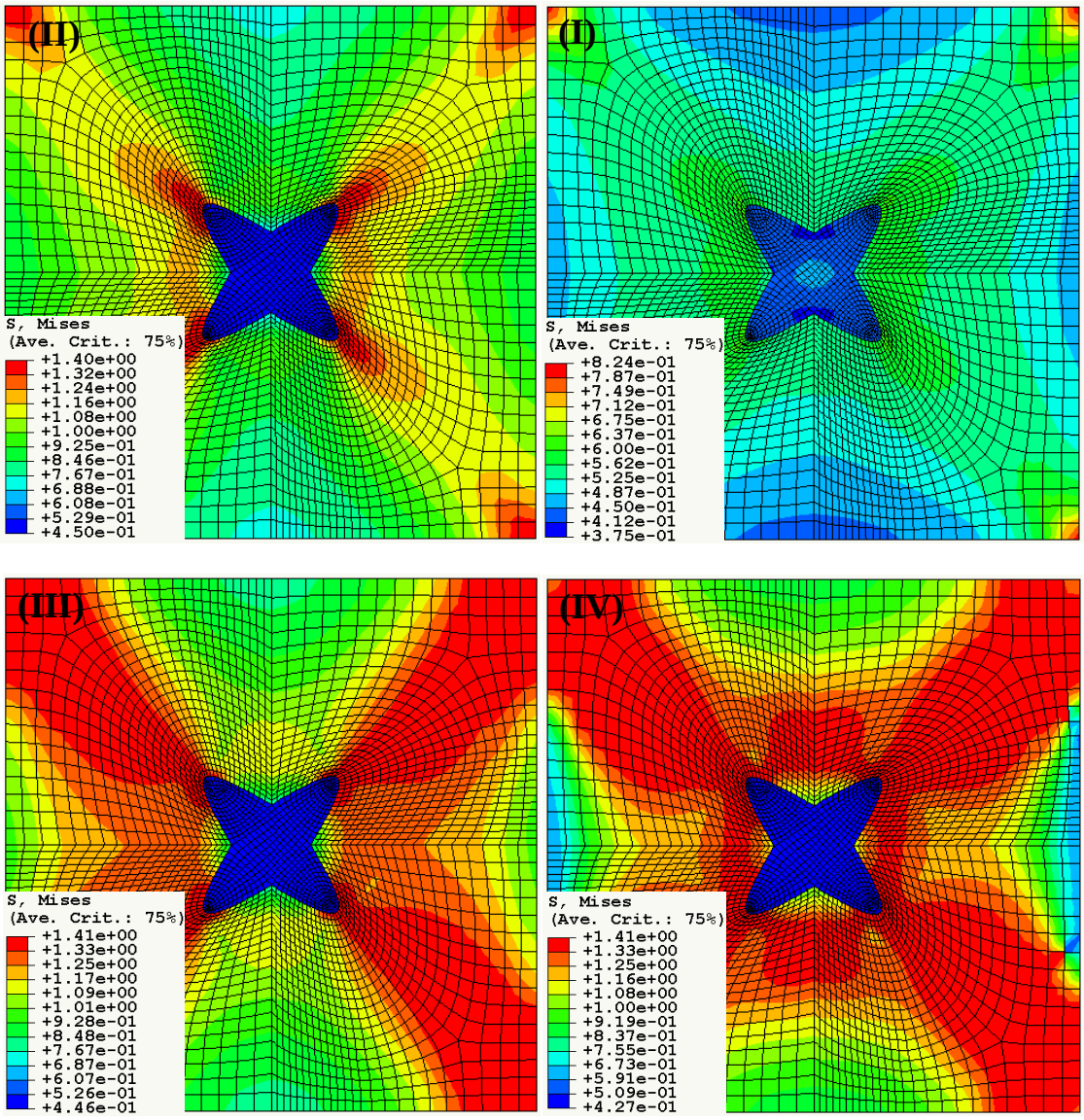
(II)
S, Mises
(Ave. Crit.: 75%)
+1.40e+00
+1.32e+00
+1.24e+00
+1.16e+00
+1.08e+00
+1.00e+00
+9.25e-01
+8.46e-01
+7.67e-01
+6.88e-01
+6.08e-01
+5.29e-01
+4.50e-01
(I)
S, Mises
(Ave. Crit.: 75%)
+8.24e-01
+7.87e-01
+7.49e-01
+7.12e-01
+6.75e-01
+6.37e-01
+6.00e-01
+5.62e-01
+5.25e-01
+4.87e-01
+4.50e-01
+4.12e-01
+3.75e-01
(III)
S, Mises
(Ave. Crit.: 75%)
+1.41e+00
+1.33e+00
+1.25e+00
+1.17e+00
+1.09e+00
+1.01e+00
+9.28e-01
+8.48e-01
+7.67e-01
+6.87e-01
+6.07e-01
+5.26e-01
+4.46e-01
(IV)
S, Mises
(Ave. Crit.: 75%)
+1.41e+00
+1.33e+00
+1.25e+00
+1.16e+00
+1.08e+00
+1.00e+00
+9.19e-01
+8.37e-01
+7.55e-01
+6.73e-01
+5.91e-01
+5.09e-01
+4.27e-01

(b)

Figure 3.9 (a) Compressive stress as a function of the lattice strain for the composite with 45^{o} oriented dendrite inclusion, and corresponding Mises stress evolution contours at representative stages (I)~(IV) are shown in (b). Properties of the matrix and inclusion are the same as the previous.

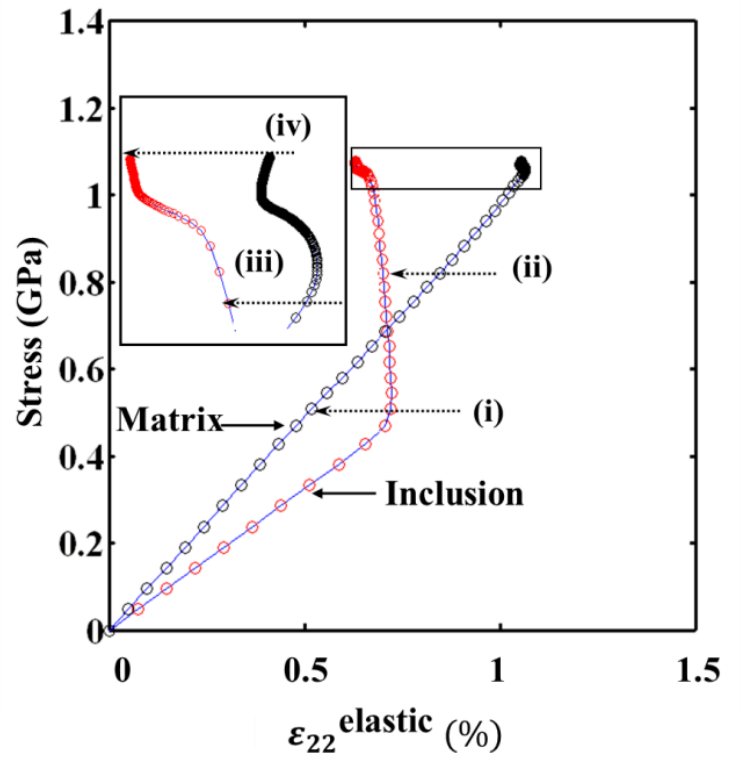
1.4
1.2
1
0.8
0.6
0.4
0.2
0
Stress (GPa)
0
0.5
1
1.5
$\varepsilon_{22}^{elastic}$ (%)
(iv)
(iii)
(ii)
(i)
Matrix
Inclusion

(a)

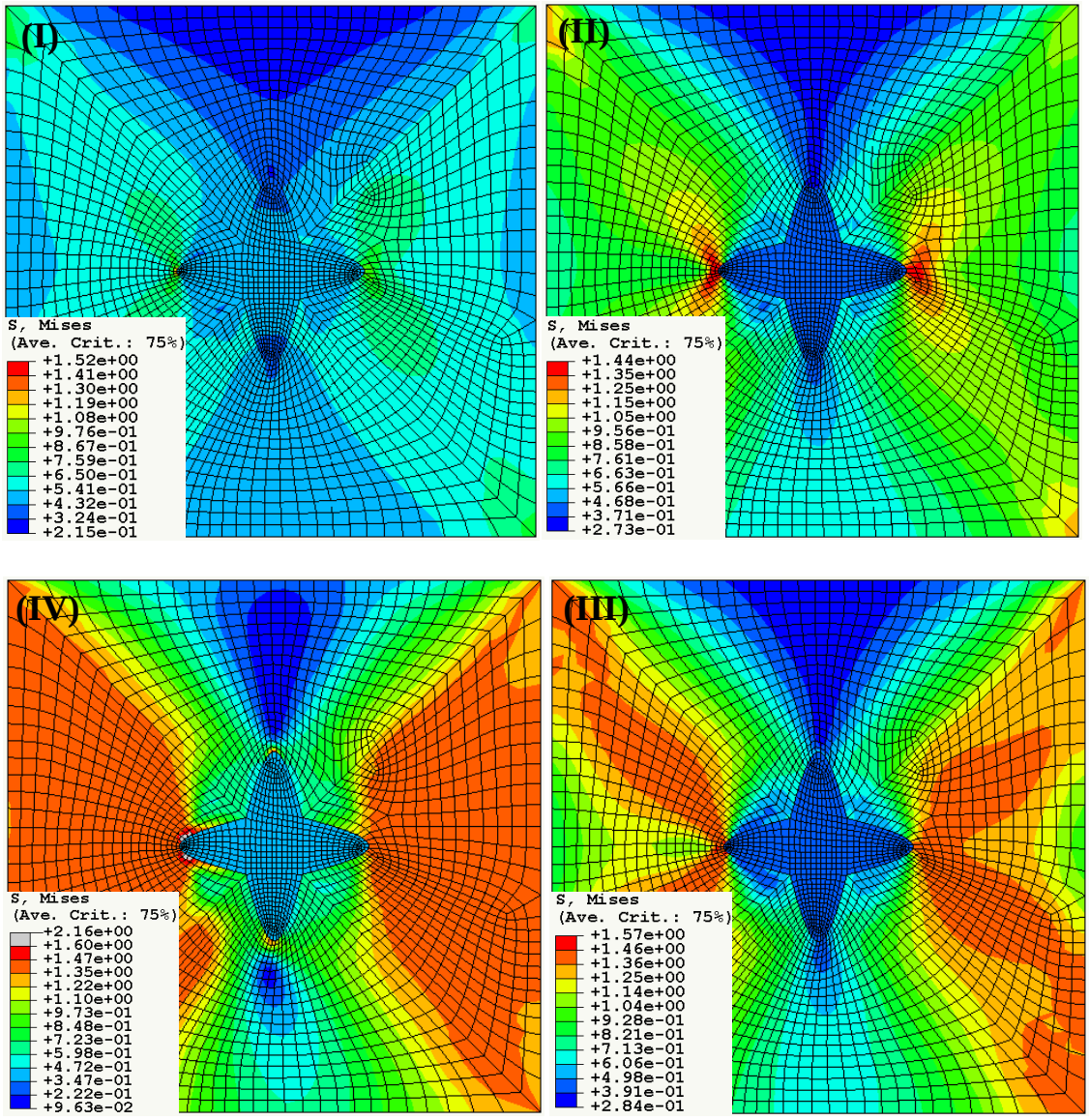
(I)
S, Mises
(Ave. Crit.: 75%)
+1.52e+00
+1.41e+00
+1.30e+00
+1.19e+00
+1.08e+00
+9.76e-01
+8.67e-01
+7.59e-01
+6.50e-01
+5.41e-01
+4.32e-01
+3.24e-01
+2.15e-01
(II)
S, Mises
(Ave. Crit.: 75%)
+1.44e+00
+1.35e+00
+1.25e+00
+1.15e+00
+1.05e+00
+9.56e-01
+8.58e-01
+7.61e-01
+6.63e-01
+5.66e-01
+4.68e-01
+3.71e-01
+2.73e-01
(IV)
S, Mises
(Ave. Crit.: 75%)
+2.16e+00
+1.60e+00
+1.47e+00
+1.35e+00
+1.22e+00
+1.10e+00
+9.73e-01
+8.48e-01
+7.23e-01
+5.98e-01
+4.72e-01
+3.47e-01
+2.22e-01
+9.63e-02
(III)
S, Mises
(Ave. Crit.: 75%)
+1.57e+00
+1.46e+00
+1.36e+00
+1.25e+00
+1.14e+00
+1.04e+00
+9.28e-01
+8.21e-01
+7.13e-01
+6.06e-01
+4.98e-01
+3.91e-01
+2.84e-01

(b)

Therefore, this inclusion geometry study can provide some guidance on the design and preparation of MGMCs. The 90^{o}-oriented dendritic inclusions should have a better preference on the strength and ductility of MGMCs, compared to the 45^{o}-oriented dendritic inclusions, since the 45^{o} dendritic case can bring more severe stress concentration into MGMCs upon loading.

3.3.3. Shear band evolution and deformation mechanism

The previous studies successfully predict the lattice strain evolution of crystalline phases in MGMCs, the micro-mechanism responsible for the localized deformation in shear bands in MG matrix, however, remains unclear. To understand this, the free-volume-based constitutive model for MG matrix is used to investigate the shear bands initiation and propagation in MGMC upon uniaxial compression. The material parameters for MG matrix are $v_f/\alpha v^* = 0.05$, $E\Omega/2k_BT = 200$, ν=0.37, $n_D = 3$, α=0.15, and v^*/Ω=1, and applied strain rate is 1.0×10^{-3} s^{-1}. The crystalline inclusions are elastic-perfectly plastic body, with Young's modulus, Poisson's ratio, and yield stress being 60 GPa, 0.37 and 0.45 GPa, respectively. For comparison, two types of MGMCs with different inclusion shapes, dendritic and circular, are employed for calculations.

Fig. 3.10(a) shows the lattice strain evolution for both MG matrix and crystalline inclusion in the circular inclusion model under compressive loading. Here, the lattice strain is in fact the elastic strain in loading direction and applied stress is the one on the entire specimen. The ultimate lattice strain in the crystalline inclusion is obtained by averaging the values of all inclusion grains. As observed in Fig. 3.10(a), with increasing

applied stress, the lattice strain in both matrix and inclusion rises linearly at the beginning till a deviation occurs at a stress of ~ 0.8 GPa. Afterwards, the lattice strain of MG matrix still increase linearly, while that of inclusions turns to evolve at a much lower rate with the applied stress elevating, implied by the consistent and reduced stress/lattice-strain slope of the matrix and inclusion, respectively. This is due to the load partitioning following the yielding of crystalline inclusion. When the applied stress reaches ~ 1.7 GPa, the difference of stress/lattice-strain slope between MG matrix and inclusion becomes more significant. With the further increase of the applied stress, the lattice strain of the matrix increases significantly, while that of the inclusions begins to decrease, namely, a 'turnover' phenomenon. To obtain insights on the micro-mechanism responsible for the stress/lattice-strain slope change in the matrix and inclusion, particularly on the 'turnover' behavior, the free volume evolution at four representative stages (i) - (iv) are plotted in Fig. 3.10(b), corresponding to the four positions in the stress - lattice strain curves in Fig. 3.10(a). At stage (i), although inclusions have already yielded at a nominal yield stress of 0.45 GPa and the free volume in matrix starts to localize around the matrix/second phase interface, no stress/lattice-strain slope change occurs. This indicates that the load partitioning in the MGMC does not happen immediately following the yielding of inclusions. When the load is increased to 1.2 or 1.7 GPa, localized deformation begins to form in shear bands, typically as demonstrated in stage (ii) and (iii). At these two stages, more loads will be transferred to matrix, resulting in much increased lattice strain, while the lattice strain in crystalline inclusion tends to evolve slowly. The

shear bands can be observed to initiate at an angle of ~ 45 ^{o} from the matrix/inclusion interface and propagate outward. Ultimately, when the localized shear bands propagate and link with each other, the lattice strain relaxation in the inclusions become more significant and the 'turnover' behavior will emerge, as depicted in (iv) in Fig. 3.10(b).

Moreover, the simulation with the free volume model is helpful in understanding the mechanism responsible for the enhanced macroscopic plasticity in MGMCs. In a monolithic BMG, a major shear band will cut through the entire sample once it initiates from some weak locations, since no blocking mechanism exists. In contrast, the shear band propagation in MGMCs could be blocked or deflected by the second phases. As revealed by Fig. 3.10(b), the shear bands do not propagate catastrophically after they initiate from the matrix/inclusion interface. Instead, the propagation of shear bands is refined to a local area enclosed by neighboring shear bands. This second-phase blocking mechanism contributes to the improved plasticity of MGMCs by avoiding the formation of a major shear band. Till a dominant shear band is formed through the linkage of many minor shear bands at large applied loads, a potential rupture path can be formed leading to the fracture of MGMCs, as demonstrated in stage (iv) in Fig. 3.10(b).

Study on the dendritic-inclusion embedded MGMCs with free volume model is shown in Fig. 3.10(a) and (b), which exhibit similar trends with the circular-inclusion model. The only difference is that the shear bands preferentially initiate from vertexes of the dendritic inclusions, as observed in Fig. 3.10(b). This demonstrates that geometry of

the inclusions does not exert significant influence on the lattice strain evolution and micro-mechanism responsible for this.

Figure 3.10 (a) Applied stress as a function of the $\varepsilon_{22}^{elastic}$ for both inclusion and matrix in the composite with multiple circular inclusions, and (b) the corresponding Mises stress evolution contours at representative stress levels (i) - (iv). The matrix is described by the free volume constitutive model through a UMAT subroutine in ABAQUS, with Young's modulus and Poisson's ratio being 200 GPa and 0.37, respectively. Other parameters can be found in text. The inclusion phase is elastic-perfectly plastic solid with Young's modulus, Poisson's ratio, and yield stress being 60 GPa, 0.37, and 0.45 GPa, respectively. All figures are given in deformed mesh with a displacement magnification ratio of 1 and the state dependent variable 1 (SDV1) specifies the free volume.

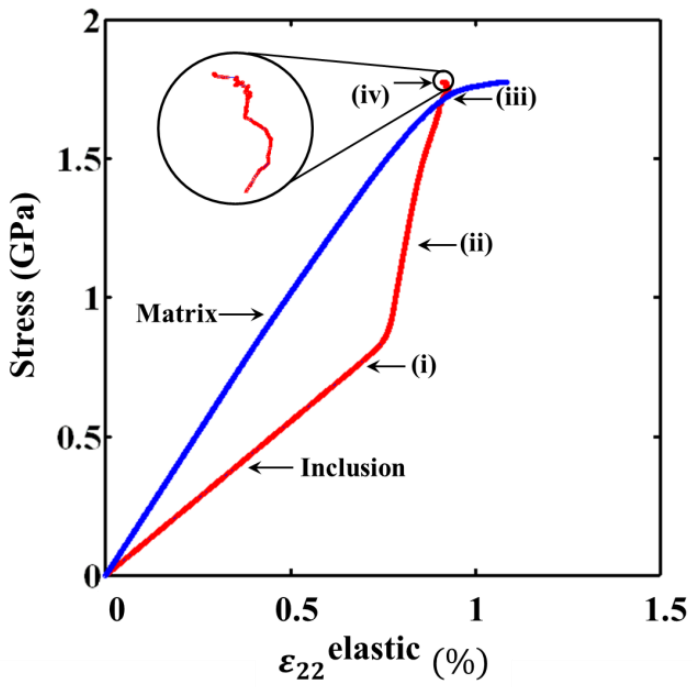
2
1.5
1
0.5
0
0
0.5
1
1.5
Stress (GPa)
ε_{22} elastic (%)
(iv)
(iii)
(ii)
(i)
Matrix
Inclusion

(a)

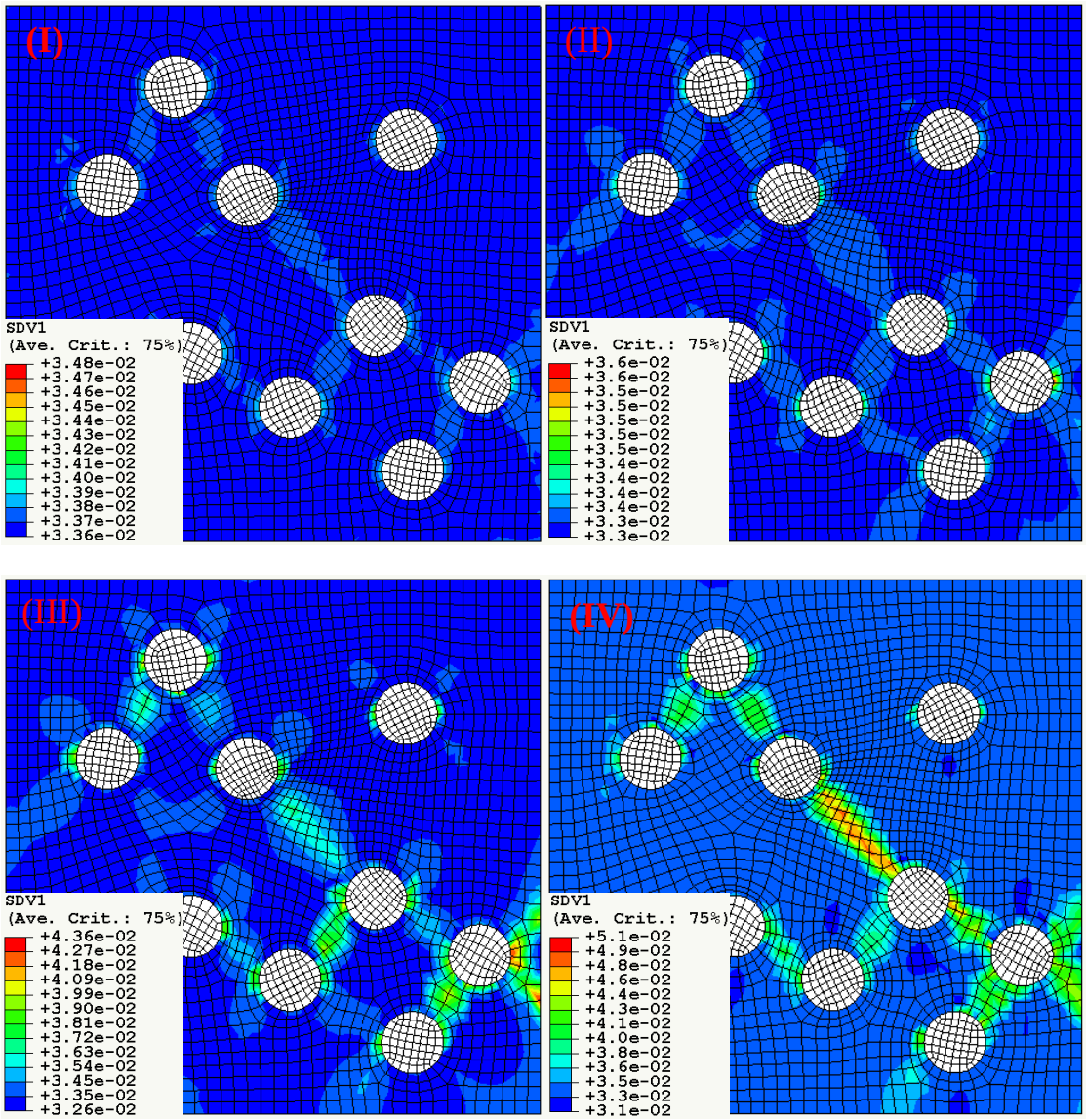
(I)
SDV1
(Ave. Crit.: 75%)
+3.48e-02
+3.47e-02
+3.46e-02
+3.45e-02
+3.44e-02
+3.43e-02
+3.42e-02
+3.41e-02
+3.40e-02
+3.39e-02
+3.38e-02
+3.37e-02
+3.36e-02
(II)
SDV1
(Ave. Crit.: 75%)
+3.6e-02
+3.6e-02
+3.5e-02
+3.5e-02
+3.5e-02
+3.5e-02
+3.5e-02
+3.4e-02
+3.4e-02
+3.4e-02
+3.4e-02
+3.3e-02
+3.3e-02
(III)
SDV1
(Ave. Crit.: 75%)
+4.36e-02
+4.27e-02
+4.18e-02
+4.09e-02
+3.99e-02
+3.90e-02
+3.81e-02
+3.72e-02
+3.63e-02
+3.54e-02
+3.45e-02
+3.35e-02
+3.26e-02
(IV)
SDV1
(Ave. Crit.: 75%)
+5.1e-02
+4.9e-02
+4.8e-02
+4.6e-02
+4.4e-02
+4.3e-02
+4.1e-02
+4.0e-02
+3.8e-02
+3.6e-02
+3.5e-02
+3.3e-02
+3.1e-02

(b)

Figure 3.11 (a) Applied stress as a function of the $\varepsilon_{22}^{elastic}$ for both inclusion and matrix in the composite with multiple dendrite inclusions, and (b) the corresponding Mises stress evolution contours at representative stress levels (i) - (iv). All the parameters are the same as those in Fig. 3.10.

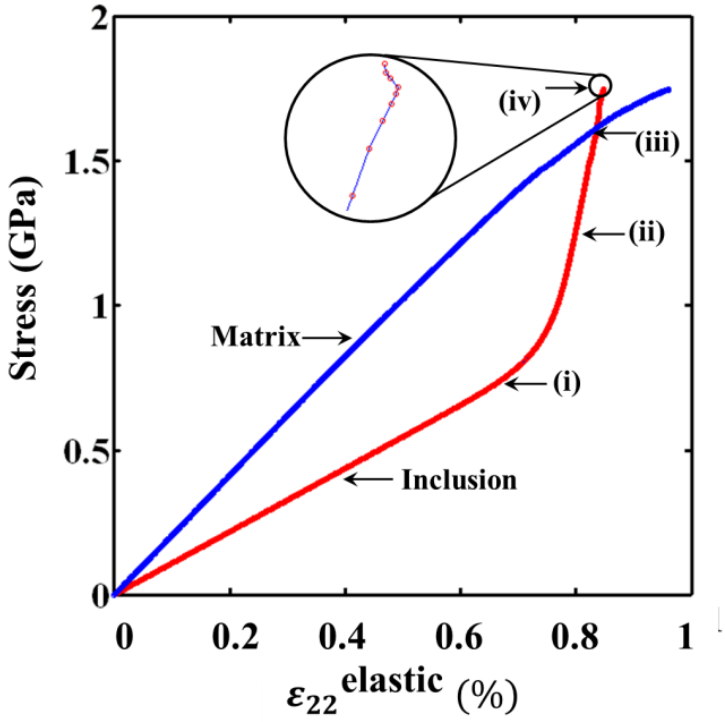
Stress (GPa)
2
1.5
1
0.5
0
0
0.2
0.4
0.6
0.8
1
ε_{22} elastic (%)
(iv)
(iii)
(ii)
(i)
Matrix
Inclusion

(a)

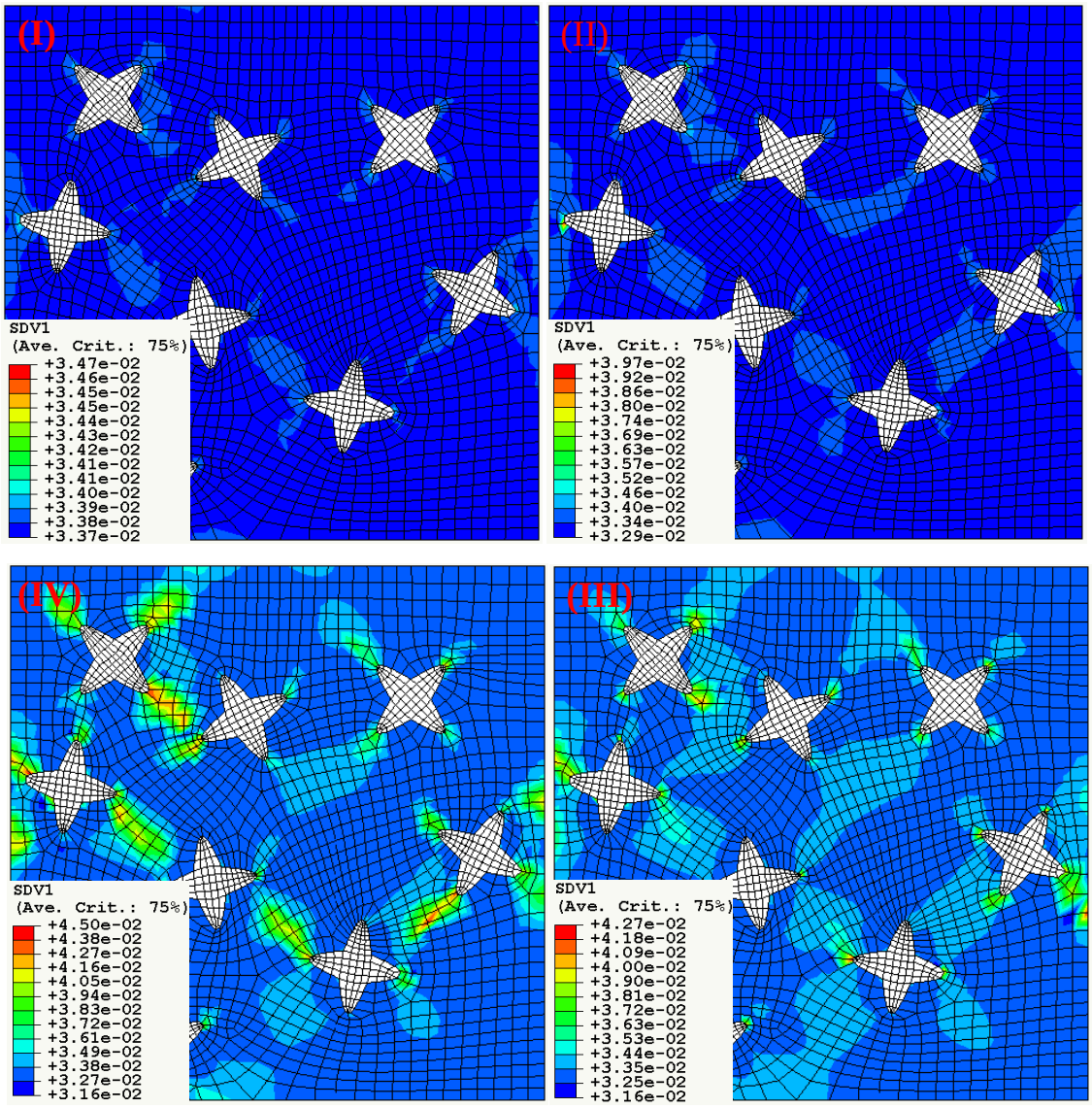
(I)
SDV1
(Ave. Crit.: 75%)
+3.47e-02
+3.46e-02
+3.45e-02
+3.45e-02
+3.44e-02
+3.43e-02
+3.42e-02
+3.41e-02
+3.41e-02
+3.40e-02
+3.39e-02
+3.38e-02
+3.37e-02
(II)
SDV1
(Ave. Crit.: 75%)
+3.97e-02
+3.92e-02
+3.86e-02
+3.80e-02
+3.74e-02
+3.69e-02
+3.63e-02
+3.57e-02
+3.52e-02
+3.46e-02
+3.40e-02
+3.34e-02
+3.29e-02
(IV)
SDV1
(Ave. Crit.: 75%)
+4.50e-02
+4.38e-02
+4.27e-02
+4.16e-02
+4.05e-02
+3.94e-02
+3.83e-02
+3.72e-02
+3.61e-02
+3.49e-02
+3.38e-02
+3.27e-02
+3.16e-02
(III)
SDV1
(Ave. Crit.: 75%)
+4.27e-02
+4.18e-02
+4.09e-02
+4.00e-02
+3.90e-02
+3.81e-02
+3.72e-02
+3.63e-02
+3.53e-02
+3.44e-02
+3.35e-02
+3.25e-02
+3.16e-02

(b)

Note that in the present model MGMCs contain roughly 20% (volume percent) of crystalline inclusions, however, in the real specimens, the volume percentage of crystals is ~50%. The only difference between the high-volume and low-volume percentage cases is that the chance of forming a dominant shear band by connecting many minor ones is much smaller for the high-volume percentage case, due to the enhanced blocking effect of second phase. Clearly, the success of the MGMCs in ductility enhancement needs to reach this percolation limit.

3.3.4. Summary

The lattice strain evolution in the crystalline phases reinforced bulk metallic glass matrix shows a 'turnover' behavior at a high level of stress. Simulation supports that this attributes to the load partitioning followed yielding of the metallic glass matrix. Modeling with simple elastic-plastic model also finds that the lattice strain relaxation also relies on the orientation of the dendrite crystalline inclusion. The improved ductility in the bulk metallic glass composites attributes to existence of the shear band blocking mechanism via presence of the second phases. The shear bands are found initiate from the second phase/matrix interface and propagate at an angle of around 45^{o}. The sample will not fracture till a major shear band is formed by connecting many small propagating shear bands.

CHAPTER 4

Effects of machine stiffness on the loading-displacement curve during spherical nano-indentation

4.1. Introduction

The instrumented indentation technique (or nanoindentation) has become a ubiquitous tool for the characterization of mechanical properties of materials at micro- and nano-scales. It can provide resolution of the load and penetration of depth down to micro-Newtons and nanometers [154, 155]. Early applications lead to direct mechanical characterization of thin film systems and materials under confined conditions, and current applications can be found across multiple disciplines [156-159]. In a typical indentation test, by precisely controlling the movement of indenters, the depth of penetration and the applied load are simultaneously recorded as an experimental load-displacement curve (frequently termed *P*-*h* curve), from which many mechanical properties of test specimens can be extracted. The most common use is for the measurement of hardness and stiffness [154, 155]. In addition, other elastic or plastic mechanical properties, such as hardening exponents [157, 160], fracture behavior [161, 162], creep deformation [163-165], and residual stresses [166-168], can also be evaluated.

Spherical indentation tests have several advantages over sharp indentations (i.e., conical and pyramidal indenters), and thus have been used extensively for probing various mechanical properties of a wide variety of materials recently [167, 169, 170]. Unlike

the self-similar deformation fields in sharp indenters, the plastic deformation field under spherical indentations changes gradually. For spherical indentations, the *P-h* curves have both the initial elastic response and the subsequent elasto-plastic behavior, while sharp indentation responses will be elasto-plastic immediately from the beginning. This enables spherical instrumented indentation to investigate many material properties that cannot be obtained by sharp indentation. For example, by solely using a single spherical indentation test, plastic properties of materials can be determined [170-173]. In contrast, for sharp indentations, either the stress-strain relation cannot be uniquely determined or multiple-indenter tests are needed [156, 174, 175]. For another example, the evident elastic-plastic transition in spherical indentations makes it ideal in investigating elastic behavior and incipient plasticity at small scales, marked by pop-ins on the *P-h* curve in both crystalline materials [176-179] and amorphous metals [159, 180, 181]. Also, spherical indentations can be used to study the size effects in that hardness changes with respect to indenter tip radii [182] as well as a newly discovered different type of size effect in which the pop-in stresses increase with decreasing indenter tip radii [178, 183]. All these applications with spherical instrumented indentation, however, rely upon a knowledge of the correct indenter tip radius. If the incorrect indenter tip radii were used, all subsequent calculations would become erroneous.

In practice, the uncertainty of the nominally measured tip radii offered by providers, which originates from difficulties in measurements at small scales, leads to researchers avoiding using these values directly. A routinely adopted method, which is

believed to be able to give correct R values, is to use the Hertzian elastic fitting [155, 184], in which the load P should be proportional to $R^{1/2}h^{3/2}$ with h being the depth of penetration if the load-displacement curve is entirely elastic. Clearly the correctness of the indenter tip radius obtained this way relies on accurate measurement of both the load and displacement. Experimentally, the displacement measured by the displacement gauge (as shown in Fig. 4.1(a)) actually consists of two parts: the penetration into the sample, h_{sample}, and the deflection of the loading frame, $h_{machine}$, so that $h_{total}=h_{sample}+h_{machine}$. The loading frame may be modeled as a spring with $h_{machine} = P/S_{machine}$, where $S_{machine}$ is the machine stiffness, as schematically shown in Fig. 4.1(b). The Hertzian theory merely considers the relation between the depth of penetration and load. In other words, when the load frame deflection is large enough, e.g., approaching the same order of magnitude as the depth of penetration, the Hertzian theory would become invalid on the experimental P-h curve if treating the displacement reading as solely from the contact response. As a result, the indenter tip radii determined using the direct Hertzian fitting become incorrect. This occurs particularly at high loads or indenting on stiff materials. It should also be noted that the machine stiffness may vary as a function of the applied load.

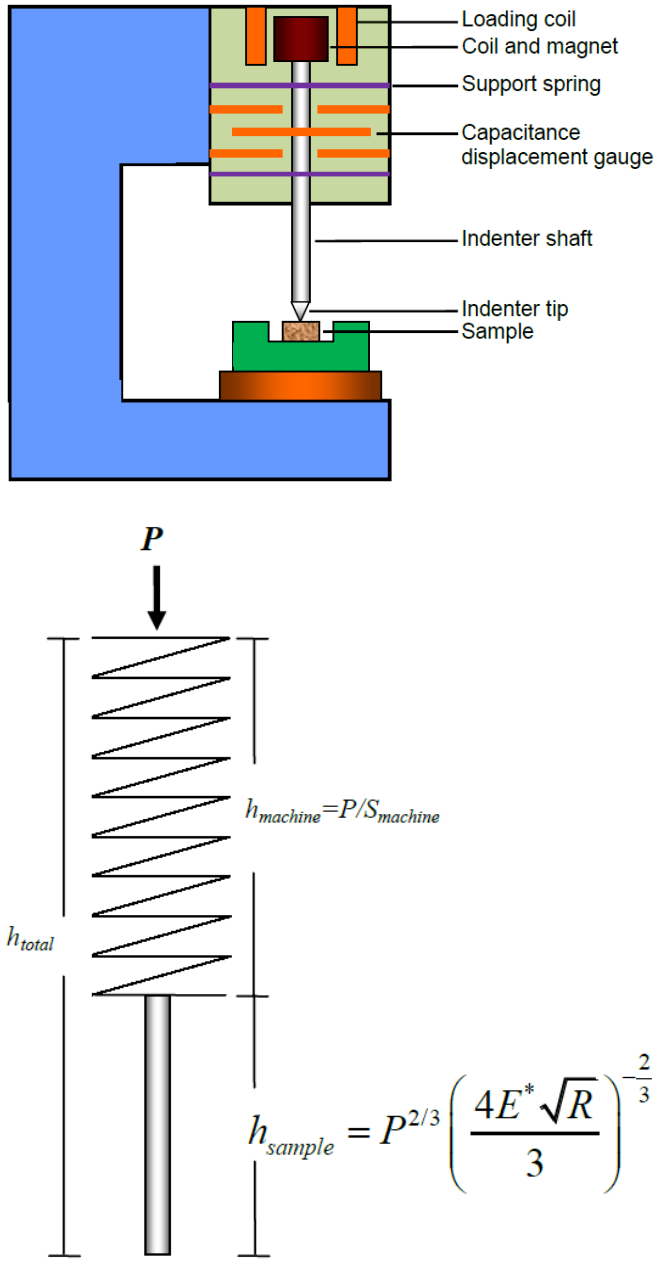

Figure 4.1 (a) Schematic illustration of the instrumented indentation system (reproduced after Oliver and Pharr, 1992) and (b) schematic diagram showing that the experimentally measured displacement is the sum of the loading frame deflection, $h_{machine}$, and the penetration into the sample, h_{sample}, i.e., $h_{total}=h_{sample}+h_{machine}$.

The purpose of the present work is to develop a method that is capable of determining the correct indenter tip radius under any conditions, and simultaneously evaluating the machine stiffness quantitatively. This is achieved by simply incorporating the machine stiffness into the Hertzian theory and testing two materials with known material stiffness. The tip radius values obtained from our approach are compared with those from the routinely used method (i.e., direct Hertzian fitting), and differences are carefully examined. The machine stiffness is systematically analyzed for various indenters and loads, which provides insights in identifying when the direct Hertzian fitting is suitable for deriving indenter tip radii and when is not.

4.2. Method

The classic Hertzian contact solution is applicable for elastic half-spaces indented by indenters described by parabolae of revolution, or for elastic bodies with initial separation gaps described by parabolae of revolution [185, 186]. The indentation load, *P*, is related to the indentation depth, $h_{elastic}$, (or more rigorously, the approaching of faraway reference points on the two elastic solids in contact) by

$$P = \frac{4}{3} E^* \sqrt{R} h_{elastic}^{3/2}, \tag{4-1}$$

where *R* is the indenter radius and the reduced modulus E^* is given by

$$\frac{1}{E^*} = \frac{1-\upsilon_s^2}{E_s} + \frac{1-\upsilon_i^2}{E_i}, \tag{4-2}$$

for isotropic elastic materials with E and υ being the Young's modulus and Poisson's ratio, respectively. The subscripts s and i denote the sample and indenter, respectively. For anisotropic elastic materials, Eq. (4-1) holds true but the representation in Eq. (4-2) is significantly complicated. The indentation modulus plays a critical role in procedures that determine material hardness such as the Oliver-Pharr approach [154, 155].

This paper is built upon the notion that the displacement data as obtained from the instrumented indentation technique has the contributions from the contact response as in Eq. (4-1), the deflection of the loading apparatus due to the finite machine stiffness ($S_{machine}=P/h_{machine}$), and the uncertainty in identifying the onset of contact, as shown in Fig. 4.1 (b). Since a constant machine stiffness, $S_{default}$, is predefined in the data processing software prior to testing, the reported displacement reading differs from that measured by the displacement gauge by

$$h_{reported} = h_{total} - \frac{P}{S_{default}}, \tag{4-3}$$

where h_{total} is the total displacement measured from the gauge in Fig. 4.1(a), and $h_{reported}$ is the reported displacement reading from the data processing software. If solely considering the displacement measured by the gauge, we have

$$h_{total} = \frac{P}{S_{machine}} + P^{2/3}\left(\frac{4}{3}E^{*}\sqrt{R}\right)^{-2/3} + h_0, \tag{4-4}$$

in which the first term on the right hand side is the deflection of the loading frame and the second term is due to the contact response, as schematically shown in Fig. 4.1(b). $S_{machine}$ is the overall machine stiffness to be determined, which in principle is a complicated

function of the load, *P*. A constant h_0 is introduced to account for the uncertainty of onset of contact. Combining Eqs. (4-3) and (4-4) gives

$$h_{reported} = \frac{P}{S_{machine}} - \frac{P}{S_{default}} + P^{2/3}(\frac{4}{3}E^*\sqrt{R})^{-2/3} + h_0 \,. \tag{4-5}$$

Our method to determine *R* and $S_{machine}$ is based on indentation tests on two different materials with known moduli. Thus, taking the difference of the following two equations,

$$h_{reported,I} = \frac{P}{S_{machine}} - \frac{P}{S_{default}} + P^{2/3}(\frac{4}{3}E_I^*\sqrt{R})^{-2/3} + h_{0,I} \,, \tag{4-6}$$

$$h_{reported,II} = \frac{P}{S_{machine}} - \frac{P}{S_{default}} + P^{2/3}(\frac{4}{3}E_{II}^*\sqrt{R})^{-2/3} + h_{0,II} \,, \tag{4-7}$$

we get

$$h_{reported,I} - h_{reported,II} = P^{2/3}(\frac{4}{3}\sqrt{R})^{-2/3}(E_I^{*-2/3} - E_{II}^{*-2/3}) + (h_{0,I} - h_{0,II}) \,. \tag{4-8}$$

Provided with E^* of these two materials, we can find the indenter radius by a linear fitting between $h_{reported,I}$-$h_{reported,II}$ and $P^{2/3}$. It is obvious that the success of this method relies on the assumption that the machine stiffness is only a function of the applied load, and the subtraction between the two sets of *P*-*h* curves should be conducted at the same load. Subsequently, with a known indenter radius, we can plot $h_{reported} - P^{2/3}(\frac{4}{3}E^*\sqrt{R})^{-2/3} + P/S_{default}$ against *P*, which will lead us to determine $S_{machine}$ and h_0 as in Eq. (4-5).

4.3. Experimental

Instrumented indentation tests were carried out on a MTS XP Nanoindenter (MTS Nano Instruments, Oak Ridge, TN) using diamond spherical indenters (E=1141 GPa, ν=0.07) with nominal tip radii of 2.55, 5.0, 8.3, 9.0, 50.0 and 100.0 μm and sapphire spherical indenters (E=433 GPa, ν=0.2) with nominal tip radius of 100.0 and 250.0 μm, respectively. The nominal indenter tip radii were provided by the manufacturer. During all tests, a machine stiffness of 9.1 N/μm was pre-selected in the current nanoindenter, according to manufacturer suggestion for routine hardness and modulus measurement using a Berkvoich diamond indenter. Fused silica (E=73 GPa, ν=0.17) and sapphire (E=433 GPa, ν=0.2) were selected for indentation tests because of their substantially different indentation moduli. This enables us to obtain two sets of P-h data having radically distinctive penetration depth at the same load, and consequently the calculation will be more reliable in Eq. (4-8). Moreover, the reduced modulus to hardness ratio E_r/H for those two materials is small, having E_r^{sp}/H^{sp} =13.9 and E_r^{fs}/H^{fs} =6.14 for the sapphire and fused silica, respectively. All tests were limited to the elastic region by using the continuous stiffness mode with a constant rate of $\dot{P}/P$ =0.05 s^{-1} and the displacement oscillation is 1 nm. We select those experiment conditions to reduce the possibility of the loss contact problem [187, 188]. On a given specimen, about 9 indents were made by each indenter and the indents were placed far enough apart to avoid interference. The indenter radii and machine stiffness were determined by the averaged results from these tests. In addition, indentations on a tin sample were also made with each indenter

for measuring the indentation impressions using a white light interferometer. Because of the extreme low value of hardness in tin and almost no elastic recovery after indenting, it is believed that the residual impression left on the sample surface accurately reflects the shape of the indenter tip. 2D and 3D profiles of the impressions were acquired using a Wyko NT 9100 white light interferometer, as shown in the insert of Fig. 4.2. Subsequently, the indenter radius was extracted by fitting the 2D profile to a spherical cap. This procedure was repeated multiple times to obtain the average and standard deviation values reported in Table 1. It is worth noting that, under current resolution, the optical profiler can only accurately measure an indenter radius larger than 50 μm.

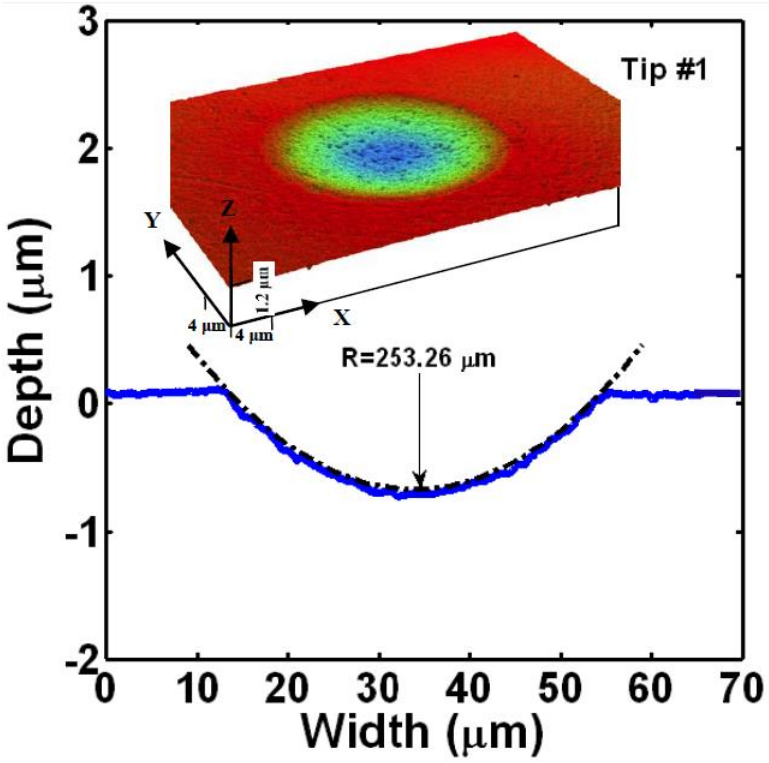

Figure 4.2 Line scan and three dimensional view of the indentation impression on tin characterized by a white light interferometer, from which the indenter tip radius can be determined. Dash curve represents spherical tip with radius of 253 μm.

As listed in Table 4.1, out of a total of 8 indenters, indenters with tip radii equal to or greater than 50 μm are marked as large indenters including Tip #1, Tip #2 , Tip #3 and Tip #4, while those smaller than 50 μm are marked as small indenters, consisting of Tip #5, Tip #6, Tip #7 and Tip #8. The nominal tip radius is generally considered inaccurate and the "actual indenter tip radius" is routinely derived from direct Hertzian fitting to the experimental *P-h* data [155,183,185]. In the present work, both the Herzian theory in Eq. (4-1) and the modified Hertzian model in Eq. (4-5) were applied to determine the indenter tip

radii and the differences were examined. These methods are compared to the optical profile measurements.

4.4. Results

4.4.1. Determination of indenter radius R

Results from the indenter Tip #2 (nominal radius =100 μm) are used for illustrative purpose and processes for other tips are essentially the same. All the final results are given in Table 4.1. Typical P-$h_{reported}$ curves on the fused silica and sapphire with Tip #2 are plotted in Fig. 4.3(a). Deformations in all cases are limited to the elastic region, as confirmed by the full unloading path that collapses onto the loading path. This helps to avoid difficulties in identifying the elastic-plastic transition points in the plastically deformed materials and ensure applicability of the Hertzain theory to all data. Due to the large difference in indentation moduli, sapphire and fused silica have distinct displacements, h_{fs} and h_{sp}, at the same loads and this large difference enables quality of data for the fitting in Eq. (4-8).

We first directly use the Hertzian theory to fit the experimental P-$h_{reported}$ curves (i.e., implicitly assuming $S_{default}$ as the machine stiffness) to get tip radii, as indicated by the black dashed curves in Fig. 4.3(a). All calculations yield smaller indenter tip radii compared to the nominal radii, as listed in Table 1. These fittings are seemingly reasonable, but we will show that the results are significantly different from both the optical profiler measurement and our subtraction method. Also such a fitting gives different tip radii for the two materials, which clearly indicates the invalidity of this

method. In the subtraction method in Eq. (4-8), data points $\left(P, h_{fs}\right)$ and $\left(P, h_{sp}\right)$ at the same loads on Fig. 4.3(a) are used. The linear fitting between $h_{fs} - h_{sp}$ and $P^{2/3}$ in Fig. 4.3(b) clearly demonstrates the success of our method in Eq. (4-8). Note that only several data points are plotted on Fig. 4.3(b); the fitting curves are obtained from all the data points in the designated load range. The tip radius can be determined from the slope, which equals to $\left(\frac{4}{3}\sqrt{R}\right)^{-2/3}\left(E_{\mathrm{I}}^{*-2/3} - E_{\mathrm{II}}^{*-2/3}\right)$. The fitted intercept corresponds to $h_{0,\mathrm{I}} - h_{0,\mathrm{II}}$, which reflects the difference in the uncertainty of onset of contact for these two materials, and can be positive and negative.

Figure 4.3 Determination of the indenter tip radius. (a) Experimental P-hreported data on sapphire and fused silica using the Tip #2 indenter, shown by symbols. Direct Hertzian fitting is shown by the black solid curves and the Hertzian solutions with indenter radii obtained from our subtraction method are given by the red dashed curve. (b) The subtraction method is used to fit h_{fs}-h_{sp} (fs: fused silica; sp: sapphire) to $P^{2/3}$ as in Eq. (4-8). The slope can be used to determine the indenter tip radius.

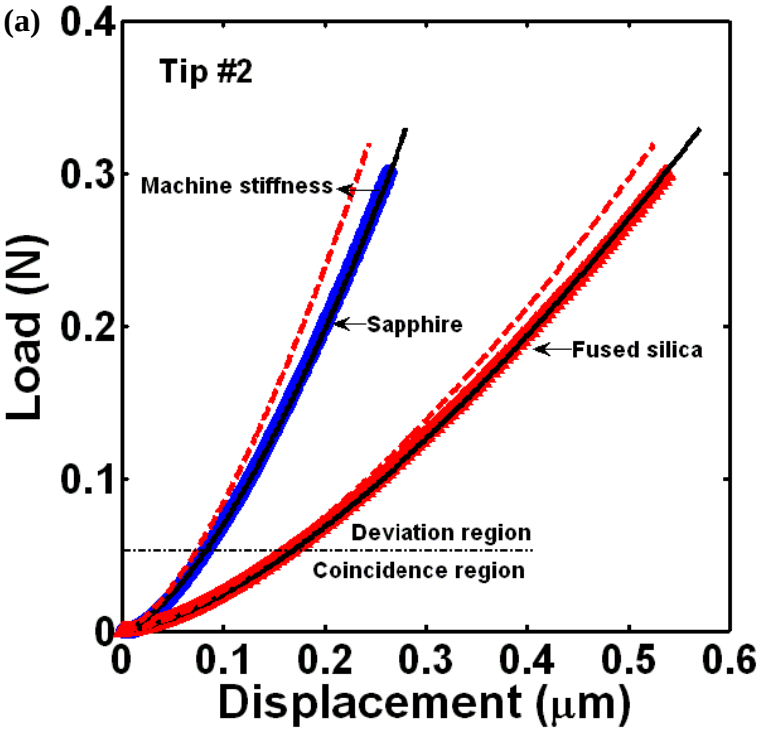
(a)
Tip #2
Machine stiffness
Sapphire
Fused silica
Deviation region
Coincidence region
Load (N)
Displacement (μm)
0
0.1
0.2
0.3
0.4
0.5
0.6

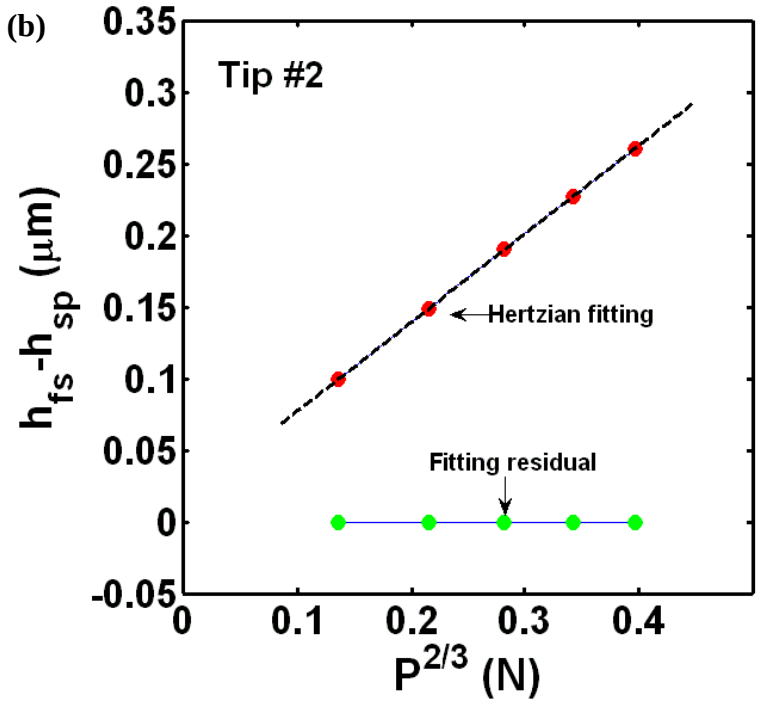
(b)
Tip #2
Hertzian fitting
Fitting residual
h_{fs}-h_{sp} (μm)
$P^{2/3}$ (N)
0.35
0.3
0.25
0.2
0.15
0.1
0.05
0
-0.05
0.1
0.2
0.3
0.4

The indenter tip radii obtained from the above procedure can be found in Table 4.1. For large indenters, the subtraction method gives indenter radii that are very close to the optical profile measurements, but deviate significantly from the direct Hertzian fitting. Thus it is concluded that the subtraction method gives correct tip radius values, while routinely determined radii by the direct Hertzian fitting tend to be underestimated at least for large indenters. The error could be as large as 25%, and using tip radii obtained by the direct Hertzain fitting may lead to incorrect conclusions in practice. For smaller indenters, tip radii obtained by both direct Hertzian fitting and subtraction method are similar, as shown in Table 4.1. Although confirmation by the optical profile measurement is not feasible for these cases, the agreement of these two methods suggests that the Hertzian fitting is applicable for finding the indenter tip radius but only for small indenters. The subtraction method developed in this work is rather universal. The critical condition (i.e., how low the load and displacement may be) regarding the validity of the direct Hertzian fitting is discussed in the Discussion section.

4.4.2. Determination of machine stiffness $S_{machine}$

To examine the significance of the machine stiffness, the Hertzian solutions for two materials, with correct indenter tip radii obtained from our subtraction method, are plotted to compare with the experimental P-$h_{reported}$ curves. As representatively shown in Fig. 4.3(a) for the indenter Tip #2, the Hertzian solutions given by the red dashed curves collapse onto the experimental P-$h_{reported}$ curves at the initial loading stage and then deviate to lower displacements, and this deviation becomes increasingly significant with

the increase of the indentation load. The coincidence of the Hertzian solutions with experimental curves at the low loads in Fig. 4.3(a) indicates that the displacement resulting from the deflection of the loading frame is smaller than the contact response. With a further increase of the applied load, a significant amount of extra displacement results as shown by the $P/S_{machine}$ term in Eq. (4-5), which cannot be accounted for by the predefined machine stiffness. Consequently, the Hertzian solutions deviate from the experimental curves beyond a critical load, being roughly 0.05 N for Tip #2. For convenience, the region below this critical load is termed "coincidence region", while that above this load is termed "deviation region". Similar behavior is found for all other large indenters. For small indenters, the Hertzian solutions overlap nicely with the experimental data throughout all loads, as representatively shown by the indenter Tip #7 in Fig. 4.4. In other words, small indenters only have "coincidence region", because deformation in these cases is restricted to low loads. The predefined machine stiffness can account for deformation of the loading frame at low load levels and hence only a negligibly small deviation is observed. To find out a critical load when the deviation begins and the predefined machine stiffness is no longer applicable, critical loads are systematically analyzed, as shown in Fig. 4.5. This critical deviation load is found to be around 0.05 N.

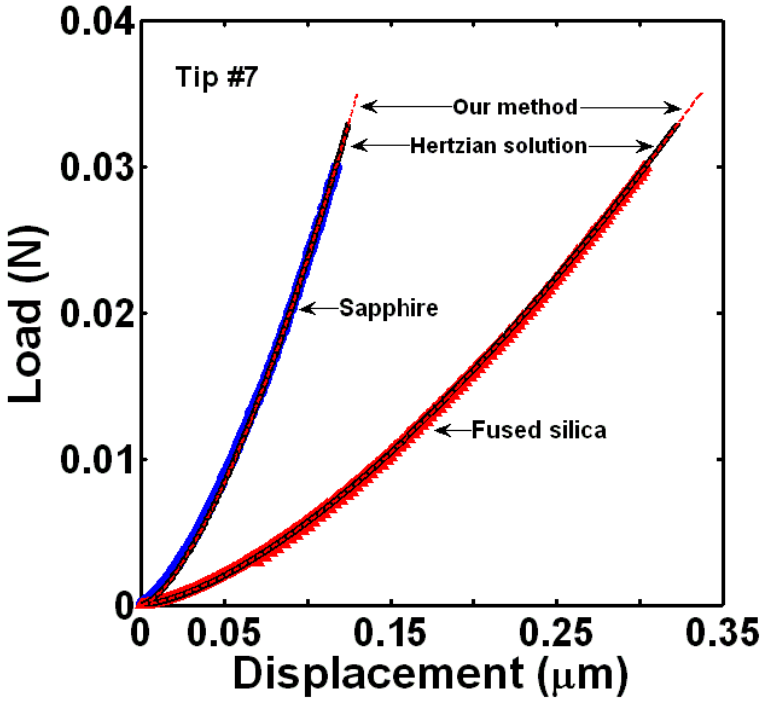

Figure 4.4 Load-displace curves using the small tip-radius indenter (Tip #7). Symbols represent experiment P-hreported curves. Direct Hertzian fitting by using Eq. (4-1) is shown by the black solid curves and the Hertzian solutions with indenter radii obtained fro from our subtraction method are given by the red dashed curve. Notes that the black solid curves overlap the red dashed curve.

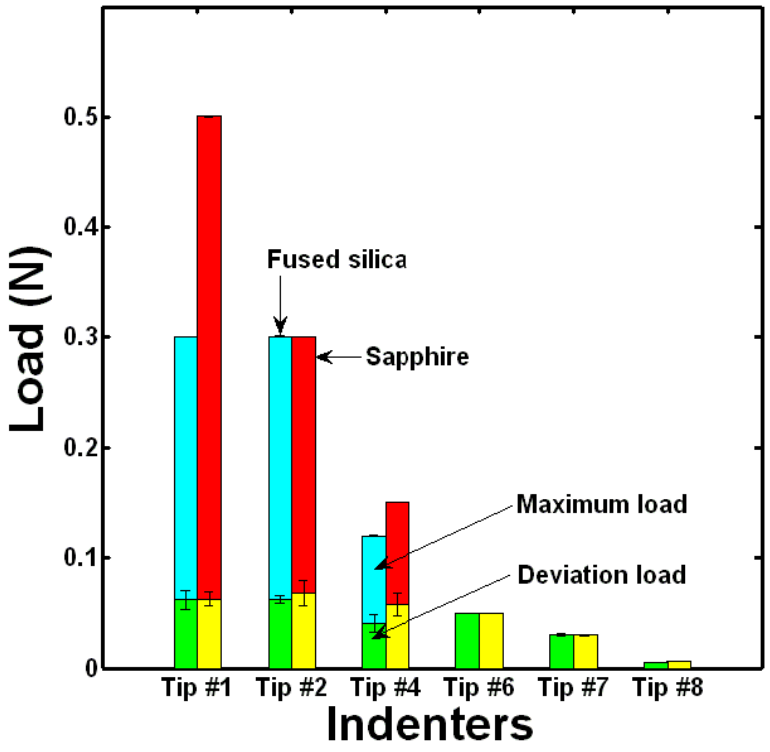

Figure 4.5 Maximum indentation loads and deviation loads for various indenters. The deviation load denotes load where the Hertzian solutions deviate noticeably from experimental P-$h_{reported}$ curves, as shown in Fig. 4.3(a). For small indenters, negligibly tiny deviation occurs, and the maximum loads equal to the deviation loads. The deviation load is around 0.05 N for the large indenters.

The machine stiffness can be quantitatively evaluated from Eq. (4-5) after obtaining the correct indenter tip radius, R, from the subtraction method. The parameter h_0 was found to be on the order of nanometers, one or two orders of magnitude smaller than the used displacement. Calculated machine stiffness at selected load ranges for various indenter tips are presented in Table 4.1. For all four indenter tips, it is found that the machine stiffness increases approximately linearly with the applied load, as

representatively demonstrated for the Tip #2 indenter in Fig. 4.6. This linear dependence of the machine stiffness on the applied load can be described with a linear relationship, $S_{machine}=kP+S_0$, with k and S_0 being fitting parameters as summarized in Table 4.1. With the load range extending upward and downward, it resembles more like a power law relationship. For small indenters, because the Hertzian solution almost overlaps with experimental P-$h_{reported}$ curves, the machine stiffnesses in these cases are indeed very close to the pre-defined value, 9.1 N/μm, as shown by our data in Fig. 4.6. It is noted that different indenters result in different calculated machine stiffness because, as shown in Fig. 4.1(b), the machine stiffness calculated by using our method include all factors into consideration except the contact between the tip end and the sample. These include the deflection of the loading frame, deformation of the indenter tip and mounting materials between the frame and indenter tip. For different indenters, the tip size, shape, tip holder and the tip mounting materials (glue) are slightly different, resulting in different machine modulus.

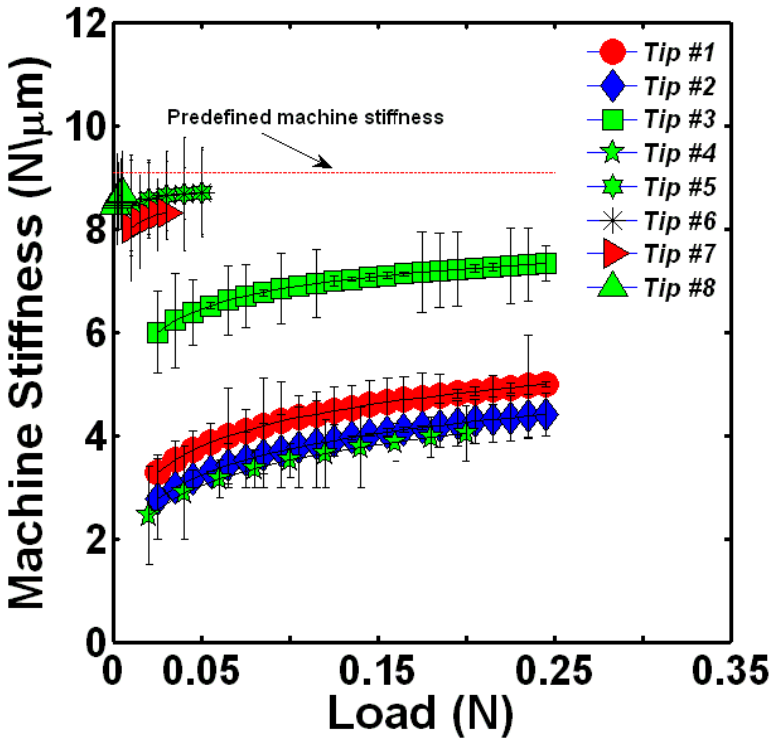

Figure 4.6 Machine stiffness under different loads with selected indenter tips. The machine stiffness approximately shows linear dependence on the load and can be described with $S_{machine} = S_0 + kP$, in which fitting parameters k and S_0 can be found in Table 1. For small indenters, the calculated machines stiffness is close to the pre-defined machines stiffness, $S_{default}$=9.1 N/μm. Machine stiffness at loads below 10% of the maximum load were not calculated because of great system errors.

4.5. Discussion

Many previous researches assumed that the machine stiffness remains constant throughout the entire indentation testing procedure or only interpret their data with a default machine stiffness, which is provided in the software by the manufacturer. Such an assumption may cause measurement errors in realistic applications, given that the

machine stiffness is actually a function of the applied load and may vary for different tips. At low load levels, e.g., < 0.05 N in our case, it is justifiable to employ a constant value for the machine stiffness, because the contact stiffness is much lower than the machine stiffness and its variations associated with increases in the load are small. As a result, directly fitting the experimental P-$h_{reported}$ data with the classic Hertzian solution is appropriate and can give correct indenter tip radii. This is confirmed by our studies on smaller indenter tips, in which the predefined machine stiffness value is taken and ultimately the calculated tip radii are relatively accurate. Our results in Table 4.1 clearly demonstrate that this is not the case for large indenter tips. The assumption of a constant machine stiffness will lead to significant errors. For instance, incorrect indenter tip radii were attained when directly using the Hertzian fitting as in Table 1. Consequently, it can be concluded that the constant machine stiffness assumption is only valid for deriving indenter tip radii with Hertzian theory at small load cases. The critical load value is around 0.05 N for the present instrumented indentation, and may vary for different indentation system. However, our subtraction method can be used to simultaneously obtain tip radii and machine stiffness regardless of the tip radii and load ranges.

To further verify our findings, the contact stiffness for all indenters was calculated for comparison with the calculated machine stiffness. The experimental P-$h_{reported}$ curves were first fitted directly with the Hertzian solution, although the obtained R values are smaller than the actual ones, as has been shown in Table 4.1. Nevertheless, this gives us a contact stiffness by

$$\frac{dP}{dh} = 2E^* \sqrt{Rh} \,. \tag{4-9}$$

Two typical results are selected for illustration purposes; one is Tip #2 representing large indenters, and the other is Tip #7 representing small indenters, as plotted in Fig. 4.7. As expected, the contact stiffness increases exponentially with loads, and is generally higher on the stiff sapphire than the relatively compliant fused silica. It is worth noting that, for large indenter tips, below our proposed critical load level of ~0.05 N, the contact stiffness is one order of magnitude smaller than the machine stiffness; but above this value, it is approaching the same order of magnitude. This is particularly apparent for sapphire because of its high material stiffness. For small indenter tips, like Tip #7, the contact stiffness is one order of magnitude smaller than the machine stiffness throughout the whole loading process. Equivalently speaking, the contribution from deflection of the load frame is smaller than that from the contact response. Thus the displacement obtained from the indenter can be trusted as the material deformation only at the nanoindentation regime (e.g., in our case, P<50 mN).

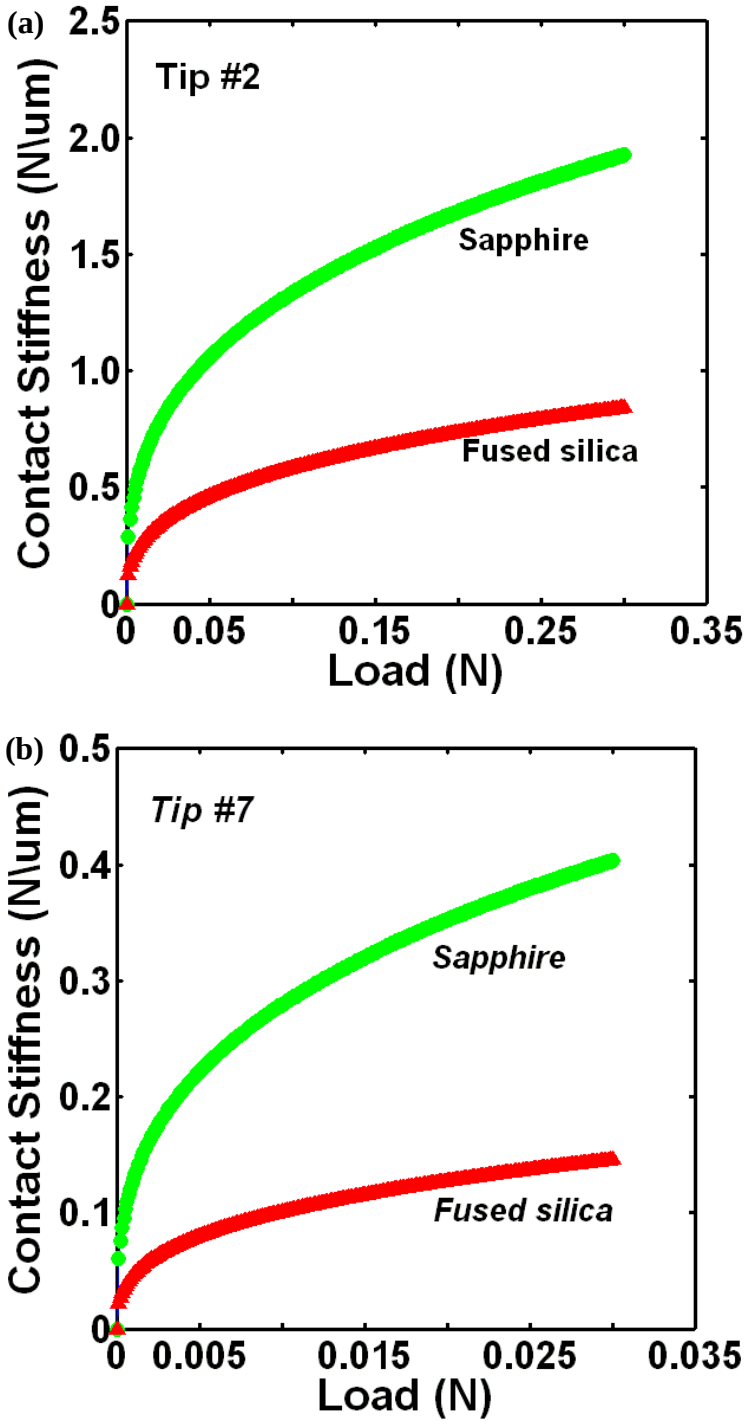

Figure 4.7 Plots of contact stiffness versus load for the two materials using large indenter Tip #2 in (a) and small indenter Tip #7 in (b).

4.6. Summary

Our studies on instrumented indentation with spherical indenter tip radii ranging from several microns to hundreds of microns shows that the routinely utilized method, i.e., direct Hertzian fitting, for determining the indenter tip radius is not appropriate for large indenter tips or above a critical load. Great caution is needed when directly using Hertzian fitting to derive the tip radius. It is acceptable to use at low loads, in our case, P<50 mN. The indenter tip radius is likely to be underestimated by direct Hertzian fitting.

A new approach for simultaneously determining the spherical indenter tip radius and the machine stiffness has been developed by incorporating the contribution of machine stiffness into the classic Hertzian solution. This approach requires two materials, desirably with radically different material stiffness, to be indented. The indenter tip radius can be derived form linear fitting of the displacement differences at the same loads for two materials, (h_I-h_{II}), against $P^{2/3}$. The machine stiffness at various loads, which has been a potential error source in many instrumented indentation applications, can also be determined once the indenter tip radius is known from the previous step. Indentations tests were done on fused silica (relatively compliant material) and sapphire (stiff material) with spherical indenter tip radii in the range of several microns to hundred of microns. Comparisons were made among indenter tip radii obtained from three methods: direct Hertzian fitting, optical profiler measurement and our approach, from which the following conclusions can be drawn.

- Utilizing the classic Hertzian theory to fit individual experimental *P*-*h* data cannot be guaranteed to give the correct spherical indenter tip radius. Large errors will occur when dealing with high load indentations because of machine stiffness, and the tip radius value thus obtained could be underestimated by as much as 25%. In our experiments, the critical load below which Hertzian theory is applicable is suggested to be ~0.05 N when the instrumented indentation system has a machine stiffness of ~10 N/μm.
- The subtraction method developed in this work can give relatively accurate indenter tip radii, regardless of load levels at which the indentation test is performed. This is particularly important when large indenter tips are used, e.g., those with radii of about tens of microns.
- The machines stiffness can be simultaneously obtained from this approach. It is found to be dependent on the applied load and can be described by a linear relationship. Explicit evaluation of the machine stiffness is potentially useful for eliminating the system error and makes the instrumented indentation a more precise technique.
- The contact stiffness increases with the applied load, so that if it eventually reaches the same order of magnitude as the machine stiffness, the deflection of the loading frame contributes substantially to the final displacement readings. And hence the variation of the machine stiffness with respect to the load, i.e.,

$S_{machine}(P)$, has to be taken into consideration rather than assuming a constant machine stiffness.

- Our method has great potential applications in area of the instrumented indentation with spherical indenters, such as the size effect study, modulus and hardness measurement, and determination of contact radius or contact area, among many others.

Table 4.1 Indenter tip radii provided by the manufacturer (denoted as nominal), measured by the optical image of the indentation impressions on tin, derived by fitting to Eq. (4-1) and by our subtraction method in Eq. (4-8) using two materials (sapphire and fused silica). The corresponding machine stiffness can be fitted to the form of $S_{machine} = S_0 + kP$.

	Large indenters				Small indenters			
	Tip #1	Tip #2	Tip #3	Tip #4	Tip #5	Tip #6	Tip #7	Tip #8
Indenter materials	Sapphire	Sapphire	Diamond	Diamond	Diamond	Diamond	Diamond	Diamond
Nominal R (μm)	250.00	100.00	100.00	50.00	9.00	8.30	5.00	2.55
R by optical profiler (μm)	253.26±7.97	98.05±5.54	115.98±9.52	46.66±2.70	n/a	n/a	n/a	n/a
Load range in calculation (N)	0.025-0.25	0.025-0.25	0.025-0.25	0.02-0.20	0.01-0.05	0.01-0.05	0.01-0.03	0.001-0.005
R by Hertzian fitting Sapphire	170.25±0.29	60.05±0.29	110.00±0.22	30.00±0.00	8.85±0.07	5.23±0.02	3.63±0.05	1.64±0.05
Fused silica	210.00±0.12	80.60±0.42	120.10±0.32	39.83±0.24	8.88±0.05	5.25±0.03	3.65±0.03	1.64±0.04
R by subtraction method (μm)	255.68±0.43	96.93±0.58	126.47±0.44	47.48±0.47	8.90±0.05	5.26±0.03	3.66±0.03	1.64±0.05
$S_{machine}$ (N/μm)	3.81-5.04	3.25-4.43	6.44-7.33	2.46-3.53	8.64-8.75	8.47-8.72	8.12-8.40	8.86-8.96
k (μm^{-1})	4.62	4.44	3.17	10.57	6.54	6.28	14.98	63.73
S_0 (N/μm)	3.86	3.50	6.53	2.48	7.89	8.41	7.88	8.40

CHAPTER 5

Nanomechanics of structural origin of the transition from pure glass to metal-like behavior in metallic glasses

5.1. Introduction

Although they have unique mechanical properties such as high strength and good corrosion resistance and thus have attracted significant scientific interests in the past several decades, metallic glasses (or called amorphous alloys) still find a huge gap in technical applications and commercialization [11, 21, 189]. The main culprit is the lack of ductility and the brittle fracture of this class of materials. The deformation mode in the metallic glasses is inhomogeneous below the glass transition temperature, i.e., the strain field will localize into narrow shear bands. Under unconstrained loading conditions such as uniaxial compression, sudden fracture will be observed along a major shear band. Therefore an extrinsic method to improve the ductility is by introducing geometric features, such as second phase and thin film coating, to block the propagation of shear bands and thus to avoid sudden failure along these shear bands [126, 190]. On the other hand, the toughness measurements from cracks or notches under *K*-fields (*K* being the stress intensity factor) have found a range of 1~100 $MPa \cdot m^{1/2}$ for a wide range of metallic glasses. The ductile-brittle transition is believed to be governed by the competition between the cleavage fracture and the crack tip blunting by shear bands, in analogy to the competition between cleavage and dislocation nucleation in crystalline materials. The

resolution of this critical issue clearly relies on a fundamental understanding of the structure-property relationship on the nanoscale.

Because of the amorphous nature, the structural characterization tools such as electron microscopy and X-ray and neutron diffractions hardly reveal useful information on the atomic structure of metallic glasses. For instance, the processing history can dramatically alter mechanical properties of metallic glass, but no noticeable changes in the transmission electron microscope image can be observed in practice [191]. An explicit structure-property relationship for the metallic glass, as that in crystalline materials, is hard to establish. Atomic scale computer simulations, such as reverse Monte Carlo modeling, molecular dynamics, and *ab initio* simulations, provide an alternative to study the structure of the metallic glass [191-193]. With the aid of model glasses, Shi and Falk [194-196] found that less structural relaxation during quenching a metallic glass sample leads to higher degree of short-range order (SRO) and percolation, macroscopically responsible for the high strength and easy initiation of localized deformation. Cheng et al. [197] also observed a considerably increased fraction of icosahedra in the Cu-Zr MG system in a similar scenario. Recent studies by Lee et al. [198], however, suggested that not only the population of icosahedra itself but also the medium-ranged order (MRO) in terms of connectivity of the icosahedra significantly affect the local and global mechanical properties of the metallic glasses. On the other hand, from the continuum mechanics point of view, the inelastic deformation is a result of the evolution of one or many state variables that characterize the atomistic/mesoscale structure. For instance, the free

volume concept has been used to develop a plastic flow model and the stress-driven evolution of free volume leads to a strain softening behavior, which provides a constitutive reason for the strain localization in shear bands. Macroscopic mechanical properties such as strength and toughness, however, cannot be used to distinguish these various structural models and the corresponding constitutive theories. The atomistic nature of these state variables is still unclear [199], and these state variables often find difficulties in explaining atomic-structure-dependent properties such as the annealing effects on the embrittlement of metallic glasses [200-202]. Atomic-level stress developed by Egami and coworkers [181] and the SRO and MRO concepts investigated by atomistic simulations, although providing sound physics-based scenarios, are still hard to link to the constitutive model and the macroscopic properties. The lack of an effective structure-property model substantially constraints resolution of many fundamental issues in the metallic glasses, and a novel approach for effective characterization of this relationship is eagerly needed accordingly.

5.2. Three point-bending tests

We start this paper by showing a wide range of ductile versus brittle behavior of the same metallic glass under different annealing conditions but with *undetectable* structural change. A metallic glass, BAM11 ($Zr_{52.5}Al_{10}Ti_5Cu_{17.9}Ni_{14.6}$ in atomic percents), was fabricated by arc melting and detailed procedures were reported elsewhere [181]. The as-cast samples were subsequently annealed at 200^{o}C, 250^{o}C and 300^{o}C for 1 week for structural relaxation. Three point bending tests on these as-cast and annealed Zr-based bulk metallic glass samples were tested with the load-deflection curves given in Fig. 5.1. The as-cast sample displays a limited degree of inelastic deformation and fractures in a more-or-less ductile manner, while the annealed samples gradually transitions into a purely brittle fracture as the annealing temperature increases. The inelastic energy absorbed by the samples during bending tests, calculated as the area beneath the load-deflection curves subtracted by the elastic energy, decreases substantially as the annealing temperature increases. Fractography examination reveals a transition from the rough fracture surface to a flat, mirror-like state as the samples are being annealed at higher temperatures, as shown in Fig. 5.1(a) for the as-cast and 300^{o}C-annealed samples.

To reveal changes in the atomic structure in these as-cast and annealed samples, high energy synchrotron X-ray diffraction tests were carried out at the 6-ID beamline, Advanced Photon Source, Argonne National Laboratory. Detailed experimental procedure can be found elsewhere [203]. It is found that all annealed samples still retain amorphous structures as in the as-cast state, indicated by the example in Fig. 5.1(b).

Furthermore the pair distribution functions (PDFs) for three representative samples are shown in Fig. 5.1(c), with the inset giving detailed view of the first peak. With increasing annealing temperature, the first peak becomes slightly narrower and shaper, indicating that the positions of the atomic pairs become more well-defined after annealing. Meanwhile, no shift on the peak positions has been found which implies that the average atomic distance of dominant atomic pairs remains the same before and after annealing. Therefore the synchrotron measurement reveals little useful information to explain the sharp change in the ductile/brittle behavior of these as-cast and annealed samples. Other traditional microscopy tools will not be helpful either, due to the featureless characteristics of the amorphous structure. Consequently, an effective approach to characterize the nanoscale structural nature of these metallic glasses is imperative.

Figure 5.1 (a) Load-deflection curves for the as-cast Zr-based metallic glass and variously annealed samples under three point bending test, illustrating the ductile-to-brittle fracture transition. Insets show the fracture surfaces. (b) The synchrotron X-ray diffraction pattern of the annealed sample (at 300ºC). Diffuse rings reveal characteristic amorphous structure. (c) Pair distribution function (PDF) of the as-cast and annealed samples (at 200 ºC and 300ºC) .

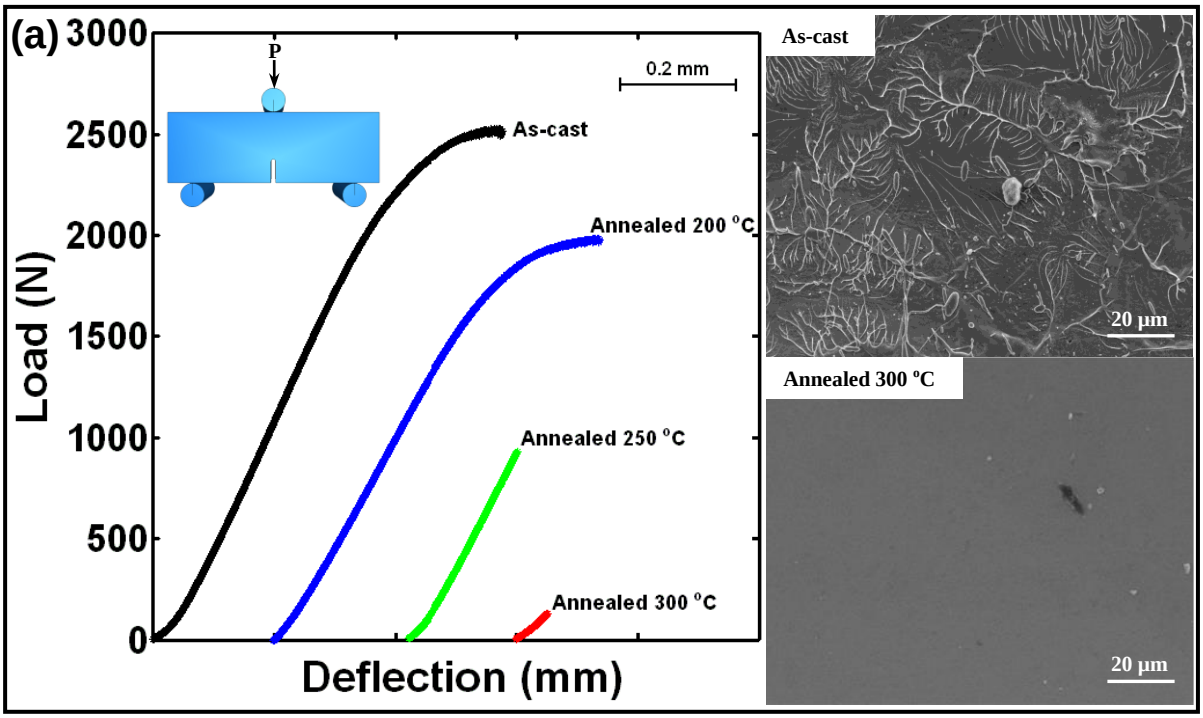
(a)
Load (N)
Deflection (mm)
P
0.2 mm
As-cast
Annealed 200 °C
Annealed 250 °C
Annealed 300 °C
As-cast
20 µm
Annealed 300 °C
20 µm

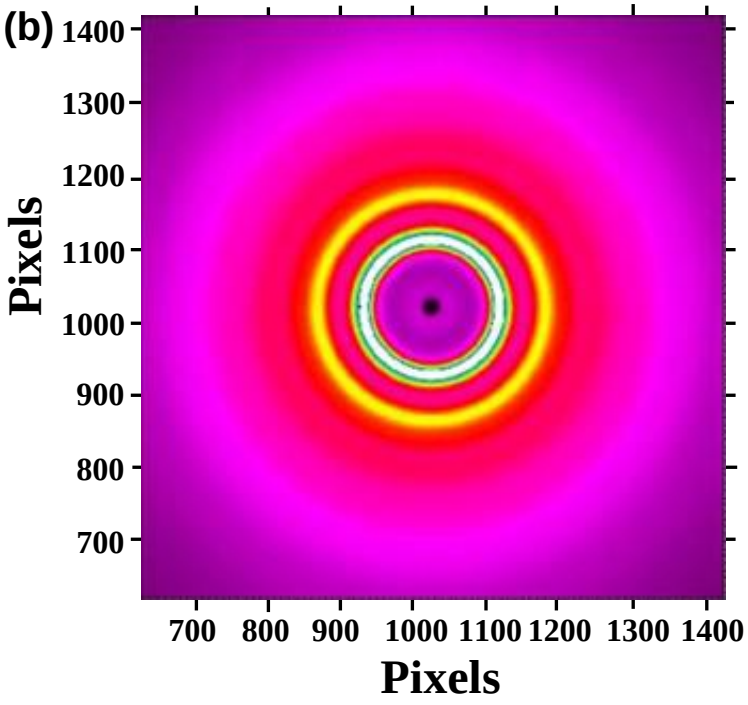
(b)
Pixels
Pixels

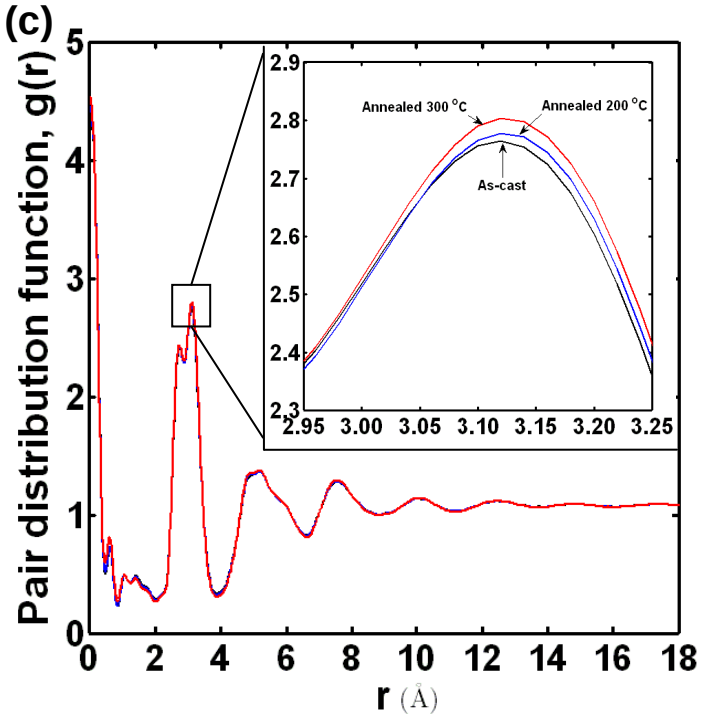
(c)
Pair distribution function, g(r)
r (Å)
Annealed 300 °C
Annealed 200 °C
As-cast

5.3. Statistical nanoindentaiton tests

While an explicit structure-property relationship is difficult to establish based on either the traditional structural characterization techniques or the atomic-scale or continuum simulations, a possible solution is to use mechanical testing at small stressed volumes as a nanoscale structure-property probe. It has been found both numerically and experimentally that the metallic glass structure fluctuates intrinsically from site to site [204-207]. Such a spatial fluctuation of the structure suggests the use of the statistical mechanical mapping for the characterization of the amorphous structure. The nanoindentation technique is an ideal tool along this line. In crystalline materials, nanoindentation using spherical indenters has discovered the pop-in behavior, i.e., the sudden excursion on the load-displacement curves. These tests can be conveniently repeated to gain hundreds or thousands of statistical data, thus providing a spatial sampling of the material of interests. The statistical analysis of the first pop-ins have found that when the crystal is free of dislocations, the pop-in corresponds to the thermally activated, homogeneous dislocation nucleation, while the use of larger indenters or the test on crystals with pre-existing defects demonstrate a stochastic behavior that relies on the stressed volume size and the pre-existing defect density [179, 180, 184]. Likewise, by performing statistical nanoindentation pop-in tests on metallic glass samples with various degrees of structural relaxation, the structural nature of the metallic glass may be thoroughly evaluated.

Nanoindentation tests were performed on both the as-cast and annealed samples at room temperature with a Nanoindenter® XP system with a constant loading rate of $\dot{P}/P$=0.05 s-1. Three spherical indenters with radii being 0.40, 1.78, and 3.80 μm were employed to probe the load-displacement relationships. These radii were calibrated using a newly developed method in [208]. The surface of materials to be indented was mechanically ground with SiC paper down to 1000 grit followed by a 24 hour polishing with colloidal silica. Displacements (h) and loads (P) were measured at the resolutions of 0.16 nm and 0.3 μN, respectively. Around 121 indents were made on each sample, and loads where displacement bursts occur were termed as pop-in loads ($P_{\text{pop-in}}$). A representative nanoindentation load-displacement curve with the indenter tip R=1.78 μm is shown in Fig. 5.2(a) for the as-cast metallic glass. The initial stage of the load-displacement curve is elastic and follows the classic Hertzian solution for spherical elastic contacts by $P = \frac{4}{3} E_r \sqrt{R} h^{3/2}$, where the reduced modulus is $E_r = \left[\left(1-\nu_s^2\right)/E_s + \left(1-\nu_i^2\right)/E_i \right]^{-1}$ with E_i and υ_i being the Young's modulus and Poisson's ratio for the indenter and E_s and υ_s for the specimen. At a critical load of around 2.0 mN, a sudden displacement excursion occurs which marks the onset of inelastic deformation. Beyond this first pop-in, the material will deform plastically as shown by the irreversible unloading curve. Repeating test pop-in tests with the other two indenters, R=0.04 μm and R=3.80 μm, on various annealed samples (200, 250 and 300 ^{o}C) gives the results in Fig. 5.2(b). An important observation is that the $P_{\text{pop-in}}$ increases with the degree of structural relaxation (a higher temperature annealing means a larger degree of

structural relaxation) for all the three indenters. It is also noted that the small fluctuation of the $P_{\text{pop-in}}$ data features the highly relaxed specimens while the large fluctuation occurs for the as-cast and less annealed samples. The corresponding maximum shear stress occurs roughly at a distance of half the contact radius right under the indenter, given by

$$\tau_{\max} = 0.445\left(\frac{16P_{pop-in}E_r^2}{9\pi^3R^2}\right)^{1/3}. \quad (5\text{-}1)$$

The diamond indenters have elastic constants E_i =1141 GPa and ν_i =0.07. The Zr-base metallic glass has elastic constants E_s =89 GPa and ν_s =0.37 [181]. As shown in Fig. 5.2(c), with the increase of the degree of structural relaxation, the maximum shear stress at pop-in is found to increase monotonically while its variation decreases. These tests with four types of materials and three indenters all approach the same highest value of about 4.1 GPa.

Figure 5.2 (a) A representative nanoindentation P-h curve showing the pop-in as the onset of the plastic deformation. (b) Dependence of the first pop-in loads on the annealing temperature and the indenter tip radius (R=0.40, 1.78 and 3.80 μm). (c) Dependence of the maximum shear stress at the first pop-in on the annealing temperature and the indenter tip radius.

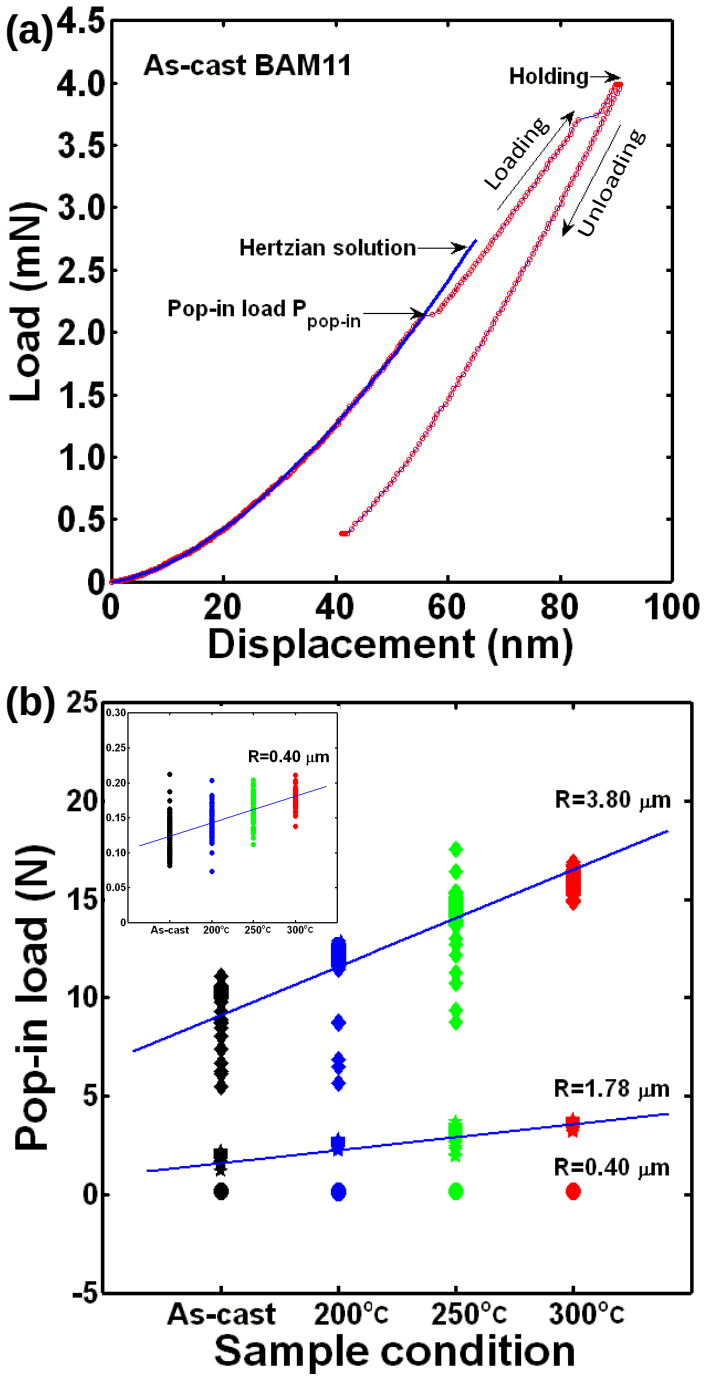
(a)
As-cast BAM11
Holding
Loading
Unloading
Hertzian solution
Pop-in load P pop-in
Load (mN)
Displacement (nm)
0
0.5
1.0
1.5
2.0
2.5
3.0
3.5
4.0
4.5
0
20
40
60
80
100
(b)
R=0.40 μm
As-cast
200°c
250°c
300°c
R=3.80 μm
R=1.78 μm
R=0.40 μm
Pop-in load (N)
Sample condition
-5
0
5
10
15
20
25

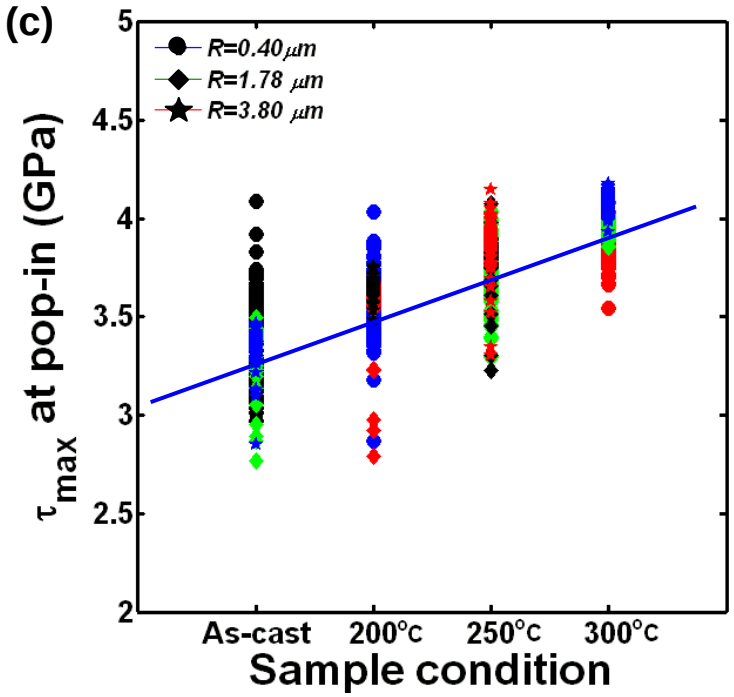
(c)
R=0.40 μm
R=1.78 μm
R=3.80 μm
τmax at pop-in (GPa)
5
4.5
4
3.5
3
2.5
2
As-cast
200°c
250°c
300°c
Sample condition

The statistical analysis of the nanoindentation pop-in data over a relatively large surface area of an indented material was found to be particularly advantageous in revealing the structural information [179, 180, 184]. From the 11×11 nanoindentation pop-in tests, the cumulative pop-in probability curves are generated as a function of the maximum shear stress in Fig. 5.3. As in Fig. 5.2(c), the most relaxed Zr-based metallic glasses (300 ^{o}C) have the largest pop-in stress and the narrowest distribution ranging from ~3.5 GPa to 3.7 GPa. In contrast, the as-cast samples have the smallest τ_{max} values distributed over a larger range from ~2.5 to 3.5 GPa. For the intermediately relaxed states, the cumulative probability distribution is in between; most data are in the range of ~3.0 to 3.5 GPa although a few discrete data points extend to low τ_{max} values.

Figure 5.3 Cumulative pop-in probability as the function of the maximum shear stress τmax under various annealing temperatures and indenters: (a) R=0.40 μm, (b) R=1.78 μm and (c) R=3.80 μm. Solid curves are prediction from our unified structural model.

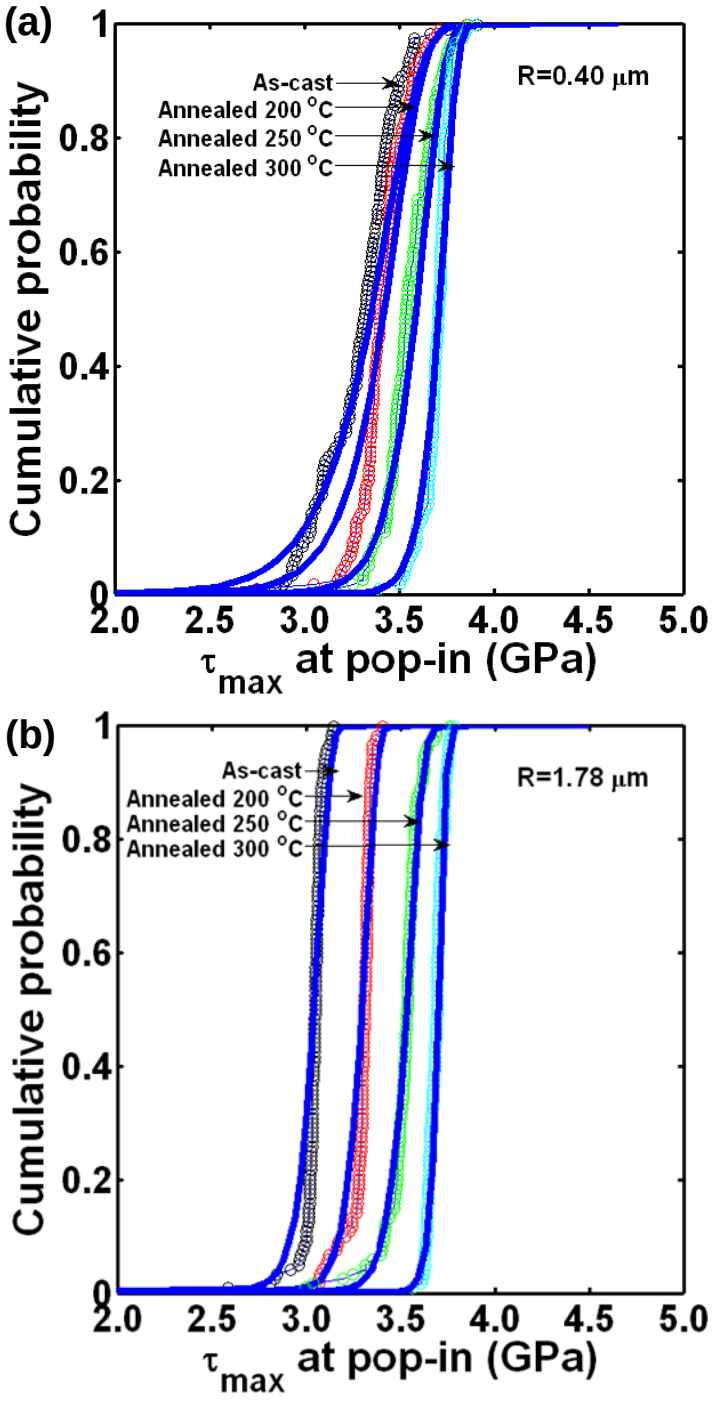
(a)
Cumulative probability
As-cast
Annealed 200 °C
Annealed 250 °C
Annealed 300 °C
R=0.40 μm
τmax at pop-in (GPa)
(b)
Cumulative probability
As-cast
Annealed 200 °C
Annealed 250 °C
Annealed 300 °C
R=1.78 μm
τmax at pop-in (GPa)

\

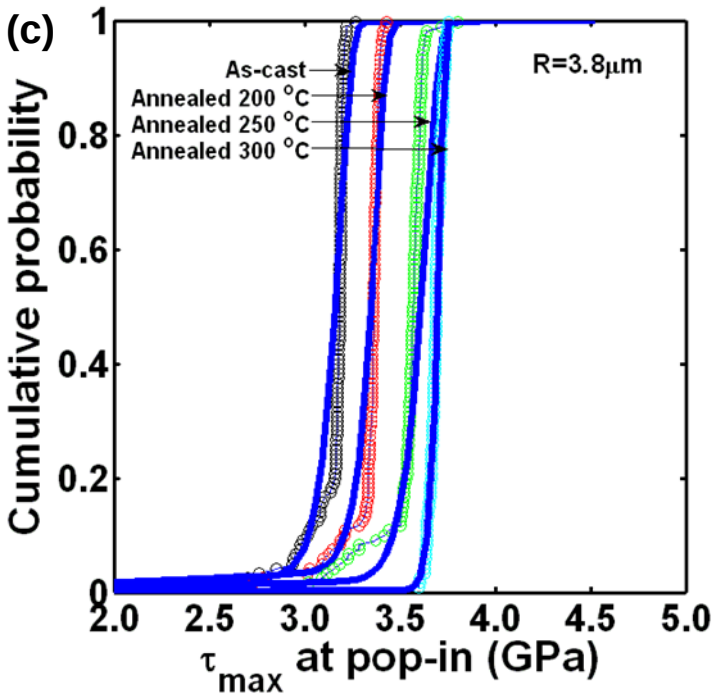
(c)
Cumulative probability
1
0.8
0.6
0.4
0.2
0
As-cast
Annealed 200 °C
Annealed 250 °C
Annealed 300 °C
R=3.8μm
2.0
2.5
3.0
3.5
4.0
4.5
5.0
τmax at pop-in (GPa)

5.4. A quantitative structure-property relation

Pop-in statistics in Figs. 5.2 and 5.3 are a result of spatial sampling of the metallic glasses. As shown in Fig. 4, we propose a structural model – the metallic glass consists of a pure-glass matrix with randomly distributed "soft zones". The pure-glass state is fully annealed and the deformation mechanism is the intrinsic, thermally-activated process near the athermal theoretical strength, τ_{th} . The as-cast and intermediately relaxed samples are characterized by the spatial distribution of the pre-existing defects (i.e., the soft zones) and the distribution of their strength. For simplicity, the latter distribution is assumed to be a Dirac delta function at a defect strength of τ_{def} . The effects of annealing condition and indenter radius can be rationalized as follows. Referring to each individual plot in Fig. 5.3, the increase of annealing temperature is equivalent to reducing the pre-existing defect density, ρ_{def} . This is supported by previous findings that the structural inhomogeneity in the metallic glass decreases by annealing the glass below T_g [209]. In the as-cast sample, as illustrated in Fig. 5.4(a), the statistical measurements have comparable chances of sampling τ_{th} or τ_{def} , leading to large variations in $\tau_{\max}$. In the annealed samples as illustrated in Fig. 5.4(b), the statistical sampling gradually favors the intrinsic, thermally activated process, so that the mean value approaches τ_{th} and the variation in $\tau_{\max}$ decreases. Now comparing the results for the same annealing temperature but with different indenters in Fig. 5.3, it is found that the larger the indenter, the lower the pop-in stress and the higher the variation in the pop-in stress. The contact radius at pop-in, given

by $a_{pop-in} = 1.7\pi R\tau_{\max}/E_r$, increases with the increase of indenter radius, so that the increase of the stressed volume size will lead to the increased probability of sampling the pre-existing defects. In summary, a low defect density and a small stressed volume will approach the intrinsic, thermally activated process with narrow variation of $\tau_{\max}$ near τ_{th}, and the opposite will see the dominance of stochastic, spatial sampling of the pre-existing defects. Next we follow the model in [180, 184] to quantify the unified structural model in Fig. 5.4 and to explain the results in Fig. 5.3.

For the thermally activated process, the nucleation rate per unit volume of material subject to an applied shear stress τ can be written as $\dot{n} = \dot{n}_0 \exp\left[-\left(\varepsilon - \tau v^*\right)/k_B T\right]$ where $\dot{n}_0$ is a pre-factor, ε is the intrinsic nucleation energy barrier, v^* is the activation volume, k_B is the Boltzmann constant, and T is the absolute temperature [210-212]. For a first-order system, the survivability $q_{thermal}$ (i.e., probability for no pop-in) is related to the nucleated rate by $-\dot{q}_{thermal}/q_{thermal} = \dot{n}V$ with V being the stressed material volume. With a boundary condition of $\lim_{\tau \to -\infty} f = 0$, the cumulative probability can be written as

$$f_{thermal} = 1 - q_{thermal} = 1 - \exp\left[-A_0 \int_{-\infty}^{\tau_{\max}^{pop-in}} \exp\left(\frac{\tau_{\max} v^*}{kT}\right) \frac{1}{\tau_{\max}} d\tau_{\max}\right], \tag{5-2}$$

or further simplified as $1 - \exp\left[-A_0 E_i\left(v^* \tau_{\max}^{pop-in}/k_B T\right)\right]$, where $E_i(x) = \int_{-\infty}^{x} t^{-1} e^t dt$ is the exponential integral and $A_0 = 3\dot{n}_0 V \frac{P}{\dot{P}} \exp\left(-\frac{\varepsilon}{k_B T}\right)$; A_0 and v^* are fitting parameters. When

the stressed volume is defect-free and the maximum resolved shear stress reaches the theoretical strength of the material, a shear band will be activated homogeneously and induce displacement extrusion on the load-displacement curve.

On the other hand, the heterogeneous pop-in mechanism is governed by the pre-existing defects in the material. We assume that a pop-in instability will be triggered when a pre-existing defect is sampled in a given volume V_s where the applied stress exceeds the defect strength τ_{def}. As discussed in [180, 184], the probability q_{hetero} of finding no defect can be described by the Poisson distribution,

$$q_{hetero}\left(\rho_{def}, V_s\right) = \exp(-\rho_{def} V_s), \tag{5-3}$$

where V_s is given by a dimensionless function $V_s/a^3 = \hat{V}_s\left(\tau_{def}/\tau_{\max}\right)$ that can be determined from the elastic contact analysis [180, 184]. The contact radius is $a = \left(\frac{3PR}{4E_r}\right)^{1/3}$.

Accordingly the cumulative probably for the heterogeneous mechanism is $f_{hetero} = 1 - q_{hetero}$. Combining Eqs. (5-2) and (5-3), the cumulative pop-in survivability (i.e., finding neither the intrinsic pop-in or the defect-assisted process) is $q_{total} = q_{thermal} \times q_{hetero}$, and the cumulative pop-in probability is $f_{total} = 1 - q_{total}$,

$$f_{total} = 1 - \exp\left[-A_0 E_i \left(v^* \tau_{\max}^{pop-in}/k_B T\right) - \rho_{def} V_s\right]. \tag{5-4}$$

Predictions using the unified structural model in Eq. (5-4) are given by the solid curves in Fig. 5.3 by fitting four parameters, v^* and A_0 for the thermal activation process, and ρ_{def} and τ_{def} for the heterogeneous pop-in mechanism. These parameters

are summarized in Table 5.1. Since annealing will not affect the intrinsic behavior, we first fit the 300ºC-annealed case by only using the model in Eq. (5-2), and the obtained v^* and A_0 will be used as initial trials for the model in Eq. (5-4). Indeed in Table 1, v^* only varies slightly for various annealing conditions and various indenters around ~0.06 nm^3. On the contrary, the defect density ρ_{def} decreases by almost two orders of magnitude as the increase of the degree of structural relaxation. This implies that compared to the thermally activated mechanism, the defect-governed process is more dominant in determining mechanical response of metallic glasses. The defect strength τ_{def} is found to be around 1.0 GPa, close to the shear flow strength of the BAM11 [181, 213, 214]. The dependence of $\tau_{\max}$ on the indenter radius is naturally captured in this model, as evidenced by almost the same parameters obtained for these three indenters. It should be noted that using the thermal activation model in Eq. (5-2) blindly for all the curves will give v^* decreases from ~0.06 nm^3 (for 300ºC-annealed sample) to ~0.02 nm^3 (for the as-cast sample) but with relatively poor fitting quality. This trend agrees with the work using the same fitting procedure by Choi et al. [215], which has attempted to correlate this activation volume change to the annealing-induced structural change. However, the undetectable structural change in Fig. 5.1 suggests the invalidity of solely using the thermal activation model.

Ductile to brittle transition upon annealing in metallic glasses can be interpreted by our unified structural model in Fig. 5.4. The as-cast metallic glasses contains a large amount of defects and the mechanical behavior and shear band mediated deformation

process in this case are mainly coordinated by the defect-assisted process. Not only the initiation of shear band is considerably facilitated, but also the propagating shear band will find large probability to pass through the soft zones. These soft zones will be capable of deflecting or deferring the shear band propagation, and accommodating a larger degree of inelastic deformation than the pure-glass state. Therefore, the as-cast samples usually exhibit low strength but good ductility, exhibiting a metal-like behavior. With the increasing degree of structural relaxation, the density of soft zones decreases as in Fig. 5.4(b), and an extreme case corresponds to their complete elimination as in Fig. 5.4(c) for 300ºC annealed samples. Under these circumstances, the initiation of shear band becomes considerably difficult since the athermal theoretical strength is approached, and the propagation of shear band will experience little or no internal resistance. Cleavage fracture is thus more likely to happen since crack tip blunting by shear bands is difficult to realize. This "pure glass" state corresponds to a steep slope on the cumulative pop-in probability curve.

Table 5.1 Fitting parameters in the unified structural model that incorporates both the thermal activation process and defect-assisted stochastic behavior.

Indenter radius R, μm	0.40				1.78				3.80			
Annealing temperature, ^{o}C	As-cast	200	250	300	As-cast	200	250	300	As-cast	200	250	300
v^{*}, nm^{3}	0.059	0.061	0.060	0.059	0.072	0.067	0.062	0.061	0.073	0.072	0.060	0.061
A_0 ($\times 10^{-22}$)	2.86	1.09	2.37	3.76	6.56	4.99	2.07	2.16	3.32	3.80	6.52	2.82
τ_{def}, GPa	0.98	0.98	0.98	0.98	0.98	1.14	1.14	0.98	1.20	0.98	0.98	0.98
ρ_{def} ($\times 10^{15}$), m^{-3}	4.70	2.48	1.3	0.12	5.40	3.04	1.24	0.11	3.80	2.35	0.88	0.11

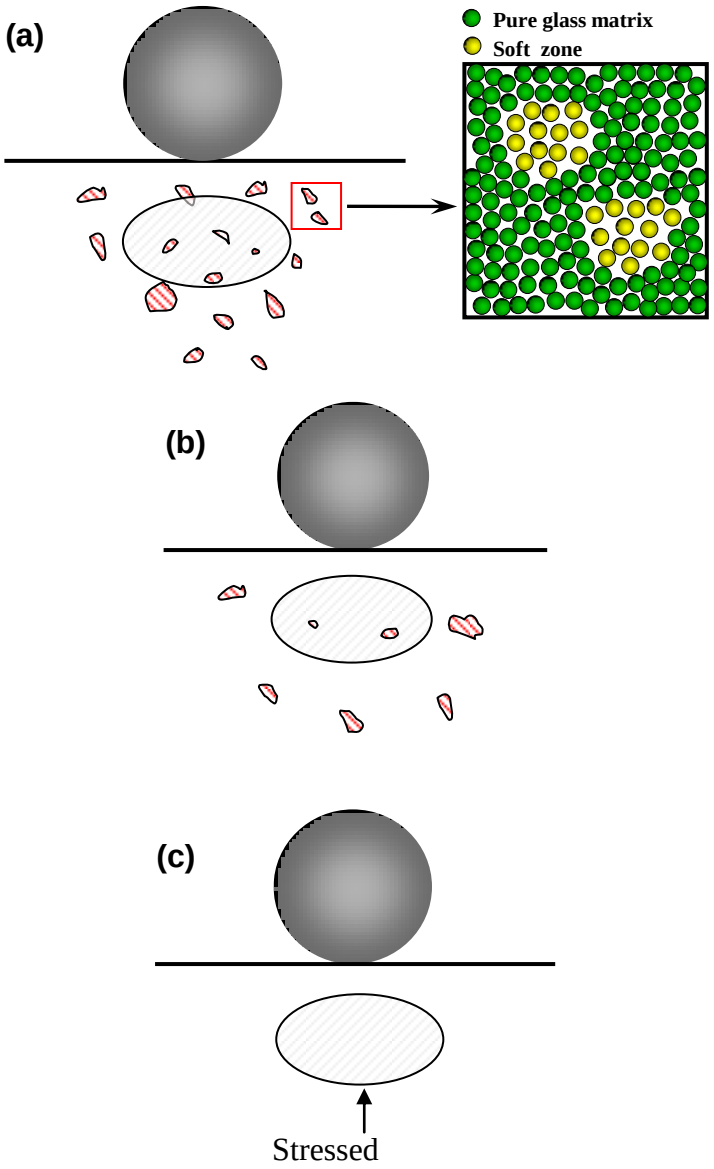

Figure 5.4 Schematic illustration of the structural origin of the transition from metal-like to pure glass behavior in metallic glasses: (a) the as-cast condition, (b) intermediately relaxed state, and (c) extremely relaxed state (i.e., pure glass). Soft zones, as pre-existing defects, will facilitate ductile deformation, while the pure-glass state experiences the intrinsic, thermally-activated deformation.

5.5. Summary

In summary, as-cast and variously annealed samples show undetectable changes on the pair distribution functions, but their mechanical responses range dramatically from ductile to brittle behavior. This work demonstrates that the nanoindentation pop-in tests provide a nanomechanics-based method to statistically probe the structural information of these metallic glasses. The observed mechanical heterogeneity is a consequence of the convolution of the intrinsic thermal activation process (characterized by v^* and A_0) and the structural heterogeneity (characterized by ρ_{def} and τ_{def}). Our model does not specify the details of the heterogeneous deformation process, so that clearly our unified model can be improved with knowledge on structural information such as the atomic-level stress, SRO and others obtained from X-ray/neutron diffraction or molecular dynamics simulation. To this end, important issues such as the ductile-brittle transition can hopefully be resolved.

CHAPTER 6

Conclusions and perspectives

As concluding remarks, the objective of this thesis work is to understand deformation mechanism of the metallic glasses and it structural origin. To achieve this goal, finite element simulations with both the Rudnicki-Rice instability theory and free volume model were performed to investigate mechanisms contributing to ductility enhancement in the thin film coated BMG and dendritic crystal reinforced BMG composites, and shear band pattern under direct indentation and bonded-interface indentation. Experimentally, spherical nanoindentation tests with calibrated indenter tip radii were conducted to statistically study maximum shear stress for establishing a effective structure-property relationship of the metallic glasses. Based on the modeling and experimental studies, the following conclusions can be drawn.

(1) Even when the size of the nanopillar sample is reduced to 140 nm, inhomogeneous deformation still dominates the metallic glass, which is supported by large localized deformation at the pillar top. This attributes to a taper angle in the pillar top, which is inevitable during its fabrication using focused ion beam (FIB). The shear bands are invisible from outside, but can be explicitly observed inside the pillar top by using the free volume model simulation. Accordingly, studying size effect in the metallic glass with FIB-fabricated tapered nanopillar sample is not a viable technique for the

identification of the transition from inhomogeneous to homogeneous deformation mode in metallic glasses

(2) With free volume modeling, only the radial shear bands were observed in the case of direct indentation on the bulk metallic glasses, but both the radial and semi-circular shear bands were found in the case of bonded-interface indentation. This concludes that the radial shear bands are intrinsic to the metallic glasses, while the semi-circular shear bands are a result of stress relaxation on the bonded-interface. Experimentally observed radial and semi-circular shear bands by the bonded-interface technique are a combination of both effects.

(3) The enhanced ductility in the titanium thin film coated bulk metallic glasses attributes to shear band reflection at the coating/substrate interface and shear band branching inside the metallic glass substrate. Good adhesion and relatively small coating thickness are also contributing factors for good ductility in the coating/BMG system.

(4) As in experiments, modeling successfully predicts a relaxation on the lattice strain of the crystalline phases in the dendritic reinforced bulk metallic glass composites. This attributes to load partitioning after metallic glass matrix yields. This lattice strain relaxation was also found depends on the orientation of the dendritic crystalline phases. The improved ductility of the metallic glass composite results from more shear band initiation at the second phase/matrix interface and blockage of the shear band propagation by the second phases.

(5) By taking the machine stiffness into the classic Hertzian solution rather than assuming a constant machine stiffness, the spherical indenter tip radius and machine stiffness in arbitrary ranges of loads and indenter radii can be simultaneously derived. In contrast, the direct Hertzian fitting method tends to underestimate the radius, especially for larger indenter tips. The success is based on indention tests on two materials with known material stiffness, and the displacement difference under the same load is not affected by the machine stiffness. A total of eight spherical indenter tips with the radius ranging from a few microns to hundreds of microns have been indented on fused silica and single crystal sapphire. Our method gives correct indenter radii for all indenters, The machine stiffness is found to indeed vary with the indentation load and indenter radius.

(6) The statistical nanoindentation pop-in tests provide a nanomechanics-based statistical method to probe the structural information of these metallic glasses. Prediction with a structural model incorporating both the thermally-activated shear band formation process and defect-assisted shear band generation indicates that the defect is a dominate factor in determining mechanical properties of the metallic glasses. When a large amount defects exist, the metallic glass exhibit relative ductile behavior since the shear bands could be deflected by the defects during propagation, like the as-cast metallic glasses. In contrast, complete brittle fracture behavior, like a pure glass, features those glasses with less defects, like the substantially annealed samples.

This dissertation presents a couple of original works on the mechanical property and structure-mechanical property relation in the metallic glasses, aiming to uncover

structural nature and deformation mechanism of the metallic glasses. Although many insightful findings are obtained, these works can be further extended along following lines.

(1) The size effect claimed by others previously based on the observation that the shear bands were not observed when compressing tapered metallic glass nanopillars may be misleading. The length scale below which the homogeneous deformation will dominate could be much smaller. In this sense, a constitutive relation which could incorporate a small length scale is hopefully to predict the transition from the inhomogeneous to homogeneous deformation mode.

(2) In practice, to achieve optimal ductility improvement for the bulk metallic glasses, good adhesion should be ensured and careful attention should be paid in the choice of the coating thickness. Furthermore, in experiments the coating type is also found to have significant influence on the ductility improvement. Simulation with proper technique could reveal underlying mechanisms.

(3) Our method for simultaneously determining the indenter tip radius and machine stiffness has many potential applications in area of the nano-indentation with spherical indenters, such as indentation size effect, modulus and hardness measurement, micropillar testing.

(4) The present structural model of the metallic glass could still be valid by replacing ν^* and ρ_{def} with other structural parameters, like the atomic-level stress, SRO and others obtained from X-ray/neutron diffraction or molecular dynamics simulation.

Accordingly, this approach will become more versatile if the scaling relation of various structural parameters can be constructed. One possible line to improve and perfect this structure-property relationship in the metallic glass is to combine the present statistical nanoindentation analysis and the small-scale simulation by taking its advantage of being able to reveal key features of the short-to-medium range order. In this sense, many long-standing fundamental issues in the metallic glass community, such as shear banding behavior and size effect, is hopefully to be resolved. And the underlying physical principles responsible for special strong-but-brittle mechanical properties of the metallic glasses could be unveiled.

References

1. Klement W, Willens RH, Duwez P. Non-Crystalline Structure in Solidified Gold-Silicon Alloys. *Nature* 1960, 187(4740): 869-870.

2. Greer AL. Metallic Glasses. *Science* 1995, 267(5206): 1947-1953.

3. Johnson WL. Thermodynamic and Kinetic Aspects of the Crystal to Glass Transformation in Metallic Materials. *Prog Mater Sci* 1986, 30(2): 81-134.

4. Turnbull D, Fisher JC. Rate of Nucleation in Condensed Systems. *J Chem Phys* 1949, 17(1): 71-73.

5. Turnbull D. Under What Conditions Can a Glass Be Formed. *Contemp Phys* 1969, 10(5): 473-&.

6. Chen HS. Glass-Transition Temperature in Glassy Alloys - Effects of Atomic Sizes and Heats of Mixing. *Acta Metall Mater* 1974, 22(7): 897-900.

7. Inoue A, Nakamura T, Nishiyama N, Masumoto T. Mg-Cu-Y Bulk Amorphous-Alloys with High-Tensile Strength Produced by a High-Pressure Die-Casting Method. *Mater T Jim* 1992, 33(10): 937-945.

8. Inoue A, Zhang T, Nishiyama N, Ohba K, Masumoto T. Preparation of 16 Mm Diameter Rod of Amorphous Zr65al7.5ni10cu17.5 Alloy. *Mater T Jim* 1993, 34(12): 1234-1237.

9. Inoue A, Nishiyama N. Extremely low critical cooling rates of new Pd-Cu-P base amorphous alloys. *Mat Sci Eng a-Struct* 1997, 226: 401-405.

10. Peker A, Johnson WL. A Highly Processable Metallic-Glass - Zr41.2ti13.8cu12.5ni10.0be22.5. *Appl Phys Lett* 1993, 63(17): 2342-2344.

11. Wang WH, Dong C, Shek CH. Bulk metallic glasses. *Mat Sci Eng R* 2004, 44(2-3): 45-89.

12. Inoue A. Stabilization of metallic supercooled liquid and bulk amorphous alloys. *Acta Mater* 2000, 48(1): 279-306.

13. Chen HS, Krause JT, Coleman E. Elastic-Constants, Hardness and Their Implications to Flow Properties of Metallic Glasses. *J Non-Cryst Solids* 1975, 18(2): 157-171.

14. He Y, Price CE, Poon SJ, Shiflet GJ. Formation of Bulk Metallic Glasses in Neodymium-Based Alloys. *Phil Mag Lett* 1994, 70(6): 371-377.

15. Lin XH, Johnson WL. Formation of Ti-Zr-Cu-Ni Bulk Metallic Glasses. *J Appl Phys* 1995, 78(11): 6514-6519.

16. Tan H, Lu ZP, Yao HB, Yao B, Feng YP, Li Y. Glass forming ability of La-rich La-Al-Cu ternary alloys. *Mater Trans* 2001, 42(4): 551-555.

17. Leonhardt M, Loser W, Lindenkreuz HG. Solidification kinetics and phase formation of undercooled eutectic Ni-Nb melts. *Acta Mater* 1999, 47(10): 2961-2968.

18. Poon SJ, Shiflet GJ, Ponnambalam V, Keppens VM, Taylor R, Petculescu G. Synthesis and properties of high-manganese iron-based bulk amorphous metals as non-ferromagnetic amorphous steel alloys. *Supercooled Liquids, Glass Transition and Bulk Metallic Glasses* 2003, 754: 167-177.

19. Zhao ZF, Zhang Z, Wen P, Pan MX, Zhao DQ, Wang WH, *et al.* A highly glass-forming alloy with low glass transition temperature. *Appl Phys Lett* 2003, 82(26): 4699-4701.

20. Dieter GE. *Mechanical Metallurgy (3rd ed)*. McGraw-Hill, 1986.

21. Schuh CA, Hufnagel TC, Ramamurty U. Overview No.144 - Mechanical behavior of amorphous alloys. *Acta Mater* 2007, 55(12): 4067-4109.

22. Srolovitz D, Vitek V, Egami T. An Atomistic Study of Deformation of Amorphous Metals. *Acta Metall Mater* 1983, 31(2): 335-352.

23. Falk ML. Molecular-dynamics study of ductile and brittle fracture in model noncrystalline solids. *Phys Rev B* 1999, 60(10): 7062-7070.

24. Bulatov VV, Argon AS. A Stochastic-Model for Continuum Elastoplastic Behavior .1. Numerical Approach and Strain Localization. *Model Simul Mater Sc* 1994, 2(2): 167-184.

25. Falk ML, Langer JS. Dynamics of viscoplastic deformation in amorphous solids. *Phys Rev E* 1998, 57(6): 7192-7205.

26. Lund AC, Schuh CA. Yield surface of a simulated metallic glass. *Acta Mater* 2003, 51(18): 5399-5411.

27. Langer JS. Dynamics of shear-transformation zones in amorphous plasticity: Formulation in terms of an effective disorder temperature. *Phys Rev E* 2004, 70(4).

28. Spaepen F. Microscopic Mechanism for Steady-State Inhomogeneous Flow in Metallic Glasses. *Acta Metall Mater* 1977, 25(4): 407-415.

29. Steif PS, Spaepen F, Hutchinson JW. Strain Localization in Amorphous Metals. *Acta Metall Mater* 1982, 30(2): 447-455.

30. Argon AS, Kuo HY. Plastic-Flow in a Disordered Bubble Raft (an Analog of a Metallic Glass). *Mater Sci Eng* 1979, 39(1): 101-109.

31. Argon AS, Shi LT. Analysis of Plastic-Flow in an Amorphous Soap Bubble Raft by the Use of an Inter-Bubble Potential. *Philos Mag A* 1982, 46(2): 275-294.

32. Cohen MH, Turnbull D. Molecular Transport in Liquids and Glasses. *J Chem Phys* 1959, 31(5): 1164-1169.

33. Polk DE, Turnbull D. Flow of Melt and Glass Forms of Metallic Alloys. *Acta Metall Mater* 1972, 20(4): 493-&.

34. Mayr SG. Activation energy of shear transformation zones: A key for understanding rheology of glasses and liquids. *Phys Rev Lett* 2006, 97(19).

35. Zink M, Samwer K, Johnson WL, Mayr SG. Plastic deformation of metallic glasses: Size of shear transformation zones from molecular dynamics simulations. *Phys Rev B* 2006, 73(17).

36. Heggen M, Spaepen F, Feuerbacher M. Creation and annihilation of free volume during homogeneous flow of a metallic glass. *J Appl Phys* 2005, 97(3).

37. Fu XL, Li Y, Schuh CA. Contributions to the homogeneous plastic flow of in situ metallic glass matrix composites. *Appl Phys Lett* 2005, 87(24).

38. Heilmaier M, Eckert J. Elevated temperature deformation behavior of Zr-based bulk metallic glasses. *Adv Eng Mater* 2005, 7(9): 833-841.

39. Reger-Leonhard A, Heilmaier M, Eckert J. Newtonian flow of Zr(55)Cu(30)Al(10)Ni(5) bulk metallic glassy alloys. *Scripta Mater* 2000, 43(5): 459-464.

40. Bletry M, Guyot P, Brechet Y, Blandin JJ, Soubeyroux JL. Homogeneous deformation of bulk metallic glasses in the super-cooled liquid state. *Mat Sci Eng a-Struct* 2004, 387: 1005-1011.

41. Lu J, Ravichandran G, Johnson WL. Deformation behavior of the Zr41.2Ti13.8CU12.5Ni10Be22.5 bulk metallic glass over a wide range of strain-rates and temperatures. *Acta Mater* 2003, 51(12): 3429-3443.

42. Kawamura Y, Nakamura T, Inoue A. Superplasticity in Pd40Ni40P20 metallic glass. *Scripta Mater* 1998, 39(3): 301-306.

43. Nieh TG, Schuh C, Wadsworth J, Li Y. Strain rate-dependent deformation in bulk metallic glasses. *Intermetallics* 2002, 10(11-12): 1177-1182.

44. Nieh TG, Wadsworth J, Liu CT, Ohkubo T, Hirotsu Y. Plasticity and structural instability in a bulk metallic glass deformed in the supercooled liquid region. *Acta Mater* 2001, 49(15): 2887-2896.

45. Schuh CA, Lund AC, Nieh TG. New regime of homogeneous flow in the deformation map of metallic glasses: elevated temperature nanoindentation experiments and mechanistic modeling. *Acta Mater* 2004, 52(20): 5879-5891.

46. Johnson WL, Samwer K. A universal criterion for plastic yielding of metallic glasses with a (T/T-g)(2/3) temperature dependence. *Phys Rev Lett* 2005, 95(19).

47. Li JX, Shan GB, Gao KW, Qiao LJ, Chu WY. In situ SEM study of formation and growth of shear bands and microcracks in bulk metallic glasses. *Mat Sci Eng a-Struct* 2003, 354(1-2): 337-343.

48. Donovan PE. A Yield Criterion for Pd40ni40p20 Metallic-Glass. *Acta Metall Mater* 1989, 37(2): 445-456.

49. Liu LF, Dai LH, Bai Y, Wei BC, Eckert J. Behavior of multiple shear bands in Zr-based bulk metallic glass. *Mater Chem Phys* 2005, 93(1): 174-177.

50. Conner RD, Choi-Yim H, Johnson WL. Mechanical properties of Zr57Nb5Al10Cu15.4Ni12.6 metallic glass matrix particulate composites. *J Mater Res* 1999, 14(8): 3292-3297.

51. Wright WJ, Schwarz RB, Nix WD. Localized heating during serrated plastic flow in bulk metallic glasses. *Mat Sci Eng a-Struct* 2001, 319: 229-232.

52. Liu CT, Heatherly L, Easton DS, Carmichael CA, Schneibel JH, Chen CH, *et al.* Test environments and mechanical properties of Zr-base bulk amorphous alloys. *Metall Mater Trans A* 1998, 29(7): 1811-1820.

53. Leamy HJ, Chen HS, Wang TT. Plastic-Flow and Fracture of Metallic Glass. *Metall Trans* 1972, 3(3): 699-&.

54. Chen H, He Y, Shiflet GJ, Poon SJ. Deformation-Induced Nanocrystal Formation in Shear Bands of Amorphous-Alloys. *Nature* 1994, 367(6463): 541-543.

55. Lewandowski JJ, Greer AL. Temperature rise at shear bands in metallic glasses. *Nat Mater* 2006, 5(1): 15-18.

56. Zhang Y, Stelmashenko NA, Barber ZH, Wang WH, Lewandowski JJ, Greer AL. Local temperature rises during mechanical testing of metallic glasses. *J Mater Res* 2007, 22(2): 419-427.

57. Zhang ZF, Eckert J, Schultz L. Difference in compressive and tensile fracture mechanisms of Zr59CU20Al10Ni8Ti3 bulk metallic glass. *Acta Mater* 2003, 51(4): 1167-1179.

58. Gao YF. An implicit finite element method for simulating inhomogeneous deformation and shear bands of amorphous alloys based on the free-volume model. *Model Simul Mater Sc* 2006, 14(8): 1329-1345.

59. Chu JP, Greene JE, Jang JSC, Huang JC, Shen YL, Liaw PK, *et al*. Bendable bulk metallic glass: Effects of a thin, adhesive, strong, and ductile coating. *Acta Mater* 2012, 60(6-7): 3226-3238.

60. Choi YC, Hong SI. Enhancement of plasticity in Zr-base bulk metallic glass by soft metal plating. *Scripta Mater* 2009, 61(5): 481-484.

61. Li HQ, Li L, Fan C, Choo H, Liaw PK. Nanocrystalline coating enhanced ductility in a Zr-based bulk metallic glass. *J Mater Res* 2007, 22(2): 508-513.

62. Wu WF, Zhang CY, Zhang YW, Zeng KY, Li Y. Stress gradient enhanced plasticity in a monolithic bulk metallic glass. *Intermetallics* 2008, 16(10): 1190-1198.

63. Pampillo CA. Flow and Fracture in Amorphous Alloys. *J Mater Sci* 1975, 10(7): 1194-1227.

64. Alpas AT, Embury JD. Flow Localization in Thin-Layers of Amorphous-Alloys in Laminated Composite Structures. *Scripta Metall Mater* 1988, 22(2): 265-270.

65. Leng Y, Courtney TH. Multiple Shear Band Formation in Metallic Glasses in Composites. *J Mater Sci* 1991, 26(3): 588-592.

66. Brothers AH, Dunand DC. Amorphous metal foams. *Scripta Mater* 2006, 54(4): 513-520.

67. Wada T, Inoue A, Greer AL. Enhancement of room-temperature plasticity in a bulk metallic glass by finely dispersed porosity. *Appl Phys Lett* 2005, 86(25).

68. Schroers J, Johnson WL. Ductile bulk metallic glass. *Phys Rev Lett* 2004, 93(25).

69. Dong WB, Zhang HF, Sun WS, Wang AM, Li H, Hu ZQ. Zr-Cu-Ni-Al-Ta glassy matrix composites with enhanced plasticity. *J Mater Res* 2006, 21(6): 1490-1499.

70. Xing LQ, Li Y, Ramesh KT, Li J, Hufnagel TC. Enhanced plastic strain in Zr-based bulk amorphous alloys. *Phys Rev B* 2001, 64(18).

71. Lee ML, Li Y, Schuh CA. Effect of a controlled volume fraction of dendritic phases on tensile and compressive ductility in La-based metallic glass. *Acta Mater* 2004, 52(14): 4121-4131.

72. Zhang Y, Xu W, Tan H, Li Y. Microstructure control and ductility improvement of La-Al-(Cu,Ni) composites by Bridgman solidification. *Acta Mater* 2005, 53(9): 2607-2616.

73. Qiao JW, Zhang Y, Liaw PK, Chen GL. Micromechanisms of plastic deformation of a dendrite/Zr-based bulk-metallic-glass composite. *Scripta Mater* 2009, 61(11): 1087-1090.

74. Dragoi D, Ustundag E, Clausen B, Bourke MAM. Investigation of thermal residual stresses in tungsten-fiber/bulk metallic glass matrix composites. *Scripta Mater* 2001, 45(2): 245-252.

75. Aydiner CC, Ustundag E, Clausen B, Hanan JC, Winholtz RA, Bourke MAM, *et al.* Residual stresses in a bulk metallic glass-stainless steel composite. *Mat Sci Eng a-Struct* 2005, 399(1-2): 107-113.

76. Balch DK, Ustundag E, Dunand DC. Elasto-plastic load transfer in bulk metallic glass composites containing ductile particles. *Metall Mater Trans A* 2003, 34A(9): 1787-1797.

77. Clyne TW, Withers,P.J. *An Introduction to Metal Matrix Composites*. Cambridge University Press, 1993.

78. Gilbert CJ, Ritchie RO, Johnson WL. Fracture toughness and fatigue-crack propagation in a Zr-Ti-Ni-Cu-Be bulk metallic glass. *Appl Phys Lett* 1997, 71(4): 476-478.

79. Hess PA, Poon SJ, Shiflet GJ, Dauskardt RH. Indentation fracture toughness of amorphous steel. *J Mater Res* 2005, 20(4): 783-786.

80. Xi XK, Zhao DQ, Pan MX, Wang WH, Wu Y, Lewandowski JJ. Fracture of brittle metallic glasses: Brittleness or plasticity. *Phys Rev Lett* 2005, 94(12).

81. Nagendra N, Ramamurty U, Goh TT, Li Y. Effect of crystallinity on the impact toughness of a La-based bulk metallic glass. *Acta Mater* 2000, 48(10): 2603-2615.

82. Suh D, Dauskardt RH. Effects of open-volume regions on relaxation time-scales and fracture behavior of a Zr-Ti-Ni-Cu-Be bulk metallic glass. *J Non-Cryst Solids* 2003, 317(1-2): 181-186.

83. Gilbert CJ, Schroeder V, Ritchie RO. Mechanisms for fracture and fatigue-crack propagation in a bulk metallic glass. *Metall Mater Trans A* 1999, 30(7): 1739-1753.

84. Yavari AR. Absence of Thermal Embrittlement in Some Fe-B and Fe-Si-B Glassy Alloys. *Mater Sci Eng* 1988, 98: 491-493.

85. Wu TW, Spaepen F. The Relation between Embrittlement and Structural Relaxation of an Amorphous Metal. *Philos Mag B* 1990, 61(4): 739-750.

86. Lewandowski JJ, Wang WH, Greer AL. Intrinsic plasticity or brittleness of metallic glasses. *Phil Mag Lett* 2005, 85(2): 77-87.

87. Nieh TG, Wadsworth J. Homogeneous deformation of bulk metallic glasses. *Scripta Mater* 2006, 54(3): 387-392.

88. Chen HM, Huang JC, Song SX, Nieh TG, Jang JSC. Flow serration and shear-band propagation in bulk metallic glasses. *Appl Phys Lett* 2009, 94(14).

89. Jang DC, Gross CT, Greer JR. Effects of size on the strength and deformation mechanism in Zr-based metallic glasses. *Int J Plasticity* 2011, 27(6): 858-867.

90. Donohue A, Spaepen F, Hoagland RG, Misra A. Suppression of the shear band instability during plastic flow of nanometer-scale confined metallic glasses. *Appl Phys Lett* 2007, 91(24).

91. Volkert CA, Donohue A, Spaepen F. Effect of sample size on deformation in amorphous metals. *J Appl Phys* 2008, 103(8).

92. Shimizu F, Ogata S, Li J. Yield point of metallic glass. *Acta Mater* 2006, 54(16): 4293-4298.

93. Chen CQ, Pei YT, De Hosson JTM. Effects of size on the mechanical response of metallic glasses investigated through in situ TEM bending and compression experiments. *Acta Mater* 2010, 58(1): 189-200.

94. Schuster BE, Wei Q, Ervin MH, Hruszkewycz SO, Miller MK, Hufnagel TC, *et al.* Bulk and microscale compressive properties of a Pd-based metallic glass. *Scripta Mater* 2007, 57(6): 517-520.

95. Lee CJ, Huang JC, Nieh TG. Sample size effect and microcompression of Mg65Cu25Gd10 metallic glass. *Appl Phys Lett* 2007, 91(16).

96. Lai YH, Lee CJ, Cheng YT, Chou HS, Chen HM, Du XH, *et al.* Bulk and microscale compressive behavior of a Zr-based metallic glass. *Scripta Mater* 2008, 58(10): 890-893.

97. Wu XL, Guo YZ, Wei Q, Wang WH. Prevalence of shear banding in compression of Zr41Ti14Cu12.5Ni10Be22.5 pillars as small as 150 nm in diameter. *Acta Mater* 2009, 57(12): 3562-3571.

98. Tian L, Cheng YQ, Shan ZW, Li J, Wang CC, Han XD, *et al.* Approaching the ideal elastic limit of metallic glasses. *Nat Commun* 2012, 3.

99. Schuster BE, Wei Q, Hufnagel TC, Ramesh KT. Size-independent strength and deformation mode in compression of a Pd-based metallic glass. *Acta Mater* 2008, 56(18): 5091-5100.

100. Dubach A, Raghavan R, Loffler JF, Michler J, Ramamurty U. Micropillar compression studies on a bulk metallic glass in different structural states. *Scripta Mater* 2009, 60(7): 567-570.

101. Greer JR, De Hosson JTM. Plasticity in small-sized metallic systems: Intrinsic versus extrinsic size effect. *Prog Mater Sci* 2011, 56(6): 654-724.

102. Chen CQ, Pei YT, Kuzmin O, Zhang ZF, Ma E, De Hosson JTM. Intrinsic size effects in the mechanical response of taper-free nanopillars of metallic glass. *Phys Rev B* 2011, 83(18).

103. Kuzmin OV, Pei YT, Chen CQ, De Hosson JTM. Intrinsic and extrinsic size effects in the deformation of metallic glass nanopillars. *Acta Mater* 2012, 60(3): 889-898.

104. Uchic MD, Dimiduk DM, Florando JN, Nix WD. Sample dimensions influence strength and crystal plasticity. *Science* 2004, 305(5686): 986-989.

105. Greer JR, Oliver WC, Nix WD. Size dependence of mechanical properties of gold at the micron scale in the absence of strain gradients. *Acta Mater* 2005, 53(6): 1821-1830.

106. Fukuda M, Tomimatsu S, Nakamura K, Koguchi M, Shichi H, Umemura K. A new FIB fabrication method for micropillar specimens for three-dimensional observation using scanning transmission electron microscopy. *J Electron Microsc* 2004, 53(5): 479-483.

107. Van Petegem S, Brandstetter S, Maass R, Hodge AM, El-Dasher BS, Biener J, *et al.* On the Microstructure of Nanoporous Gold: An X-ray Diffraction Study. *Nano Lett* 2009, 9(3): 1158-1163.

108. Dudonis J, Brucas R, Miniotas A. Synthesis of amorphous Zr-Cu alloys by magnetron co-sputtering. *Thin Solid Films* 1996, 275(1-2): 164-167.

109. Spaepen F. A microscopic mechanism for steady state inhomogeneous flow in metallic glasses.pdf. *Acta Metall* 1977, 25: 407-415.

110. Gao YF. An implicit finite element method for simulating inhomogeneous deformation and shear bands of amorphous alloys based on the free-volume model. *Modell Simul Mater Sci Eng* 2006, 14(8): 1329-1345.

111. Kuzmin OV, Pei YT, De Hosson JTM. In situ compression study of taper-free metallic glass nanopillars. *Appl Phys Lett* 2011, 98(23).

112. Liu MC, Huang JC, Chou HS, Lai YH, Lee CJ, Nieh TG. A nanoscaled underlayer confinement approach for achieving extraordinarily plastic amorphous thin film. *Scripta Mater* 2009, 61(8): 840-843.

113. Zhang H, Schuster BE, Wei Q, Ramesh KT. The design of accurate micro-compression experiments. *Scripta Mater* 2006, 54(2): 181-186.

114. Chen MW, Inoue A, Zhang W, Sakurai T. Extraordinary plasticity of ductile bulk metallic glasses. *Phys Rev Lett* 2006, 96(24).

115. Song SX, Wang XL, Nieh TG. Capturing shear band propagation in a Zr-based metallic glass using a high-speed camera. *Scripta Mater* 2010, 62(11): 847-850.

116. Wang YN, Huang JC. Comparison of grain boundary sliding in fine grained Mg and Al alloys during superplastic deformation. *Scripta Mater* 2003, 48(8): 1117-1122.

117. Jana S, Ramamurty U, Chattopadhyay K, Kawamura Y. Subsurface deformation during Vickers indentation of bulk metallic glasses. *Mat Sci Eng a-Struct* 2004, 375: 1191-1195.

118. Ramamurty U, Jana S, Kawamura Y, Chattopadhyay K. Hardness and plastic deformation in a bulk metallic glass. *Acta Mater* 2005, 53(3): 705-717.

119. Zhang HW, Jing XN, Subhash G, Kecskes LJ, Dowding RJ. Investigation of shear band evolution in amorphous alloys beneath a Vickers indentation. *Acta Mater* 2005, 53(14): 3849-3859.

120. Subhash G, Zhang HW. Shear band patterns in metallic glasses under static indentation, dynamic indentation, and scratch processes. *Metall Mater Trans A* 2007, 38A(12): 2936-2942.

121. Xie S, George EP. Size-dependent plasticity and fracture of a metallic glass in compression. *Intermetallics* 2008, 16(3): 485-489.

122. Xie S, George EP. Hardness and shear band evolution in bulk metallic glasses after plastic deformation and annealing. *Acta Mater* 2008, 56(18): 5202-5213.

123. Yoo BG, Jang JI. A study on the evolution of subsurface deformation in a Zr-based bulk metallic glass during spherical indentation. *J Phys D Appl Phys* 2008, 41(7).

124. Wright WJ, Saha R, Nix WD. Deformation mechanisms of the Zr40Ti14Ni10Cu12Be24 bulk metallic glass. *Mater Trans* 2001, 42(4): 642-649.

125. Gao YF, Wang L, Bei H, Nieh TG. On the shear-band direction in metallic glasses. *Acta Mater* 2011, 59(10): 4159-4167.

126. An ZN, Li WD, Liu FX, Liaw PK, Gao YF. Interface Constraints on Shear Band Patterns in Bonded Metallic Glass Films Under Microindentation. *Metall Mater Trans A* 2012, 43A(8): 2729-2741.

127. Jiang MQ, Dai LH. On the origin of shear banding instability in metallic glasses. *J Mech Phys Solids* 2009, 57(8): 1267-1292.

128. Li HQ, Li L, Fan C, Choo H, Liaw PK. Nanocrystalline coating enhanced ductility in a Zr-based bulk metallic glass. *J Mater Res* 2007, 22(2): 508.

129. Rudnicki JW, Rice JR. Conditions for the localization of deformation in pressure-sensitive dilatant materials. *J Mech Phys Solids* 1975, 23: 371-394.

130. Gao YF, Wang L, Bei H, Nieh TG. On the shear band direction in metallic glasses. *Acta Mater* 2011, 59: 4159-4167.

131. Spaepen F. A microscopic mechanism for steady state inhomogeneous flow in metallic glasses.pdf. *Acta Metall* 1977, 25: 407-415.

132. Rullyani C, Chu,J.P., LI,W.D., Gao, Y.F., Liaw, P.K., Ramamurty, U. *Unpublished research results*.

134. Chu JP, Greene JE, Jang JSC, Huang JC, Shen YL, Liaw PK, *et al.* Bendable bulk metallic glass: Effects of a thin, adhesive, strong, and ductile coating. *Acta Mater* 2012, 60(6-7): 3226-3238.

135. Jia HL, Liu, F.X., An, Z.N., Li, W.D., Wang, G.Y., Chu, J.P., Jang, J.S.C., Gao, Y.F., Liaw, P.K. *In Review*.

136. Liu FX. Microstructures and Mechanical Behavior of Multicomponent Metallic-Glass Thin Film. *Dissertation (University of Tennessee)*: 2009.

137. Chiang CL, Chu JP, Liu FX, Liaw PK, Buchanan RA. A 200nm thick glass-forming metallic film for fatigue-property enhancements. *Appl Phys Lett* 2006, 88(13): 131902.

138. Chang YZ, Tsai PH, Li JB, Lin HC, Jang SCJ, Li C, *et al.* Zr-based Metallic Glass Thin Film Coating for Fatigue-properties Improvement of 7075-T6 Aluminum Alloy. *Thin Solid Films,* : Accepted.

139. Jia HL, Zheng, L.L., Li, W.D., Wang, G.Y., Qiao, J.W., Ren, Y., Liaw, P.K., Gao, Y.F. *In Review*.

140. Qiao JW, Zhang Y, Jia HL, Yang HJ, Liaw PK, Xu BS. Tensile softening of metallic-glass-matrix composites in the supercooled liquid region. *Appl Phys Lett* 2012, 100(12).

141. Qiao JW, Sun AC, Huang EW, Zhang Y, Liaw PK, Chuang CP. Tensile deformation micromechanisms for bulk metallic glass matrix composites: From work-hardening to softening. *Acta Mater* 2011, 59(10): 4126-4137.

142. Hofmann DC, Suh JY, Wiest A, Duan G, Lind ML, Demetriou MD, *et al.* Designing metallic glass matrix composites with high toughness and tensile ductility. *Nature* 2008, 451(7182): 1085-U1083.

143. Hays CC, Kim CP, Johnson WL. Microstructure controlled shear band pattern formation and enhanced plasticity of bulk metallic glasses containing in situ formed ductile phase dendrite dispersions. *Phys Rev Lett* 2000, 84(13): 2901-2904.

144. Qiao JW, Zhang Y, Liaw PK. Tailoring Microstructures and Mechanical Properties of Zr-Based Bulk Metallic Glass Matrix Composites by the Bridgman Solidification. *Adv Eng Mater* 2008, 10(11): 1039-1042.

145. Qiao JW, Wang S, Zhang Y, Liaw PK, Chen GL. Large plasticity and tensile necking of Zr-based bulk-metallic-glass-matrix composites synthesized by he Bridgman solidification. *Appl Phys Lett* 2009, 94(15).

146. Li L, Ungar T, Wang YD, Morris JR, Tichy G, Lendvai J, *et al.* Microstructure evolution during cold rolling in a nanocrystalline Ni-Fe alloy determined by synchrotron X-ray diffraction. *Acta Mater* 2009, 57(17): 4988-5000.

147. Li HQ, Choo H, Ren Y, Saleh TA, Lienert U, Liaw PK, *et al.* Strain-dependent deformation behavior in nanocrystalline metals. *Phys Rev Lett* 2008, 101(1).

148. Wang YD, Huang EW, Ren Y, Nie ZH, Wang G, Liu YD, *et al.* In situ high-energy X-ray studies of magnetic-field-induced phase transition in a ferromagnetic shape memory Ni-Co-Mn-In alloy. *Acta Mater* 2008, 56(4): 913-923.

149. Wang YD, Ren Y, Huang EW, Nie ZH, Wang G, Liu YD, *et al.* Direct evidence on magnetic-field-induced phase transition in a NiCoMnIn ferromagnetic shape memory alloy under a stress field. *Appl Phys Lett* 2007, 90(10).

150. Barabash R, Gao YF, Sun YN, Lee SY, Choo H, Liaw PK, *et al.* Neutron and X-ray diffraction studies and cohesive interface model of the fatigue crack deformation behavior. *Phil Mag Lett* 2008, 88(8): 553-565.

151. Huang SY, Brown, D.W., Clausen, B., Teng, Z.K., Gao, Y.F., Liaw, P.K. *Metall Mater Trans A* 2011, 43: 1497.

152. Peirce D, Asaro RJ, Needleman A. An Analysis of Nonuniform and Localized Deformation in Ductile Single-Crystals. *Acta Metall Mater* 1982, 30(6): 1087-1119.

153. Bower AF, Wininger E. A two-dimensional finite element method for simulating the constitutive response and microstructure of polycrystals during high temperature plastic deformation. *J Mech Phys Solids* 2004, 52(6): 1289-1317.

154. Oliver WC, Pharr GM. An Improved Technique for Determining Hardness and Elastic-Modulus Using Load and Displacement Sensing Indentation Experiments. *J Mater Res* 1992, 7(6): 1564-1583.

155. Oliver WC, Pharr GM. Measurement of hardness and elastic modulus by instrumented indentation: Advances in understanding and refinements to methodology. *J Mater Res* 2004, 19(1): 3-20.

156. Cheng YT, Cheng CM. Can stress-strain relationships be obtained from indentation curves using conical and pyramidal indenters? *J Mater Res* 1999, 14(9): 3493-3496.

157. Dao M, Chollacoop N, Van Vliet KJ, Venkatesh TA, Suresh S. Computational modeling of the forward and reverse problems in instrumented sharp indentation. *Acta Mater* 2001, 49(19): 3899-3918.

158. Bradby JE, Williams JS, Swain MV. Pop-in events induced by spherical indentation in compound semiconductors. *J Mater Res* 2004, 19(1): 380-386.

159. Bei H, Lu ZP, George EP. Theoretical strength and the onset of plasticity in bulk metallic glasses investigated by nanoindentation with a spherical indenter. *Phys Rev Lett* 2004, 93(12).

160. Bucaille JL, Stauss S, Felder E, Michler J. Determination of plastic properties of metals by instrumented indentation using different sharp indenters. *Acta Mater* 2003, 51(6): 1663-1678.

161. Lee JH, Gao YF, Johanns KE, Pharr GM. Cohesive interface simulations of indentation cracking as a fracture toughness measurement method for brittle materials. *Acta Mater* 2012, 60(15): 5448-5467.

162. Lee JS, Jang J, Lee BW, Choi Y, Lee SG, Kwon D. An instrumented indentation technique for estimating fracture toughness of ductile materials: A critical indentation energy model based on continuum damage mechanics. *Acta Mater* 2006, 54(4): 1101-1109.

163. Bower AF, Fleck NA, Needleman A, Ogbonna N. Indentation of a Power Law Creeping Solid. *P Roy Soc Lond a Mat* 1993, 441(1911): 97-124.

164. Li H, Ngan AHW. Size effects of nanoindentation creep. *J Mater Res* 2004, 19(2): 513-522.

165. Goodall R, Clyne TW. A critical appraisal of the extraction of creep parameters from nanoindentation data obtained at room temperature. *Acta Mater* 2006, 54(20): 5489-5499.

166. Suresh S, Giannakopoulos AE. A new method for estimating residual stresses by instrumented sharp indentation. *Acta Mater* 1998, 46(16): 5755-5767.

167. Swadener JG, Taljat B, Pharr GM. Measurement of residual stress by load and depth sensing indentation with spherical indenters. *J Mater Res* 2001, 16(7): 2091-2102.

168. Sebastiani M, Bemporad E, Carassiti F, Schwarzer N. Residual stress measurement at the micrometer scale: focused ion beam (FIB) milling and nanoindentation testing. *Philos Mag* 2011, 91(7-9): 1121-1136.

169. Herbert EG, Oliver WC, Pharr GM. On the measurement of yield strength by spherical indentation. *Philos Mag* 2006, 86(33-35): 5521-5539.

170. Jiang P, Zhang TH, Feng YH, Yang R, Liang NG. Determination of plastic properties by instrumented spherical indentation: Expanding cavity model and similarity solution approach. *J Mater Res* 2009, 24(3): 1045-1053.

171. Choi IC, Yoo BG, Kim YJ, Seok MY, Wang YM, Jang JI. Estimating the stress exponent of nanocrystalline nickel: Sharp vs. spherical indentation. *Scripta Mater* 2011, 65(4): 300-303.

172. Lee H, Lee JH, Pharr GM. A numerical approach to spherical indentation techniques for material property evaluation. *J Mech Phys Solids* 2005, 53(9): 2037-2069.

173. Zhao MH, Ogasawara N, Chiba N, Chen X. A new approach to measure the elastic-plastic properties of bulk materials using spherical indentation. *Acta Mater* 2006, 54(1): 23-32.

174. Lee JH, Kim T, Lee H. A study on robust indentation techniques to evaluate elastic-plastic properties of metals. *Int J Solids Struct* 2010, 47(5): 647-664.

175. Lan HZ, Venkatesh TA. On the sensitivity characteristics in the determination of the elastic and plastic properties of materials through multiple indentation. *J Mater Res* 2007, 22(4): 1043-1063.

176. Hyun HC, Kim M, Lee JH, Lee H. A dual conical indentation technique based on FEA solutions for property evaluation. *Mech Mater* 2011, 43(6): 313-331.

177. Montagne A, Tromas C, Audurier V, Woirgard J. A new insight on reversible deformation and incipient plasticity during nanoindentation test in MgO. *J Mater Res* 2009, 24(3): 883-889.

178. Bei H, Gao YF, Shim S, George EP, Pharr GM. Strength differences arising from homogeneous versus heterogeneous dislocation nucleation. *Phys Rev B* 2008, 77(6).

179. Shim S, Bei H, George EP, Pharr GM. A different type of indentation size effect. *Scripta Mater* 2008, 59(10): 1095-1098.

180. Li TL, Bei H, Morris JR, George EP, Gao YF. Scale effects in convoluted thermal/spatial statistics of plasticity initiation in small stressed volumes during nanoindentation. *Mater Sci Tech-Lond* 2012, 28(9-10): 1055-1059.

181. Bei H, Lu ZP, Shim S, Chen G, George EP. Specimen Size Effects on Zr-Based Bulk Metallic Glasses Investigated by Uniaxial Compression and Spherical Nanoindentation. *Metall Mater Trans A* 2010, 41A(7): 1735-1742.

182. Choi IC, Zhao Y, Yoo BG, Kim YJ, Suh JY, Ramamurty U, *et al.* Estimation of the shear transformation zone size fin a bulk metallic glass through statistical a analysis of the first pop-in stresses during spherical nanoindentation. *Scripta Mater* 2012, 66(11): 923-926.

183. Swadener JG, George EP, Pharr GM. The correlation of indentation size effect experiments with pyramidal and spherical indenters. *Mater Res Soc Symp P* 2002, 695: 451-456.

184. Morris JR, Bei H, Pharr GM, George EP. Size Effects and Stochastic Behavior of Nanoindentation Pop In. *Phys Rev Lett* 2011, 106(16).

185. Field JS, Swain MV. A Simple Predictive Model for Spherical Indentation. *J Mater Res* 1993, 8(2): 297-306.

186. Johnson KL. *Contact Mechanics*. Cambridge University Press, Cambridge, UK, 1985.

187. Gao YF, Pharr GM. Multidimensional contact moduli of elastically anisotropic solids. *Scripta Mater* 2007, 57(1): 13-16.

188. Pharr GM, Strader JH, Oliver WC. Critical issues in making small-depth mechanical property measurements by nanoindentation with continuous stiffness measurement. *J Mater Res* 2009, 24(3): 653-666.

189. Yang Y, Ye JC, Lu J, Gao YF, Liaw PK. Metallic Glasses: Gaining Plasticity for Microsystems. *Jom-Us* 2010, 62(2): 93-98.

190. Liu FX, Liaw PK, Jiang WH, Chiang CL, Gao YF, Guan YF, *et al.* Fatigue-resistance enhancements by glass-forming metallic films. *Mat Sci Eng a-Struct* 2007, 468: 246-252.

191. Cheng YQ, Ma E. Atomic-level structure and structure-property relationship in metallic glasses. *Prog Mater Sci* 2011, 56(4): 379-473.

192. Shi YF, Katz MB, Li H, Falk ML. Evaluation of the disorder temperature and free-volume formalisms via simulations of shear banding in amorphous solids. *Phys Rev Lett* 2007, 98(18).

193. Fan C, Liaw PK, Wilson TW, Choo H, Gao YF, Liu CT, *et al.* Pair distribution function study and mechanical behavior of as-cast and structurally relaxed Zr-based bulk metallic glasses. *Appl Phys Lett* 2006, 89(23).

194. Shi YF, Falk ML. Strain localization and percolation of stable structure in amorphous solids. *Phys Rev Lett* 2005, 95(9).

195. Shi YF, Falk ML. Structural transformation and localization during simulated nanoindentation of a noncrystalline metal film. *Appl Phys Lett* 2005, 86(1).

196. Shi YF, Falk ML. Stress-induced structural transformation and shear banding during simulated nanoindentation of a metallic glass. *Acta Mater* 2007, 55(13): 4317-4324.

197. Cheng YQ, Cao AJ, Ma E. Correlation between the elastic modulus and the intrinsic plastic behavior of metallic glasses: The roles of atomic configuration and alloy composition. *Acta Mater* 2009, 57(11): 3253-3267.

198. Lee M, Lee CM, Lee KR, Ma E, Lee JC. Networked interpenetrating connections of icosahedra Effects on shear transformations in metallic glass. *Acta Mater* 2011, 59(1): 159-170.

199. Egami T. Atomic level stresses. *Prog Mater Sci* 2011, 56(6): 637-653.

200. Kanungo BP, Glade SC, Asoka-Kumar P, Flores KM. Characterization of free volume changes associated with shear band formation in Zr- and Cu-based bulk metallic glasses. *Intermetallics* 2004, 12(10-11): 1073-1080.

201. Kohda M, Haruyama O, Ohkubo T, Egami T. Kinetics of volume and enthalpy relaxation in Pt60Ni15P25 bulk metallic glass. *Phys Rev B* 2010, 81(9).

202. Slipenyuk A, Eckert J. Correlation between enthalpy change and free volume reduction during structural relaxation of Zr55Cu30Al10Ni5 metallic glass. *Scripta Mater* 2004, 50(1): 39-44.

203. Tong Y, Dmowski W, Witczak Z, Chuang CP, Egami T. Residual elastic strain induced by equal channel angular pressing on bulk metallic glasses. *Acta Mater* 2013, 61(4): 1204-1209.

204. Yoshimoto K, Jain TS, Workum KV, Nealey PF, de Pablo JJ. Mechanical heterogeneities in model polymer glasses at small length scales. *Phys Rev Lett* 2004, 93(17).

205. Mayr SG. Relaxation kinetics and mechanical stability of metallic glasses and supercooled melts. *Phys Rev B* 2009, 79(6).

206. Ichitsubo T, Hosokawa S, Matsuda K, Matsubara E, Nishiyama N, Tsutsui S, *et al.* Nanoscale elastic inhomogeneity of a Pd-based metallic glass: Sound velocity from ultrasonic and inelastic x-ray scattering experiments. *Phys Rev B* 2007, 76(14).

207. Wagner H, Bedorf D, Kuchemann S, Schwabe M, Zhang B, Arnold W, *et al.* Local elastic properties of a metallic glass. *Nat Mater* 2011, 10(6): 439-442.

208. Li WD, Bei,H., Qu,J., Gao, Y.F. *J Mater Res*. *In Review*.

209. Wang XD, Lou HB, Gong Y, Vainio U, Jiang JZ. Heterogeneities in CuZr-based bulk metallic glasses studied by x-ray scattering. *J Phys-Condens Mat* 2011, 23(7).

210. Li TL, Gao YF, Bei H, George EP. Indentation Schmid factor and orientation dependence of nanoindentation pop-in behavior of NiAl single crystals. *J Mech Phys Solids* 2011, 59(6): 1147-1162.

211. Schuh CA, Mason JK, Lund AC. Quantitative insight into dislocation nucleation from high-temperature nanoindentation experiments. *Nat Mater* 2005, 4(8): 617-621.

212. Zhu T, Li J. Ultra-strength materials. *Prog Mater Sci* 2010, 55(7): 710-757.

213. Wang L, Bei H, Gao YF, Lu ZP, Nieh TG. Effect of residual stresses on the hardness of bulk metallic glasses. *Acta Mater* 2011, 59(7): 2858-2864.

214. Wang L, Bei H, Gao YF, Lu ZP, Nieh TG. Effect of residual stresses on the onset of yielding in a Zr-based metallic glass. *Acta Mater* 2011, 59(20): 7627-7633.

215. Choi IC, Zhao Y, Kim YJ, Yoo BG, Suh JY, Ramamurty U, *et al.* Indentation size effect and shear transformation zone size in a bulk metallic glass in two different structural states. *Acta Mater* 2012, 60(19): 6862-6868.

VITA

Weidong Li was born in Zhangjia kou, Hebei Province, China in 1984. He obtained his Bachelor's degree in Materials Science and Engineering (on the ceramic and mineral material branch) in 2007 from China University of Geoscience (Beijing). Starting from fall 2007, he began to focus on Matreials Processing at University of Science and Technology Beijing and received Master's degree in January, 2010. Roughly half a year later, he came to The University of Tennessee at Knoxville, US, to pursue doctoral degree in the Department of Material Science and Engineering, mainly concentrated on fundamentals of new materials, solid mechanics, fracture mechanics and small-scale mechanical behavior.